

8-2017

Computer-Aided Detection of Pathologically Enlarged Lymph Nodes On Non-Contrast CT In Cervical Cancer Patients For Low-Resource Settings

Brian M. Anderson

The University of Texas MD Anderson Cancer Center UTHHealth Graduate School of Biomedical Sciences,
markba122@gmail.com

Laurence E. Court

The University of Texas MD Anderson Cancer Center, lecourt@mdanderson.org

Ann Klopp

The University of Texas MD Anderson Cancer Center, AKlopp@mdanderson.org


Stephen F. Kry

The University of Texas MD Anderson Cancer Center, Sfkry@mdanderson.org

Jennifer Johnson

The University of Texas MD Anderson Cancer Center, jljohnso@mdanderson.org

Follow this and additional works at: http://digitalcommons.library.tmc.edu/utgsbs_dissertations

 *next page for additional authors*

Part of the [Medicine and Health Sciences Commons](#), and the [Other Computer Engineering Commons](#)

Recommended Citation

Anderson, Brian M.; Court, Laurence E.; Klopp, Ann; Kry, Stephen F.; Johnson, Jennifer; Cressman, Erik; Rao, Arvind; and Yang, Jinzhong, "Computer-Aided Detection of Pathologically Enlarged Lymph Nodes On Non-Contrast CT In Cervical Cancer Patients For Low-Resource Settings" (2017). *UT GSBS Dissertations and Theses (Open Access)*. 746.
http://digitalcommons.library.tmc.edu/utgsbs_dissertations/746

This Thesis (MS) is brought to you for free and open access by the Graduate School of Biomedical Sciences at DigitalCommons@TMC. It has been accepted for inclusion in UT GSBS Dissertations and Theses (Open Access) by an authorized administrator of DigitalCommons@TMC. For more information, please contact laurel.sanders@library.tmc.edu.

Author

Brian M. Anderson, Laurence E. Court, Ann Klopp, Stephen F. Kry, Jennifer Johnson, Erik Cressman, Arvind Rao, and Jinzhong Yang

COMPUTER-AIDED DETECTION OF PATHOLOGICALLY ENLARGED LYMPH NODES ON NON-
CONTRAST CT IN CERVICAL CANCER PATIENTS FOR LOW-RESOURCE SETTINGS

By

Brian Mark Anderson, B.S.

APPROVED:

Laurence E. Court, Ph.D.
Supervisory Professor

Ann Klopp, M.D., Ph.D.

Stephen Kry, Ph.D.

Jennifer Johnson, M.S., M.B.A.

Erik N.K Cressman, M.D., Ph.D., FSIR

Arvind U.K Rao, Ph.D.

Jinzhong Yang, Ph.D.

APPROVED:

Dean, The University of Texas
MD Anderson Cancer Center UTHealth Graduate School of Biomedical Sciences

COMPUTER-AIDED DETECTION OF PATHOLOGICALLY ENLARGED LYMPH NODES ON
NON-CONTRAST CT IN CERVICAL CANCER PATIENTS FOR LOW-RESOURCE SETTINGS

A
THESIS

Presented to the Faculty of
The University of Texas
MD Anderson Cancer Center UTHealth
Graduate School of Biomedical Sciences

In Partial Fulfillment
Of the Requirements
For the Degree of

MASTER OF SCIENCE

by

Brian Mark Anderson, B.S.

Houston, Texas

August, 2017

Copyright © 2017 Brian Anderson. All rights reserved.

Acknowledgements

I would like to thank Varian for their support of this project. I would especially like to thank Dr. Ann Klopp, whose trip to southern Africa created the inspiration for this project and who has continued to provide assistance throughout the creation of this program.

I would like to acknowledge the Texas Advanced Computing Center (TACC) at The University of Texas at Austin for providing grid resources that have contributed to the research results reported within this work. URL: <http://www.tacc.utexas.edu>. Much of the data processing for this project could not have been completed this year if not for TACC.

Thank you to Dr. Laurence Court, who has mentored me throughout this entire project and helped guide me in becoming a better researcher and medical physicist. You've helped me immensely over the past year and a half; it is crazy how fast the time goes. My time has been further enhanced by the wonderful group of students which you've surrounded yourself with, and it has made my experience second to none. I'm glad I'll only be a few floors away in the years ahead.

I would also like to thank Dr. Richard Wendt. I've never met someone so selflessly dedicated to helping each student within this program. Your work has helped me come to love this institution.

Thank you to Betsy Kindred and Frances Quintana, you've both helped me so much throughout my time here.

Thank you to Lisa Edwards for instilling in me a love for physics in high school, to Len Hurst and Michael Goodwill for helping me become interested in Medical Physics through your wonderful mentoring, and to Dr. C. -K. Chris Wang for helping me come to love and appreciate research.

A special thanks to all of my friends for supporting me, especially the PAC10. Devan, thanks for letting me complain to you when the program wasn't working, and listening to me ramble when it finally was. Sy, Rebecca, and Sheila, thank you for being such good friends. Ben, thanks for everything, I wouldn't be in this program if not for you and I wouldn't enjoy my time in Houston half as much if you weren't here as well.

Lastly, and most importantly, I want to thank my parents. You both have helped me so much in everything, far beyond this single project. Your unending patience, love, and support has helped me in everything in do. I love you both.

Abstract

COMPUTER-AIDED DETECTION OF PATHOLOGICALLY ENLARGED LYMPH NODES ON NON-CONTRAST CT IN CERVICAL CANCER PATIENTS FOR LOW-RESOURCE SETTINGS

Brian Mark Anderson, B.S.

Advisory Professor: Laurence E. Court, Ph.D.

The mortality rate of cervical cancer is approximately 266,000 people each year, and 70% of the burden occurs in Low- and Middle- Income Countries (LMICs). Radiation therapy is the primary modality for treatment of locally advanced cervical cancer cases. In the absence of high quality diagnostic imaging needed to identify nodal metastasis, many LMIC sites treat standard pelvic fields, failing to include node metastasis outside of the field and/or to boost lymph nodes in the abdomen and pelvis. The first goal of this project was to create a program which automatically identifies positive cervical cancer lymph nodes on non-contrast daily CT images, which are widely available in LMICs(1).

A region of interest which is likely to contain the nodal volumes relevant for cervical cancer was defined on a single patient CT(2). This region was deformed onto new patients using an in-house, demons-based deformation software. Edge detection and erosion filtering were used to distinguish potential positive nodes from normal structures. Regions on adjacent slices were then connected into a potential nodal 3D-structure. To differentiate these 3D structures from normal tissues, eighty-six features were generated based on the shape and mean pixel values of the structures, and four classification ensemble methods were tested to differentiate the positive nodes from normal tissues. A cohort of fifty-eight MD Anderson cervical cancer patients with pathologically enlarged lymph nodes were used as a training-test set. Similarly, twenty MD Anderson cervical cancer patients were obtained as a validation set. They contained 154 and 35 pathologically enlarged lymph nodes, respectively.

Model comparison led to the selection of the Adaboost ensemble model, utilizing 17 features. In the validation set, 60% of the clinically significant positive cervical cancer nodes were identified along with a false/true positive ratio of ~4:1. The entire process takes approximately 10/number-of-cores-minutes.

Our findings demonstrated that our computer-aided detection model can assist in the identification of metastatic nodal disease where high quality diagnostic imaging is not readily available. By identifying these nodes, radiation treatment fields can be modified to include pathologically enlarged lymph nodes, which is an essential element to providing potentially curative radiotherapy for cervical cancer.

Contents

Acknowledgements	iii
Abstract	v
List of Figures	x
List of Tables.....	xv
1. Chapter 1: Introduction	1
1.1. Cervical Cancer around the World	1
1.2. Anatomical Location of Cervical Cancer	3
1.3. Identification of Disease.....	5
1.4. Staging and Treatment of Cervical Cancer.....	8
1.5. Computer-Aided Detection/Diagnosis (CAD) Systems	12
1.6. Hypothesis	13
1.7. Specific Aims	13
1.8. Organization of Thesis	13
2. Chapter 2: Identification of Potentially Pathologically Enlarged Lymph Nodes.....	14
2.1. Introduction	14
2.2. Data Acquisition.....	14
2.3. Deformation of Region of Interest (ROI) to Patient.....	15
2.4. Expansion of Mask	17
2.5. Identification of Potential Nodes.....	20
2.5.1. Introduction	20
2.5.2. Binary Thresholding.....	22
2.5.3. Erosion and Dilation.....	24
2.5.4. <i>Identification of ideal thresholding</i>	26
2.5.5. Edge Detection	27
2.6. Correction for non-circular geometry and poor identification	31
2.6.1. Binary Image Factors	31
2.6.2. Gaussian Smoothed Image Factors.....	36

2.6.3.	Reshaping of Mask	39
2.6.4.	Removal of Overlapping Structures	41
2.7.	Identification of start points to build 3D structures	43
2.7.1.	Removal of extraneous start points	45
2.8.	Generation of 3D Structure	47
2.9.	Additional Extension	50
2.10.	Results	51
2.11.	Discussion	52
2.12.	Conclusion.....	52
3.	Chapter 3: Identification of differentiating features and optimization of model.....	53
3.1.	Introduction	53
3.2.	Training and Test Generation	53
3.3.	Feature identification.....	55
3.3.1.	Shape Features and Location Feature	55
3.3.2.	Histogram Features.....	57
3.4.	Feature Selection	60
3.4.1.	Model Selection.....	60
3.4.2.	Univariate Analysis	60
3.4.3.	Correlation Test	61
3.4.4.	Multi-Variate Analysis	63
3.5.	Results	66
3.6.	Pinnacle Contour Creation	74
3.7.	Validation Set	75
3.8.	Discussion	76
4.	Chapter 4: Discussion	78
4.1.	General Recap	78
4.2.	Strengths and Weaknesses by Location.....	78
4.2.1.	Limitations.....	81

4.2.2. Future Implementation	82
4.3. Conclusion.....	85
References	Error! Bookmark not defined.
Vita.....	87

List of Figures

FIGURE 1: INCIDENCE AND MORALITY OF CERVICAL CANCER BY GEOGRAPHIC LOCATION [3]	1
FIGURE 2: LOW/MEDIUM AND HIGH/VERY HIGH HDI BY GEOGRAPHICAL LOCATION [3]	2
FIGURE 3: INCIDENCE OF CERVICAL CANCER BY GEOGRAPHICAL LOCATION [4]	3
FIGURE 4: ANATOMICAL DISPLAY OF CERVICAL LYMPH NODES [7]. USED WITH PERMISSION.....	4
FIGURE 5: 5-YEAR RELATIVE SURVIVAL BY STAGE AT DIAGNOSIS [8]	5
FIGURE 6: PET DATA OF AFRICA WHERE AVAILABLE [1]	6
FIGURE 7: CT DATA OF AFRICA WHERE AVAILABLE [1]	7
FIGURE 8: FOUR-BOX FIELD, AP, PA, AND TWO LATERAL TREATMENT FIELDS [17]. USED WITH PERMISSION.	10
FIGURE 9: (LEFT) CORONAL AND (RIGHT) SAGITTAL VIEW OF BONY-ANATOMY BLOCKS, GREEN AND RED RESPECTIVELY, IN FOUR-FIELD BOX TREATMENT. THE MULTICOLORED SECTIONS ARE NODES FROM 50 PATIENTS MAPPED ONTO A SINGLE PATIENT TO CREATE AN ATLAS PATIENT MASK [18] USED WITH PERMISSION	11
FIGURE 10: DISTRIBUTION OF PATHOLOGICALLY ENLARGED LYMPH NODES IN THE FIFTY-EIGHT PATIENT DATASET	15
FIGURE 11: (LEFT) CONTOURS FROM PHYSICIANS OF TWO EXTERNAL ILIAC NODES, SHOWN IN RED. (RIGHT) THE ASSOCIATED PET DATA OF THESE NODES. NOTE THAT THE BRIGHT SPOTS SHOW A MARKED INCREASE IN FDG, ASSISTING THE PHYSICIAN TO DETERMINE IF THEY ARE DISEASE.....	15
FIGURE 12: THE MULTICOLORED SECTIONS ARE NODES FROM 50 PATIENTS MAPPED ONTO A SINGLE PATIENT. THESE NODES WERE USED TO CREATE AN ATLAS PATIENT MASK. USED WITH PERMISSION [18]	16
FIGURE 13: (LEFT) DEFORMATION OF CONTOUR FROM ATLAS PATIENT ONTO (RIGHT) NEW PATIENT ..	17
FIGURE 14: PERCENTAGE OF LYMPH NODES INFERIOR TO THE MOST SUPERIOR SLICE OF THE MASKED REGION VS SUPERIOR EXTENSION. AN EXTENSION OF 75 MM WAS SELECTED IN THE FINAL MODEL.	18
FIGURE 15: PERCENTAGE LYMPH NODES SUPERIOR TO THE MOST INFERIOR ASPECT OF THE MASK VS INFERIOR EXTENSION. AN EXTENSION OF 25 MM WAS SELECTED IN THE FINAL MODEL.	19
FIGURE 16: PERCENTAGE OF NODES INCLUDED WITHIN MASKED REGION VS RADIAL AXIAL EXPANSION	20
FIGURE 17: IDENTIFICATION OF A SINGLE BINARY CIRCLE WITH REGIONPROPS	21
FIGURE 18: IDENTIFICATION OF CONNECTED BINARY CIRCLES, AS A SINGLE OBJECT WITH REGIONPROPS	21

FIGURE 19: NOTE THE DIFFERENCE IN APPEARANCE AFTER HU THRESHOLDING OF THE NON-FILTERED IMAGE (LEFT) VS THE FILTERED IMAGE (RIGHT), IN PARTICULAR IF THE BONE THRESHOLDING WAS DONE ON THE NON-SMOOTHED IMAGE VS SMOOTHED IMAGE. 22

FIGURE 20: INTERNAL ILIAC NODE (LEFT), NOT BEING ATTACHED TO ANYTHING ELSE ON THE BINARY IMAGE (CENTER), IS IDENTIFIED USING REGION PROPS AS A UNIQUE SURFACE (RIGHT). 23

FIGURE 21: AXIAL SLICE OF TWO II NODES, A) CONNECTS TO ARTERY ANTERIORLY ON THE BINARY IMAGE AND B) IS NEARLY INDISTINGUISHABLE FROM THE NORMAL TISSUE ON THE BINARY IMAGE 23

FIGURE 22: (LEFT) AXIAL IMAGE CONVERTED INTO (RIGHT) BINARY IMAGE TO SHOW CONNECTION OF LYMPH NODE WITH NORMAL TISSUE 24

FIGURE 23: (LEFT) IMAGE OF CIRCLE BEFORE EROSION FILTERING, EACH WITH AN AREA OF 375π . (CENTER) AFTER EROSION FILTERING OF A CIRCULAR MATRIX WITH RADIUS 11 PIXELS, EACH SPOT HAS AREA 70π . (RIGHT) MAINTAINING THE CENTROID VALUES FOUND FROM THE CENTER IMAGE AND CORRECTING BACK FOR THE AMOUNT OF EROSION, EACH CIRCLE CORRECTLY IDENTIFIED WITH AREA AROUND 375π 25

FIGURE 24: (LEFT) BINARY WHERE LYMPH NODE AND ARTERY ARE CONNECTED (CENTER) IMAGE AFTER EROSION TO THE POINT WHICH STRUCTURES ARE SEPARATED (BLUE) AND WHERE EROSION WAS UNABLE TO SEPARATE (RED) (RIGHT) CORRECTED AREA FOR EROSION, FINAL IDENTIFICATION. NOTE THAT THE NODE WITHIN THE BLUE BOX HAS BEEN IDENTIFIED, BUT THE ONE IN THE RED BOX HAS NOT BEEN..... 25

FIGURE 25: (TOP) % OF TRUE POSITIVES AND (BOTTOM) RATIO OF FALSE/TRUE POSITIVES VS HU CUTOFF 27

FIGURE 26: (LEFT) IMAGE WITH EDGES IMPOSED FROM SIGMA = 3, (RIGHT) IMAGE WITH EDGES IMPOSED FROM SIGMA = 1..... 28

FIGURE 27: (TOP LEFT) ORIGINAL, FILTERED IMAGE, (TOP RIGHT) IMAGE OF NODE COLLAPSED INTO ARTERY AND NEAR-BY NORMAL TISSUES ON BINARY IMAGE AND (BOTTOM) IMAGE OF NODE WITH EDGE FROM LOG EDGE DETECTION IMPOSED, SIGMA = 3..... 29

FIGURE 28: NUMBER OF FALSE SURFACES GENERATED VS SIGMA 30

FIGURE 29: EXAMPLE OF FORWARD SELECTION FOR SIGMA 30

FIGURE 30: (LEFT) SOLIDITY OF CONNECTING CIRCLES IS .7, (CENTER) SOLIDITY OF SINGLE CIRCLE IS ~ 1 AND (RIGHT) SOLIDITY OF A RECTANGLE IS 1 31

FIGURE 31: (TOP) % OF TRUE POSITIVES FOUND VS SOLIDITY AND (BOTTOM) RATIO OF FALSE POSITIVES TO TRUE POSITIVES VS SOLIDITY. CUTOFF OF 0.85 WAS SELECTED 32

FIGURE 32: (LEFT) IDENTIFICATION OF POTENTIAL SURFACE AND (RIGHT) MASK OF SURFACE..... 33

FIGURE 33: (TOP) PERCENT OF TRUE POSITIVES FOUND VS RADII DIFFERENCE RATIO OF FALSE/TRUE POSITIVES VS DIFFERENCE IN RADII FROM PROJECTION AND (BOTTOM). CUTOFF CRITERIA OF 3.5MM WAS SELECTED. 33

FIGURE 34: (TOP) PERCENT OF TRUE POSITIVES FOUND VS DIFFERENCE IN RADII*RADII. (BOTTOM) RATIO OF FALSE TO TRUE POSITIVES VS DIFFERENCE IN RADII * RADII CUTOFF OF ANYTHING GREATER THAN 50 WAS SELECTED 34

FIGURE 35: (TOP) PERCENTAGE OF TRUE POSITIVES (TP) WITH RADII LESS THAN CUTOFF. RADII GREATER THAN 14 MM WERE REMOVED AND (BOTTOM) RATIO OF FALSE TO TRUE POSITIVES VS MAX RADII CUTOFF. A CUTOFF OF 14 MM WAS SELECTED 35

FIGURE 36: (LEFT) NODE WAS IDENTIFIED FROM BINARY IMAGE, (CENTER) THE MEAN OF THE AREA ON THE ORIGINAL IMAGE, 'BASE', AND (RIGHT) THE MEAN OF THE AREA ON THE OUTSIDE OF THE CIRCLE, 'RING' 36

FIGURE 37: (TOP) PERCENTAGE OF TRUE POSITIVES FOUND WITH MIN MEAN BASE CUTOFF AND (BOTTOM) RATIO OF FALSE/TRUE POSITIVE WITH MEAN BASE CUTOFF. A MINIMUM VALUE OF 10 WAS SELECTED. 37

FIGURE 38: RING MEAN VALUE WAS TAKEN AS THE MINIMUM OF THE RED, BLUE, AND GREEN RING VALUES. 38

FIGURE 39: (TOP) PERCENTAGE OF TRUE POSITIVE FOUND WITH MINIMUM REQUIREMENT OF BASE-RING (BOTTOM) RATIO OF FALSE/TRUE POSITIVES VS BASE-RING MINIMUM HU. A MINIMUM REQUIREMENT OF 15 WAS SELECTED..... 39

FIGURE 40: (TOP) PERCENTAGE OF TRUE POSITIVES FOUND VS SUPERIOR PROJECTION AND (BOTTOM) FALSE TO TRUE POSITIVE RATIO VS SUPERIOR PROJECTION. A PROJECTION OF 100 MM WAS SELECTED..... 40

FIGURE 41: (TOP) PERCENTAGE OF TRUE POSITIVES FOUND VS AXIAL EXPANSION DURING SUPERIOR PROJECTION (BOTTOM) RATIO OF FALSE/TRUE POSITIVES VS AXIAL EXPANSION DURING SUPERIOR PROJECTION. AXIAL EXPANSION OF 1 MM WAS SELECTED..... 41

FIGURE 42: EXAMPLE OF OVERLAPPING SURFACES..... 42

FIGURE 43: (TOP) TRUE POSITIVE FOUND VS CONSTANT FOR OVERLAP AND (BOTTOM) RATIO OF FALSE/TRUE POSITIVES VS CONSTANT FOR OVERLAP. C0 OF 0 WAS ULTIMATELY SELECTED. 43

FIGURE 44: (LEFT) IMAGE OF TWO EI/II CERVICAL CANCER NODES AND (RIGHT) 7 MM INFERIOR, BOTH COMPLETELY GONE..... 44

FIGURE 45: (LEFT AND CENTER) PROJECTION OF SURFACE ONTO INFERIOR SLICE, FINDING NO SURFACES. (RIGHT) CONSIDERATION OF SURFACE AS A STARTING POINT (BLUE CIRCLE). 44

FIGURE 46:(TOP) PERCENTAGE OF TRUE POSITIVES FOUND AS A FUNCTION OF C1 AND C2. (BOTTOM) RATIO OF FALSE/TRUE POSITIVES AS A FUNCTION OF C1 AND C2. 45

FIGURE 47: FOR THE ABOVE IMAGES, THE METRIC VALUE WOULD BE EQUAL TO $(15-0)*5\text{MM}$, OR $75\text{MM}*HU$	46
FIGURE 48: (TOP) PERCENTAGE OF TRUE POSITIVES FOUND VS DIFFERENCE IN $HU * RADIUS$ (BOTTOM) RATIO OF FALSE TO TRUE POSITIVES VS DIFFERENCE IN $HU * RADIUS$. A CUTOFF OF $45\text{MM}*HU$ WAS SELECTED.....	47
FIGURE 49: (LEFT-CENTER) SURFACE IN RED HAS BEEN IDENTIFIED AS A POTENTIAL STARTING POINT (CENTER-RIGHT) THIS SURFACE IS PROJECTED ONTO THE SUPERIOR SLICE, WHERE ANOTHER SURFACE IS IDENTIFIED, THE TWO ARE CONNECTED.	48
FIGURE 50: (TOP) PERCENTAGE OF TRUE POSITIVES FOUND AS A FUNCTION OF C3 AND C4 (BOTTOM) RATIO OF FALSE TO TRUE POSITIVES AS A FUNCTION OF C3 AND C4. C3 WAS SELECTED TO .65 AND C4 0 MM.....	49
FIGURE 51: CONNECTION OF SURFACES FROM A SINGLE LYMPH NODE CANDIDATE	50
FIGURE 52: TWO NODE CANDIDATES WHICH SHARE THE SAME INITIALIZING POINT	50
FIGURE 53: RANDOM SELECTION WITHOUT REPLACEMENT OF 48 PATIENTS FOR TRAINING AND 10 PATIENTS FOR TEST. REPEAT RANDOM SELECTION TO MAKE 30 UNIQUE GROUPS.....	54
FIGURE 54: RADII OF A CANDIDATE NODE	55
FIGURE 55: DIFFERENCE IN DISTANCE ABOUT CENTERS OF SURFACES.....	56
FIGURE 56: (A) (RED) BASE AREA WITH RADIUS R MM, (B) (BLUE) RING AREA WITH RADIUS R MM, (C) (GREEN) SUBBASE AREA WITH RADIUS R-2 MM AND (D) (YELLOW) SUBRING AREA WITH RADIUS R-2 MM.....	57
FIGURE 57: UNIVARIATE ANALYSIS - ADABOOSTM1, AUC FOR EACH VARIABLE	61
FIGURE 58: SPEARMAN CORRELATION TEST, X-AXIS IS THE SAME AS Y-AXIS.....	62
FIGURE 59: EXAMPLE OF FORWARD SELECTION. NOTE THE HIGHEST AUC ON THE FIRST ITERATION IS VARIABLE 1 AND 3. THESE TWO ARE THEN SAVED INTO THE 2 ND ITERATION, ETC.....	64
FIGURE 60: NUMBER OF FEATURES INCLUDED FOR OPTIMIZED DIFFERENTIATION OF TRUE POSITIVES AND NORMAL TISSUES ON GROUP 1.....	65
FIGURE 61: EXAMPLE OF BACKWARD SELECTION. EACH ITERATION REMOVES THE VARIABLE WHICH RESULTS IN THE LARGEST INCREASE IN AUC.....	65
FIGURE 62: EXAMPLE OF FORWARD/BACKWARD SELECTION. THE 'STARTPOINT' COMES FROM THE PREVIOUS FORWARD SELECTION AND EACH ITERATION WITHIN THE BACKWARD SELECTION IS A REMOVAL OF ONE VARIABLE, TRYING TO MAXIMIZE THE AUC	66
FIGURE 63: SERIAL ADDITION FOR ADABOOST, AUC VS # OF VARIABLES INCLUDED BY CORRELATION CUTOFF.....	67
FIGURE 64: % TP AND RATIO FALSE/TRUE POSITIVES VS SCORE FOR GENTLEBOOST ON SERIAL ADDITION	71

FIGURE 65: %TP AND RATIO FALSE/TRUE POSITIVES VS SCORE FOR ADABOOST FOR FORWARD SELECTION	72
FIGURE 66: %TP AND RATIO FALSE/TRUE POSITIVES VS SCORE FOR ADABOOST FOR BACKWARD SELECTION	72
FIGURE 67: %TP AND RATIO FALSE/TRUE POSITIVES VS SCORE FOR ADABOOST FOR FORWARD/BACKWARD SELECTION	73
FIGURE 68: RATIO OF FALSE/TRUE POSITIVES VS % TRUE POSITIVES FOR THE TOP MODELS OF EACH TECHNIQUE	73
FIGURE 69: BREAKDOWN AMONG GROUPS BY SCORE: BLUE 'HIGHLY-LIKELY', GREEN 'LIKELY', AND YELLOW 'SOMEWHAT-LIKELY'	74
FIGURE 70: DISTRIBUTION OF NODES IN VALIDATION SET	75
FIGURE 71: % TRUE POSITIVES AND RATIO FALSE/TRUE POSITIVES VS SCORE FOR VALIDATION SET. TP MEANS TRUE POSITIVE AND FP MEANS FALSE POSITIVE. A SCORE CUTOFF OF 3.1 HAS BEEN PREVIOUSLY DETERMINED BASED ON THE FIFTY-EIGHT PATIENT DATASET. ALL SCORES ARE INCLUDED FOR ILLUSTRATION PURPOSES ONLY. AXIS HAVE BEEN CHANGED TO START AT 0.1 FOR VISUALIZATION PURPOSES.....	76
FIGURE 72: % OF NODES IDENTIFIED BY ANATOMICAL LOCATION OF THE ORIGINAL FIFTY-EIGHT PATIENTS	78
FIGURE 73: EXAMPLE OF A NODE THAT THE PROGRAM COULD NOT FIND, CONTOURED IN RED/GREEN BY PHYSICIAN	80
FIGURE 74: EXAMPLES OF IDENTIFICATION OF TWO EXTERNAL ILIAC NODES AND PARAAORTIC NODE (BLUE) THAT THE PROGRAM CORRECTLY IDENTIFIED	80
FIGURE 75: RATIO OF FALSE POSITIVES TO TRUE POSITIVES IDENTIFIED BY ANATOMICAL LOCATION OF THE ORIGINAL FIFTY-EIGHT PATIENT COHORT	81
FIGURE 76: EXAMPLE OF PROGRAM OPERATION	84
FIGURE 77: EXAMPLE OF STRUCTURE IMPORTED INTO TREATMENT PLANNING SYSTEM. TWO EI/II NODES PROPERLY IDENTIFIED IN THE 'HIGHLY LIKELY' GROUP (BLUE), AND ARTERY FALSELY IDENTIFIED IN THE 'SOMEWHAT LIKELY' GROUP (YELLOW)	85

List of Tables

TABLE 1: FIGO STAGING AND EXTENT OF DISEASE [11].....8

TABLE 2: TYPICAL PELVIC FIELD BORDERS FOR TREATMENT OF CARCINOMA OF THE CERVIX [12].....9

TABLE 3: AMOUNT OF EXPANSION BY DIRECTION EXPANDED OF MASK TO INCLUDE 99% OF THE
PATHOLOGICALLY ENLARGED LYMPH NODES 20

TABLE 4: ALL CRITERIA USED FOR THE CREATION OF THE 3D NODES, AS WELL AS CRITERIA FOR
REMOVAL OF EXTRANEIOUS SURFACES. X IS THE MEASURED VARIABLE, REMOVED IF EQUATION IS
SATISFIED. EXAMPLE SOLIDITY: REMOVE IF X IS LESS THAN 0.85..... 51

TABLE 5: SHAPE FEATURES: RADII. (LEFT COLUMN) THE VARIABLE EQUATION WHICH IS USED BY THE
MODEL, (CENTER COLUMN) THE NAME WHICH IT IS ASSIGNED, AND (RIGHT COLUMN) VARIABLE
NUMBER..... 56

TABLE 6: SHAPE FEATURES: DISTANCE BETWEEN SLICES. (LEFT COLUMN) THE VARIABLE EQUATION
WHICH IS USED BY THE MODEL, (CENTER COLUMN) THE NAME WHICH IT IS ASSIGNED, AND (RIGHT
COLUMN) VARIABLE NUMBER 57

TABLE 7: BASE AND SUBBASE (LEFT COLUMN) THE VARIABLE EQUATION WHICH IS USED BY THE MODEL,
(CENTER COLUMN) THE NAME WHICH IT IS ASSIGNED, AND (RIGHT COLUMN) VARIABLE NUMBER58

TABLE 8: RING AND SUBRING (LEFT COLUMN) THE VARIABLE EQUATION WHICH IS USED BY THE MODEL,
(CENTER COLUMN) THE NAME WHICH IT IS ASSIGNED, AND (RIGHT COLUMN) VARIABLE NUMBER59

TABLE 9: SUBBASE - RING. (LEFT COLUMN) THE VARIABLE EQUATION WHICH IS USED BY THE MODEL,
(CENTER COLUMN) THE NAME WHICH IT IS ASSIGNED, AND (RIGHT COLUMN) VARIABLE NUMBER60

TABLE 10: COMPARISON OF MODELS FROM SERIAL ADDITION 67

TABLE 11: FEATURE FORMULA AND FEATURE NAME FOR ADABOOSTM1 FROM SERIAL SELECTION 68

TABLE 12: COMPARISON OF MAX AVERAGE AUC AND STANDARD DEVIATION BY MODEL..... 68

TABLE 13: FEATURE FORMULA AND FEATURE NAME FOR ADABOOSTM1 FROM FORWARD SELECTION 69

TABLE 14: COMPARISON OF MAX AVERAGE AUC AND STD BY MODEL..... 69

TABLE 15: FEATURE FORMULA AND FEATURE NAME FOR ADABOOSTM1 FROM BACKWARD SELECTION
..... 70

TABLE 16: COMPARISON OF MAX AVERAGE AUC AND STD BY MODEL..... 70

TABLE 17: FEATURE FORMULA AND FEATURE NAME FOR ADABOOSTM1 FROM FORWARD/BACKWARD
SELECTION 71

1. Chapter 1: Introduction

1.1. Cervical Cancer around the World

In 2012 there were approximately 528,000 new cervical cancers cases world-wide (Figure 1), 70% (368,000) of which occurred within Low- and Middle-Income Countries (LMICs) (3). The mortality rate of cervical cancer is approximately half this number (266,000), with LMICs accounting for 70% of the mortality burden.

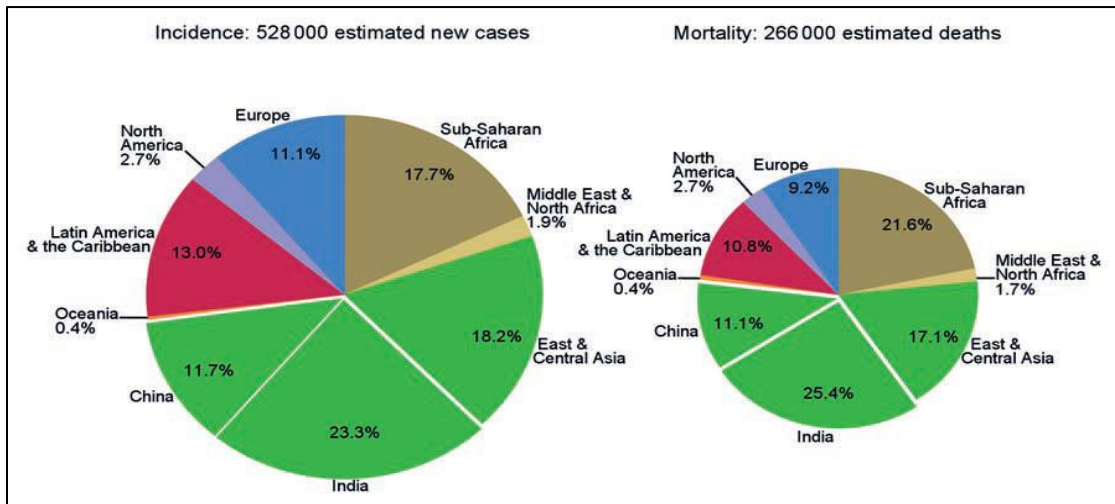


Figure 1: Incidence and Mortality of Cervical Cancer by geographic location (3). Used with permission B. W. Stewart and C. P. Wild, "World cancer report 2014," World Heal. Organ., pp. 1–2, 2014.

These LMICs are defined based on the Human Development Index (HDI) which is a composite of three basic human metrics: a long and healthy life, education, and standard of living, Figure 2.

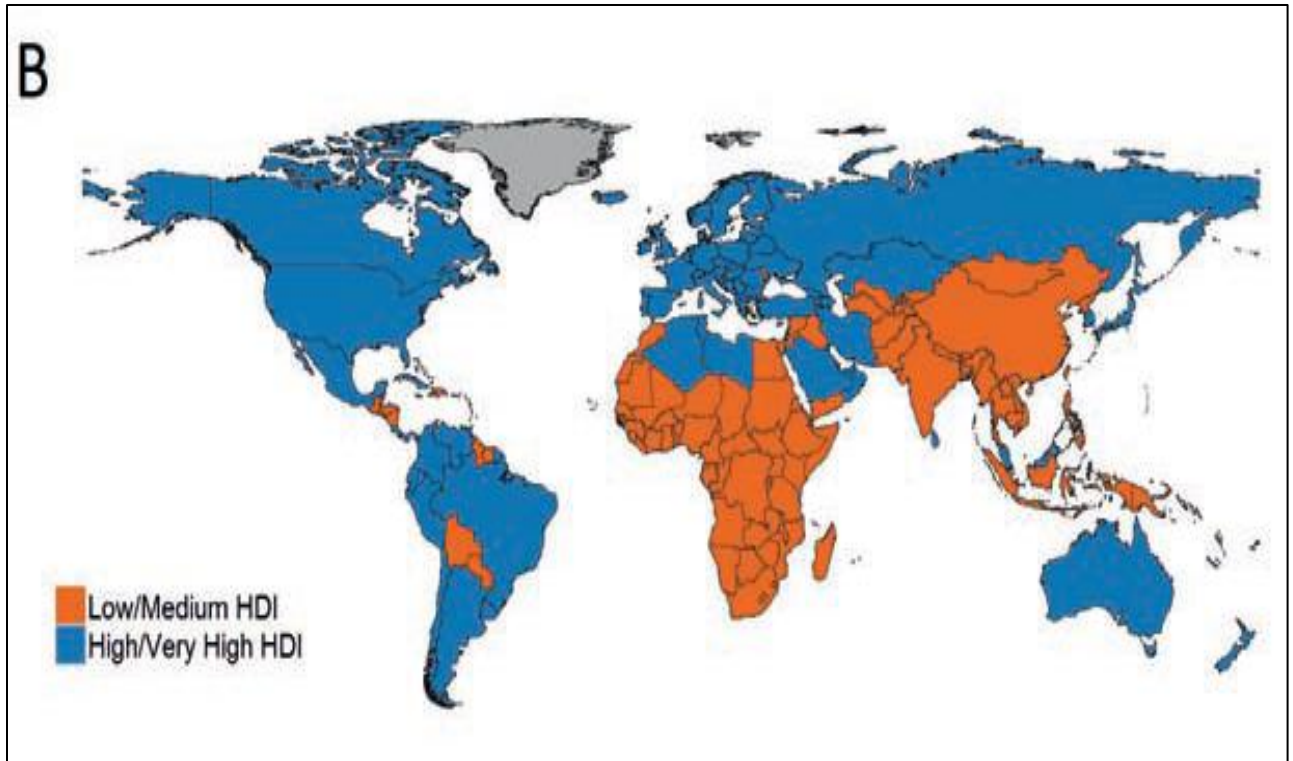


Figure 2: Low/Medium and High/Very High HDI by geographical location (3) Used with permission B. W. Stewart and C. P. Wild, "World cancer report 2014," World Heal. Organ., pp. 1–2, 2014.

The incidence of cervical cancer is particularly significant in southern Africa, India, and parts of South America, as seen in Figure 3 (4).

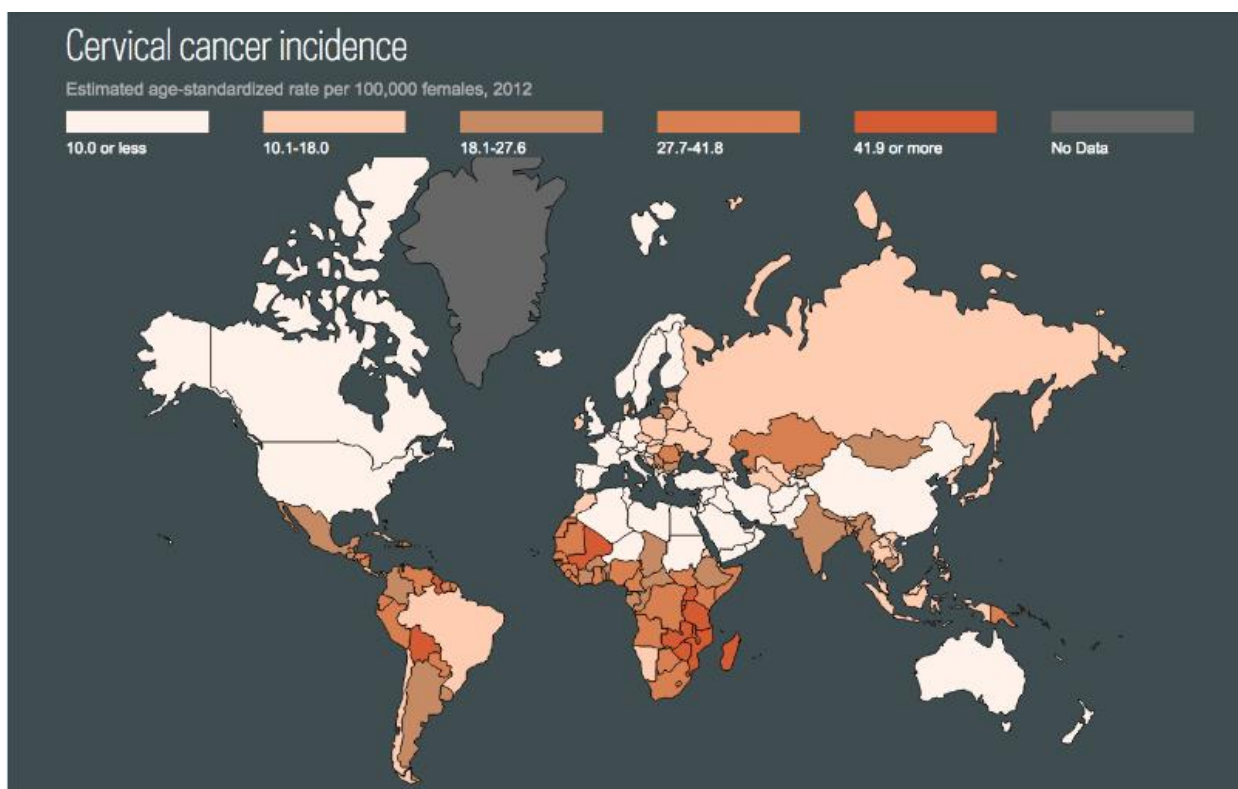


Figure 3: Incidence of Cervical Cancer by Geographical location (4). Used with permission Ferlay, J., H.-R. Shin, F. Bray, D. Forman, C. Mathers, and D. M. Parkin. 2010. Estimates of worldwide burden of cancer in 2008: GLOBOCAN 2008. *Int. J. Cancer* 127: 2893–2917.

While cervical cancer is the fourth most common cause of cancer death among women in the world, it is the second most common cause in LMICs, second only to breast cancer. This is likely due to several factors: the higher prevalence of the Human papillomavirus infection (HPV) in LMICs [3,5], potential lack of PET data for identification of disease or access to necessary treatment resources (linear accelerators, brachytherapy, etc.) (1), and/or lack of resources to optimize individual radiation treatments (6).

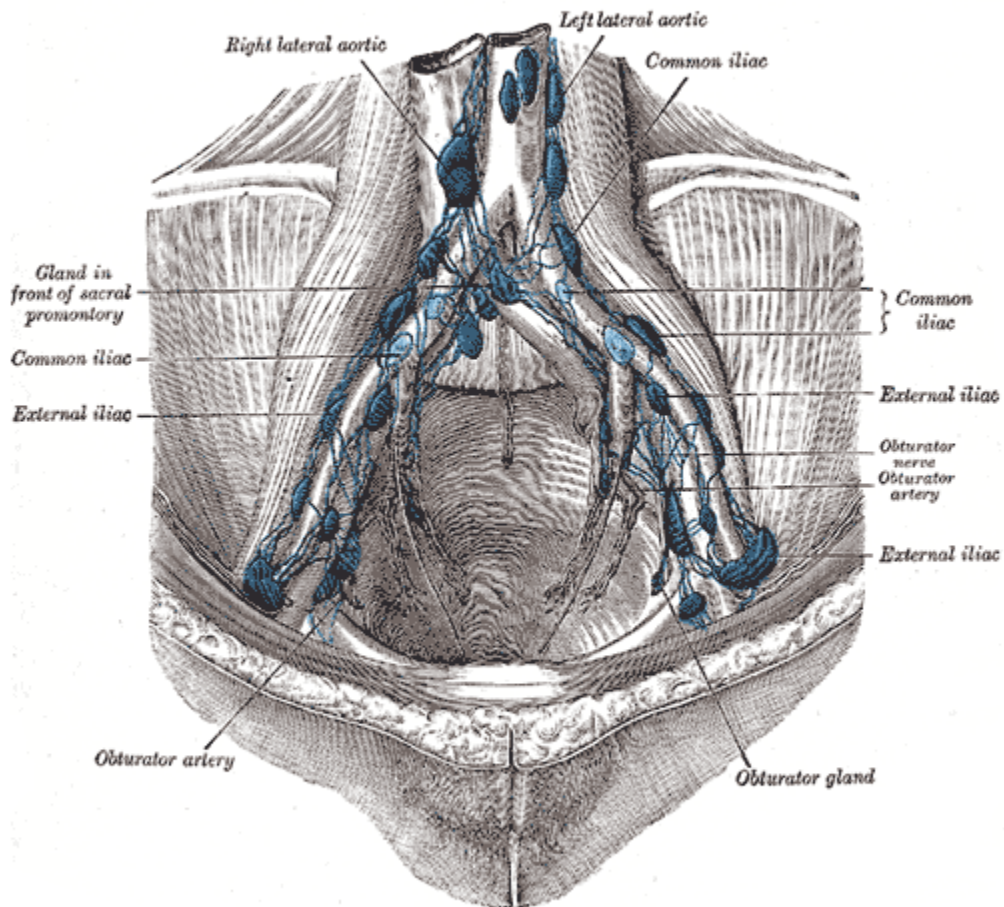
1.2. Anatomical Location of Cervical Cancer

The nomenclature for the characterization of pelvic lymph nodes in cervical cancer patients are based on their location relative to the bifurcation of the aorta and common iliac arteries, and can be broken up into 4 general groups: external/internal iliac, common, obturator, and paraaortic. The external and internal iliac (EI/II) nodes are named due to their proximity to the external and internal iliac artery, the common iliac nodes are any nodes located between the bifurcation of the aorta and the bifurcation of the common

iliac arteries, obturator nodes are those surrounding the obturator artery, and the paraaortic are characterized by their location superior to the bifurcation of the descending aorta (named right and left lateral aortic in Figure 4) (7).

Henry Gray (1825–1861). *Anatomy of the Human Body*. 1918.

FIG. 611



The parietal lymph glands of the pelvis. (Cunéo and Marcille.)

Figure 4: *Anatomical Display of Cervical Lymph Nodes* (7). Used with permission Krahl, V. E. 1960. *Anatomy of the human body (Gray's Anatomy)*. By Henry Gray. Twenty-seventh edition (American Centennial Edition). Edited by Charles Mayo Goss. 1458 pages with 1174 illustrations. Lea & Febiger, 600 Washington Square, Philadelphia, Pa., 1959. *Anat. Rec.* 136: 505–505.

1.3. Identification of Disease

As can be seen in Figure 5, the overall 5-Year survival varies greatly based on the extent of disease.

Localized disease has the highest chance of survival, while distant metastasis has the lowest (8).

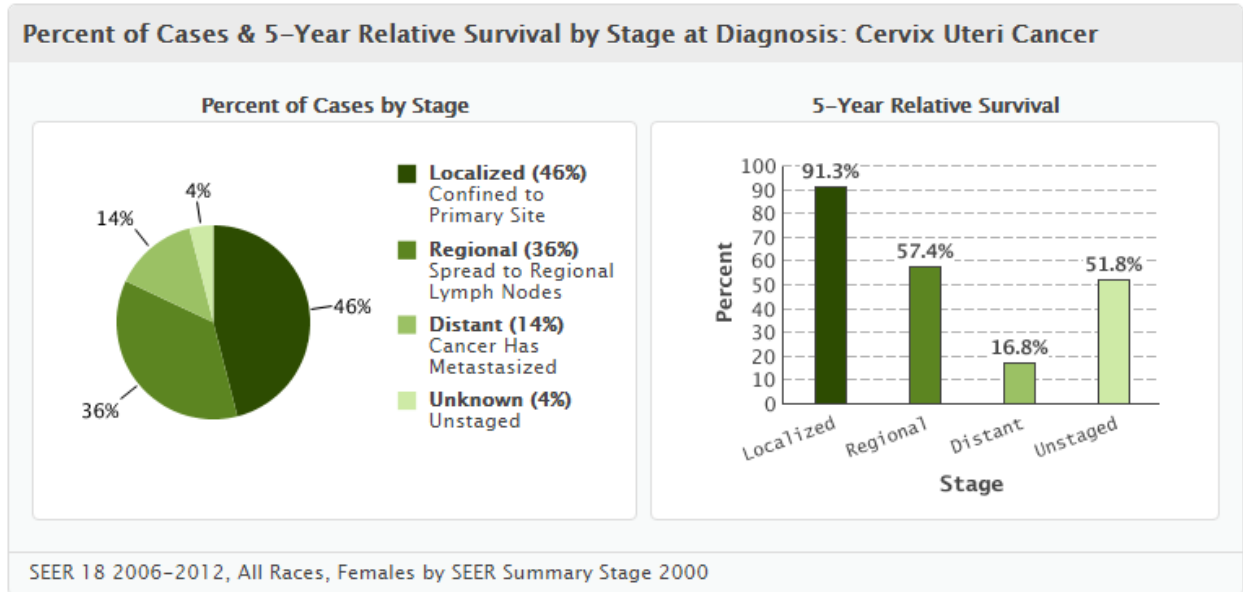


Figure 5: 5-Year Relative Survival by Stage at Diagnosis (8)
SEER. 2013. *Cancer of the Cervix Uteri (Invasive)*,

From Figure 5 it is apparent that the identification of positive lymph nodes and other metastatic sites is especially important in determining the extent disease(9). The current standard of care for the identification of cervical cancer lymph nodes in the US involves the usage of Positron Emission Tomography (PET). PET is particularly successful in identifying both local disease and distant metastasis which is useful for initial staging and restaging of the patient (10). Unfortunately, some LMICs do not have PET to assist in the identification of cervical cancer which has metastasized, Figure 6 (1).

Baseline country survey on medical devices, 2014 update: Medical Equipment – Total density* per million population
Positron emission tomography

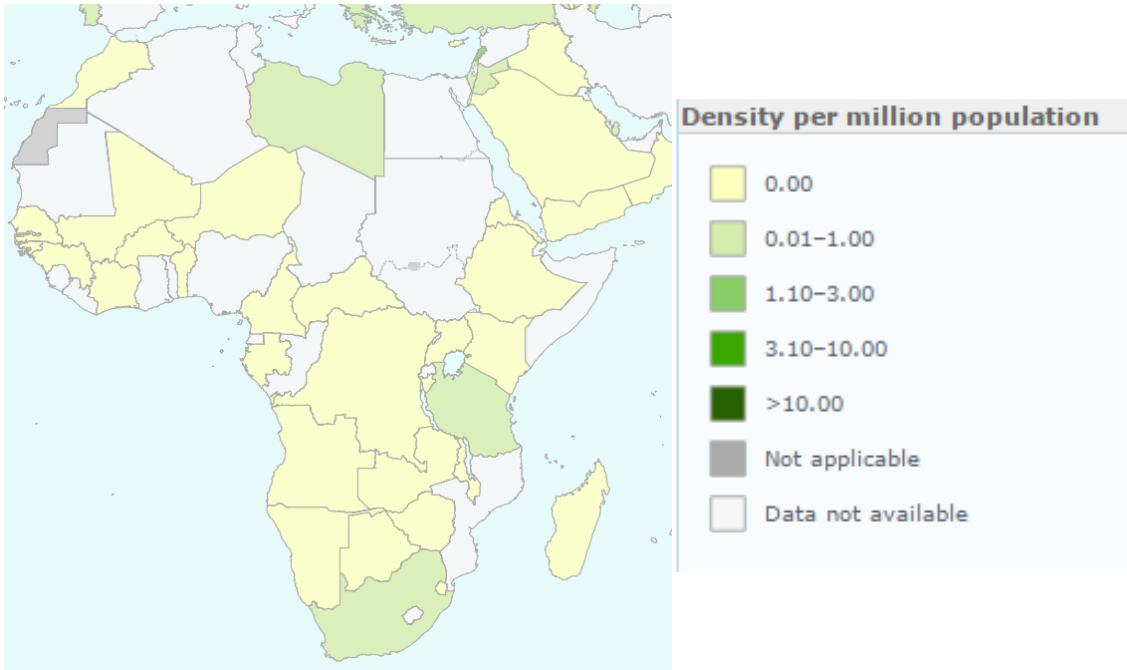


Figure 6: PET Data of Africa where available (1)
“Baseline country survey on medical devices,” World Heal. Organ., 2014

However, these same countries do often have access to CT scanners (1), providing an opportunity to identify disease from the CT rather than the PET scanner, Figure 7.

Baseline country survey on medical devices, 2014 update: Medical Equipment – Total density* per million population
Computed tomography

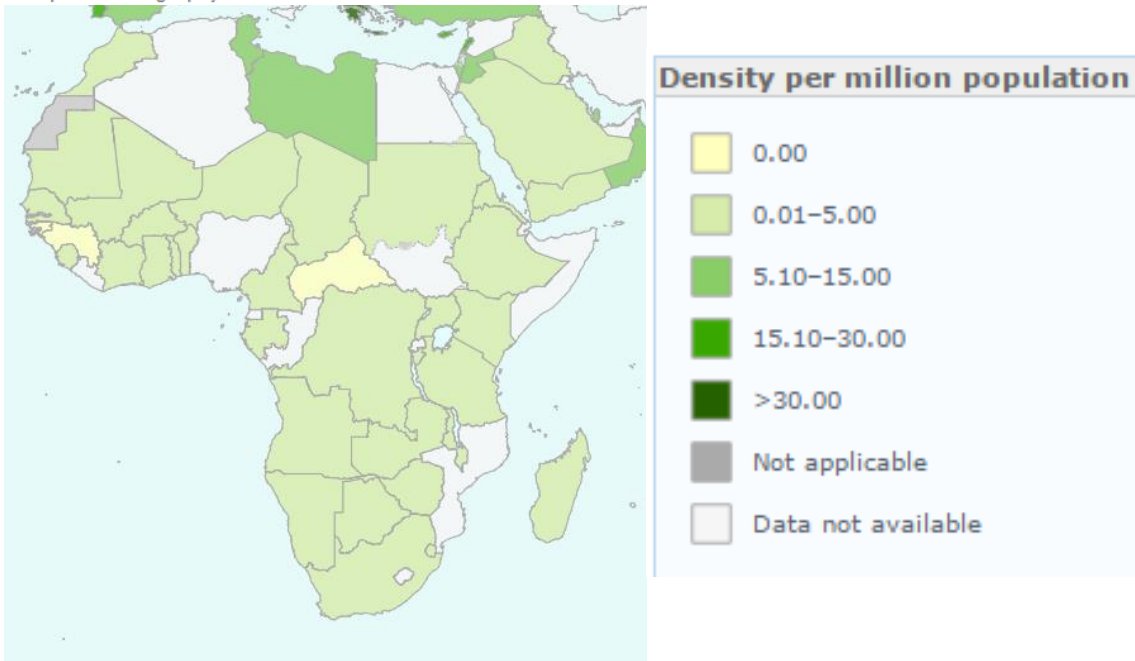


Figure 7: CT Data of Africa where available (1)
"Baseline country survey on medical devices," World Heal. Organ., 2014

1.4. Staging and Treatment of Cervical Cancer

The severity of disease associated with cervical cancer depends on several things: extent of local disease, extent of spread to lymphatic system, and extent of spread to other organs. The Federation of Gynecology and Obstetrics (FIGO) staging of cervical cancer is broken down as seen in Table 1 (11).

Table 1: FIGO staging and extent of disease (11)

Stage	Extent of Disease
0	Carcinoma in Situ
I	Limited to Cervix
Ia1	Microscopic Disease Stromal invasion < 3mm, lateral < 7 mm
Ia2	Microscopic Disease Stromal invasion < 3mm & > 5mm, lateral < 7 mm
Ib1	Macroscopic lesion < 4cm in greatest dimension
Ib2	Macroscopic lesion > 4cm in greatest dimension
II	Extension to uterus/parametrial/vagina
Ila1	Involvement of upper two thirds of vagina <i>without</i> parametrial invasion, < 4cm
Ila2	Involvement of upper two thirds of vagina <i>without</i> parametrial invasion, > 4cm
Ilb1	Involvement of upper two thirds of vagina <i>with</i> parametrial invasion
III	Extension to pelvic side wall and/or lower third of vagina
IIIa	Involvement of lower third of vagina
IIIb	Extension to pelvic side wall and/or hydronephrosis
IV	Extension to adjacent organs or beyond true pelvis
IVa	Extension to adjacent organs e.g. bladder
IVb	Distant metastases

A paper in 2016 offered recommendations for clinicians and policy-makers for treatment of cervical cancer in resource limited regions, advocating for the inclusion of EBRT if available for patients with IB-IVB cervical cancer (6). EBRT in this case came most often in the form of a four-field box or parallel opposed beams as well as boost treatment of any pathologic lymph nodes.

The four-field box can be created based on bony landmarks described in Table 2 (12), or from a CT based plan. It has been shown that conventional four-field radiotherapy based on bony landmarks does not always fully encompass the target volume and that CT based treatment planning offers significant improvements ((13),(14),(15),(16)).

Table 2: Typical Pelvic Field Borders for Treatment of Carcinoma of the Cervix (12)

Typical Pelvic Field Borders for Treatment of Carcinoma of the Cervix		
Field Name	Border	Bony Landmarks
AP-PA fields	Superior	L4-L5 or L5-S1 inter-vertebral space
	Inferior	Lower border of the obturator foramen. In the case of vaginal extension, there should be a distal margin of 3-4 cm from the most caudal extent of the vaginal involvement
	Lateral	2 cm lateral to the pelvic brim to adequately cover the external iliac and obturator nodes
Lateral fields	Superior	L4-L5 or L5-S1 inter-vertebral space
	Inferior	Lower border of the obturator foramen. In the case of vaginal extension, there should be a distal margin of 3-4 cm from the most caudal extent of the vaginal involvement
	Anterior	Anterior face (convex) of the pubic symphysis
	Posterior	Include all the sacral hollow with margin (1-1.5 cm)

The four-box field comes in the form of an AP, PA, and two lateral fields (17), as shown in Figure 8. The borders, as described in Table 2, can be more easily visualized in a coronal and sagittal view, Figure 9 (18).

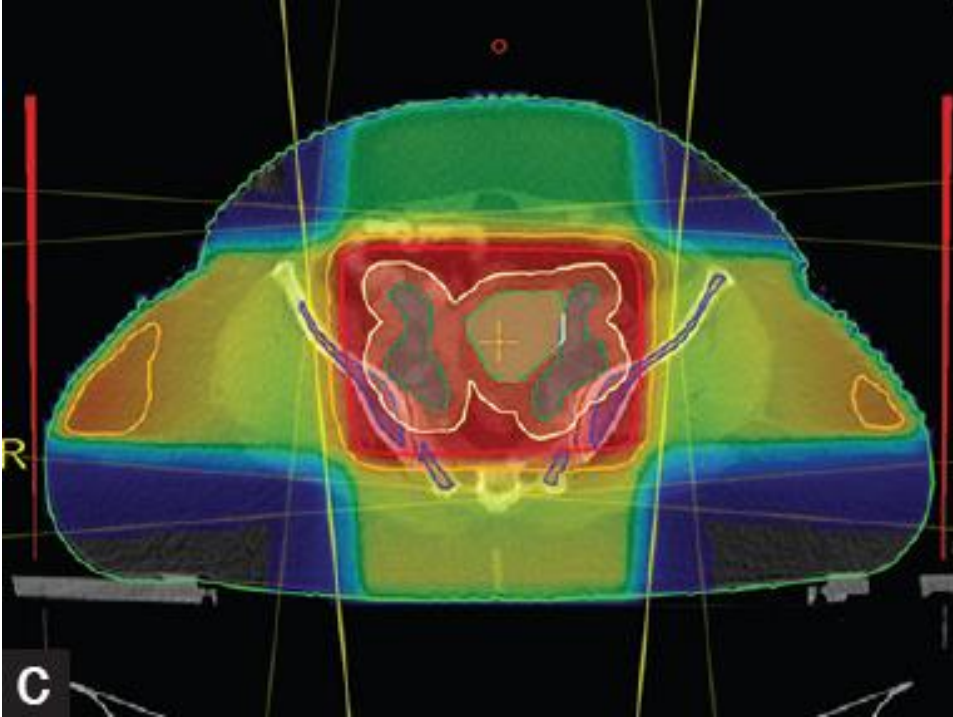


Figure 8: Four-box field, AP, PA, and two lateral treatment fields (17). Used with permission.
Avinash, H. U., T. R. Arul Ponni, M. G. Janaki, A. S. Kirthi Koushik, and S. M. Kumar. 2015. A prospective dosimetric and clinical comparison of acute hematological toxicities in three-dimensional conformal radiation therapy and intensity modulated radiation therapy with concurrent chemotherapy in carcinoma cervix. *J. Cancer Res. Ther.* 11: 83–7.

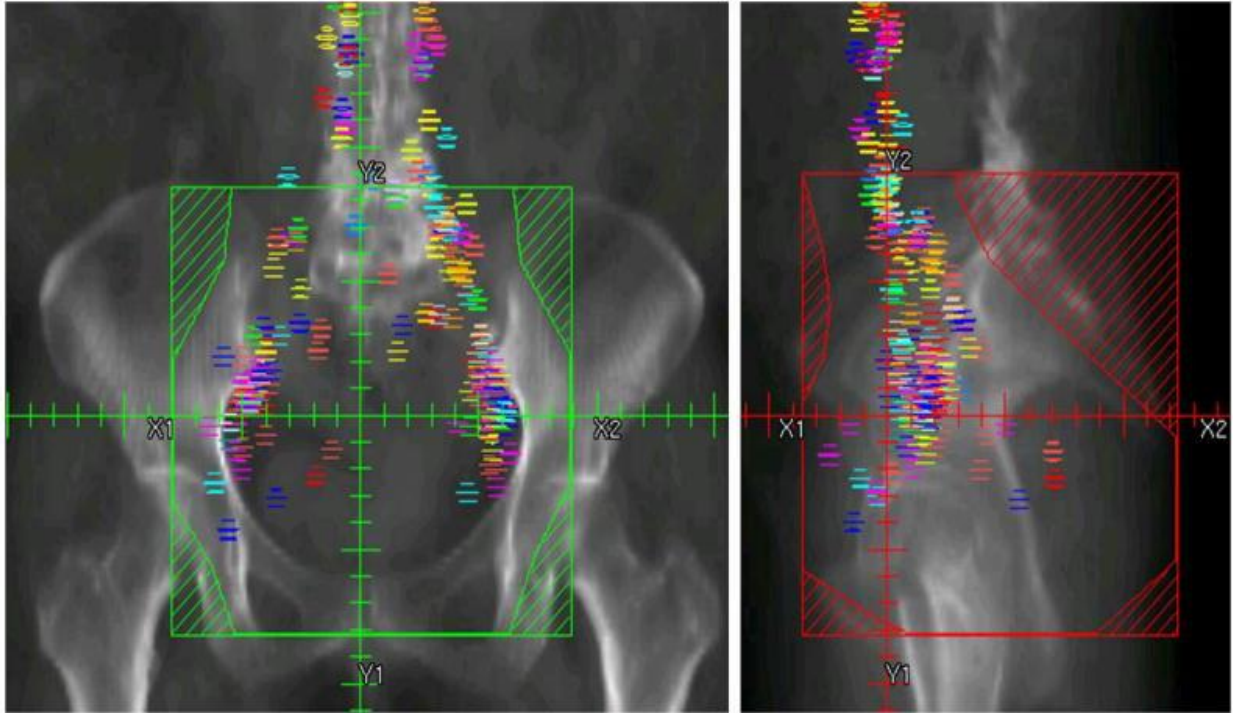


Figure 9: (left) Coronal and (right) Sagittal view of bony-anatomy blocks, green and red respectively, in four-field box treatment. The multicolored sections are nodes from 50 patients mapped onto a single patient to create an atlas patient mask (18) Used with permission

Fontanilla, H. P., A. H. Klopp, M. E. Lindberg, A. Jhingran, P. Kelly, V. Takiar, R. B. Iyer, C. F. Levenback, Y. Zhang, L. Dong, and P. J. Eifel. 2013. Anatomic distribution of [18F] fluorodeoxyglucose-avid lymph nodes in patients with cervical cancer. *Pract. Radiat. Oncol.* 3: 45–53.

Radiation therapy in patients who have low risk (disease likely involving only microscopic regional disease) are usually treated with 45 to 50 Gy, utilizing EBRT to the pelvic lymph nodes. If disease involving pathologically enlarged lymph nodes has been identified, they are often given a boost of radiation to a total dose of 56-66 Gy for small nodes and 65 Gy or more to ‘bulky nodes’ (19).

To ensure optimized treatment of cervical cancer disease it is important for any identified metastatic disease to the lymph nodes be included and boosted (20). The superior aspect of the four-field box, which extends to the L4-L5 or L5-S1 interspace, does not include the para-aortic node anatomy. Physicians, through the usage of PET data and previous experience, would determine if the superior aspect of the four-field box needs to be raised to include potentially cancerous nodes.

The incidence of lymphatic involvement in cervical cancer varies based on the FIGO score, with stages IB, IIB, and IIIB having approximately a 15, 30, and 50% chance of lymphatic involvement, respectively (12). Also patients with stage IIB or IIIB are expected to have para-aortic disease in 20-30%

of the cases, although it is rare for para-aortic nodes to occur without other nodal involvement (21). In lieu of PET data and previous experience, it was theorized that a Computer-Aided Detection (CAD) system could assist the physicians in identifying this disease.

1.5. Computer-Aided Detection/Diagnosis (CAD) Systems

Since there is currently no CAD program for identifying cervical cancer nodes, particularly with the lack of PET data, a literature review of CAD systems in breast cancer and lung cancer was used as a potential comparison.

CAD systems can be broken up based on two general goals: Computer-Aided Detection (CADe) and Computer-Aided Diagnosis (CADx). CADe systems are normally created to identify potential disease, whether that is based on location or other features. CADx systems are usually created to evaluate suspicious structures and assist in differentiating disease; i.e malignant, benign, etc. These systems often differentiate between potentially pathologic objects from normal objects based on criteria such as intensity, surface features, size, etc.

The goal of these systems is to help assist physicians identify disease which they might not be able to identify on their own. This can improve patient treatments and outcome, although these systems can also run the risk of providing incorrect feedback. It is for this reason that the CAD systems must often have not only a high sensitivity, or an ability to identify disease, but also have a high specificity, or ability to ignore normal structures.

In the past decade, CAD systems which assist in the detection of lung cancer have an average false to true positive rate of approximately 11 to 1, although some are achieving 5 to 1 (22–29). This is better than some breast cancer systems which range from a ratio of 35 to 5 false to true positives, respectively (30, 31). These systems generally have sensitivities of 90% and above.

1.6. Hypothesis

Quantitative image features measured on non-contrast CT images are capable of identifying 75% of the pathologically enlarged lymph nodes in cervical cancer patients, with a false/true positive ratio of 5 to 1.

1.7. Specific Aims

The hypothesis will be tested with the following specific aims:

- 1) Develop a program capable of identifying potentially pathologically enlarged lymph nodes from non-contrast CT images*
- 2) Create and optimize a machine learning model which differentiates pathologically enlarged lymph nodes from normal tissues*

1.8. Organization of Thesis

The specific aims are divided into two chapters: Chapter 2: Identification of Potentially Pathologically Enlarged Lymph Nodes, which will address Specific Aim 1, and Chapter 3: Identification of differentiating features and optimization of model which will address Specific Aim 2. Final discussion and conclusions are presented in Chapter 4: Discussion.

2. Chapter 2: Identification of Potentially Pathologically Enlarged Lymph Nodes

2.1. Introduction

Lymph nodes have often been described as spherical or banana shaped in their appearance (32) and can appear circular in their axial cross section images. It was theorized the nodes could be identified based on their general circular appearance within axial slices and then connected into 3D structures. The steps taken for the identification of the positive lymph nodes in this program were first to identify all 2D axial slices of the node and then connect them into a 3D structure similar to their true appearance.

2.2. Data Acquisition

The non-contrast CT scans of fifty-nine patients from 2006-2013 with FDG-avid lymph nodes who had pretreatment PET/CT were retrospectively obtained from the electronic medical record. One patient was excluded due to presence of rectal contrast which had the potential to cause problems with the deformable image registration, leaving fifty-eight patients. These fifty-eight patients contained a total of 154 pathologically enlarged ($> 1\text{cm}$) lymph nodes of which 4 were located within the inguinal region, 91 in the External/Internal Iliac (EI/II) region, 25 in the common Iliac region, and 34 in the Para aortic region, see Figure 10. These patients were used for the testing and training of the program.

A validation set of twenty cervical cancer patients with pre-treatment PET/CT from MD Anderson were acquired and are described in Chapter 3.7 Validation Set.

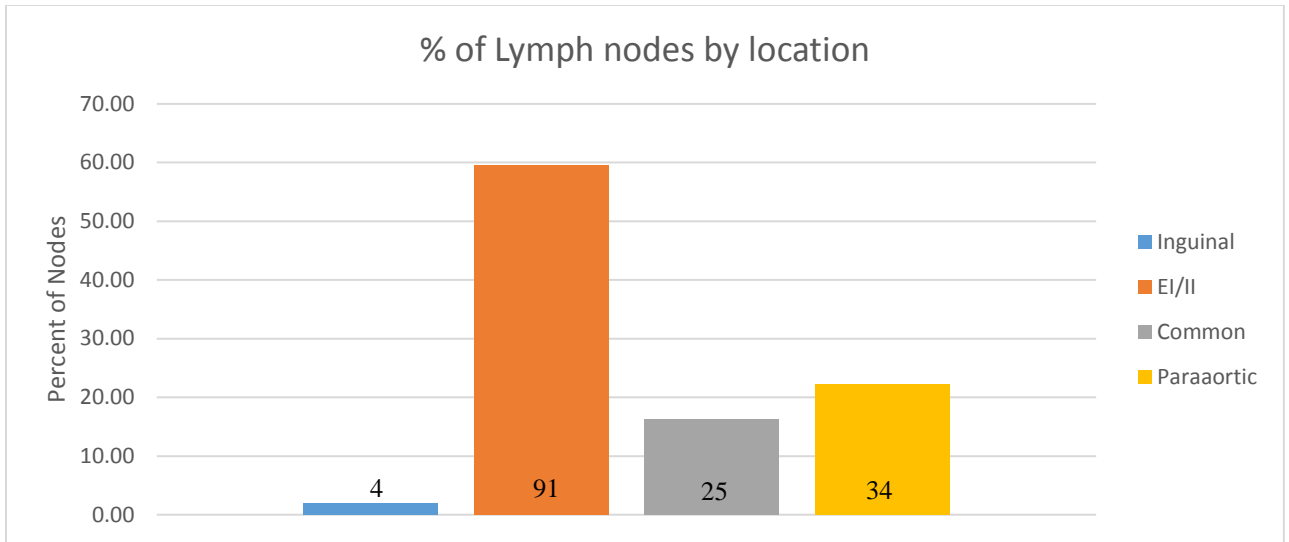


Figure 10: Distribution of pathologically enlarged lymph nodes in the fifty-eight patient dataset

The positive lymph nodes of all seventy-eight patients had been previously contoured by physicians at MD Anderson cancer center during individual patient treatment. To create these contours, physicians relied on previous expertise in identification of nodal disease in the CT scans and PET data to identify tissues which are likely cancerous Figure 11.

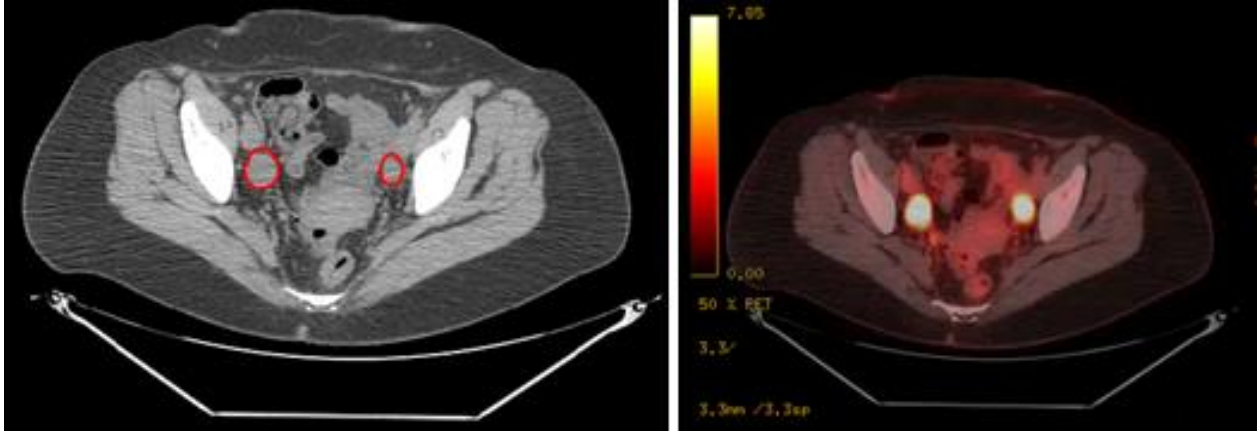


Figure 11: (left) Contours from physicians of two external iliac nodes, shown in red. (right) The associated PET data of these nodes. Note that the bright spots show a marked increase in FDG, assisting the physician to determine if they are disease

2.3. Deformation of Region of Interest (ROI) to Patient

Reducing the search space for the program will have the benefit of decreased computational time.

Smaller search space means less area to look through, which will reduce the number of normal tissues identified. To reduce the search space on each patient, a region of interest was determined where pathologic nodes would likely occur, and this search space was deformed onto each new patient. This

region of interest was created in a previous work from 50 women who had lymph-node metastases (18). These metastases were all mapped onto an individual patient, Figure 12.

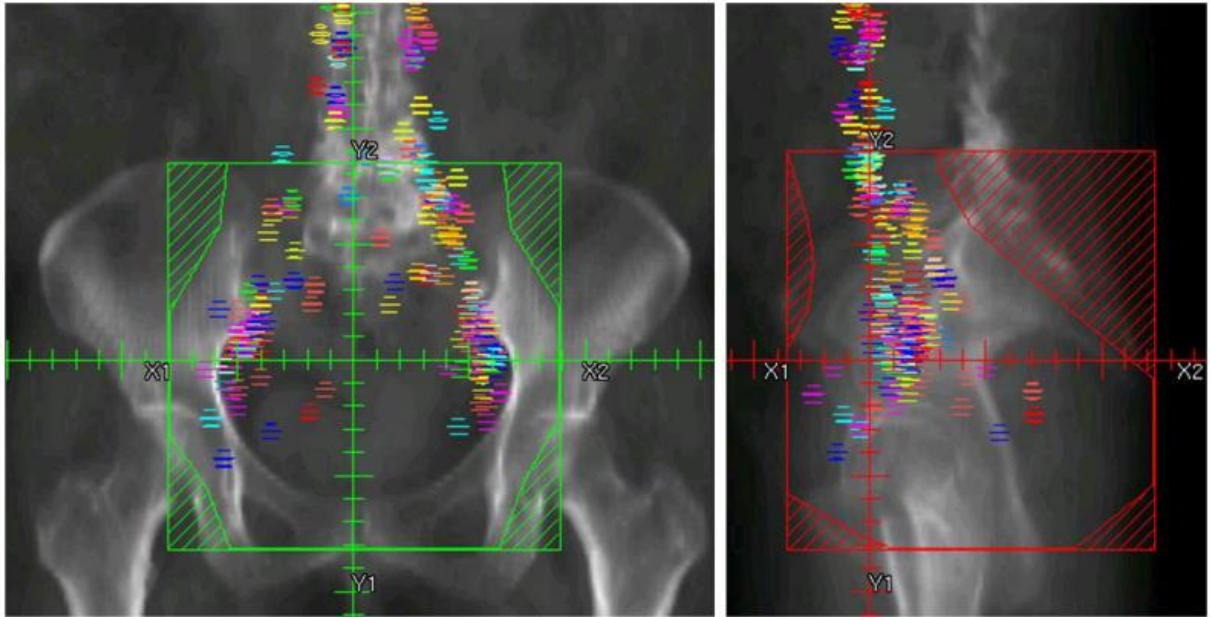


Figure 12: The multicolored sections are nodes from 50 patients mapped onto a single patient. These nodes were used to create an atlas patient mask. Used with permission (18)
Fontanilla, H. P., A. H. Klopp, M. E. Lindberg, A. Jhingran, P. Kelly, V. Takiar, R. B. Iyer, C. F. Levenback, Y. Zhang, L. Dong, and P. J. Eifel. 2013. Anatomic distribution of [18F] fluorodeoxyglucose-avid lymph nodes in patients with cervical cancer. *Pract. Radiat. Oncol.* 3: 45–53.

From these known nodes, a region of interest was generated, shown on the left in red in Figure 13 (18). This region of interest was then deformed onto each new patient using an in-house Demons based software (33),(34) as illustrated in Figure 13.

The ‘demons’ algorithm was implemented as a fully automatic grayscale-based deformable image registration algorithm. Demon’s algorithms can be broadly categorized into two groups: feature-based and grayscale image-based. Feature-based algorithms attempt to minimize the difference between two images based on features, such as land mark points or reference fiducials. Grayscale image-based algorithms, like that used in this project, use voxel data directly to minimize the differences in intensity between the images. In order to make this algorithm as reproducible and robust as possible, a bone window (1050) and level (225) were implemented for all patients during deformation. To assist in the deformation of the contour to the new patient, the deformable region was defined to extend just superiorly to the mask and

inferior to the femoral heads. This is done manually on each patient; the automation of this step is currently under production.

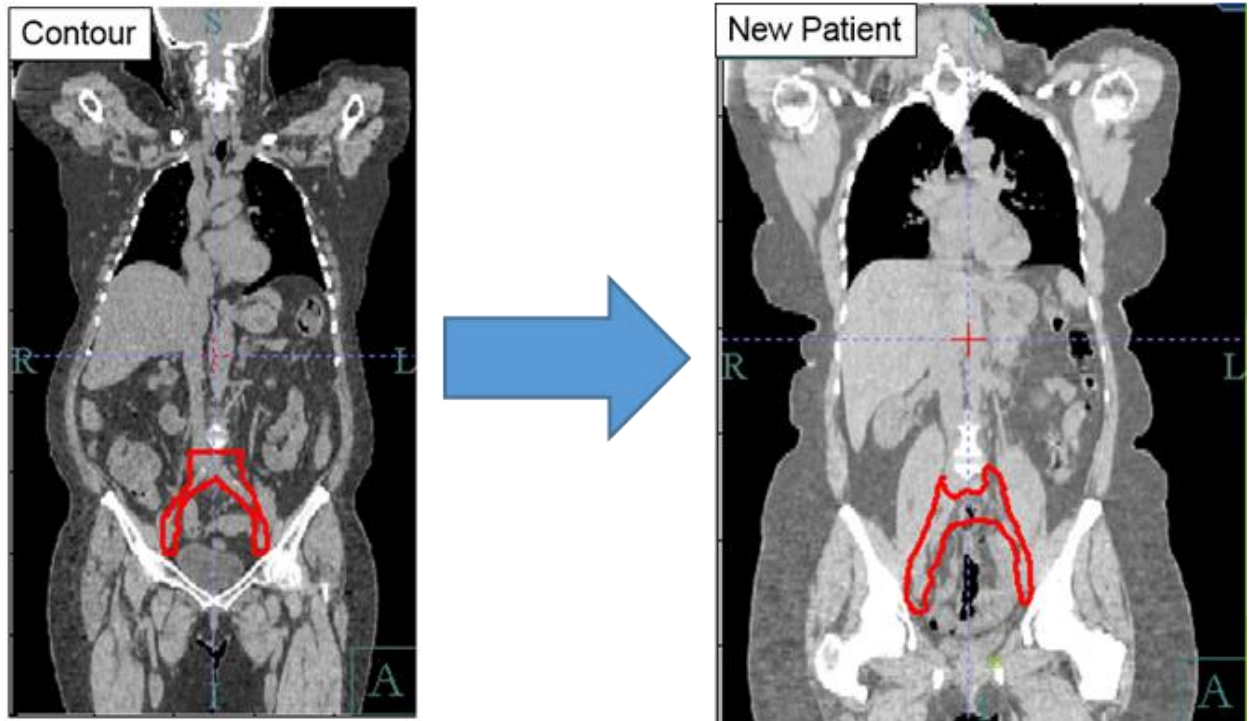


Figure 13: (left) Deformation of contour from atlas patient onto (right) new patient

The mask which was provided from this work often stops inferior to the common and paraaortic region. For this reason expansions are required to ensure all possible disease can be identified.

2.4. Expansion of Mask

We found that this mask, directly transferred to the new patients, did not fully encompass the potential location of the lymph nodes described in the training dataset, Figure 10. To ensure the inguinal, iliac, sacral, and para-aortic nodes were included within the region of interest, expansions of the masked region in all directions were necessary, as described below.

2.4.1. SI Expansion

To ensure the inclusion of potential para-aortic and common lymph nodes, the mask was expanded in the superior direction. These nodes are likely to be excluded from the basic four-field box plan and are thus their identification is very important for treatment modification purposes.

The mask was extended superiorly until every axial slice of each node on all patients was contained inferior to the most superior slice. Based on the locations of the nodes with respect to the deformed mask, as shown in Figure 14, a superior expansion of 75 mm ensured any possible metastatic nodes would be identified inferior to the most superior slice across the fifty-eight patient cohort. This large superior expansion was necessary due to the lack of a paraaortic mask. The mask used therefore had to be projected superiorly to compensate.

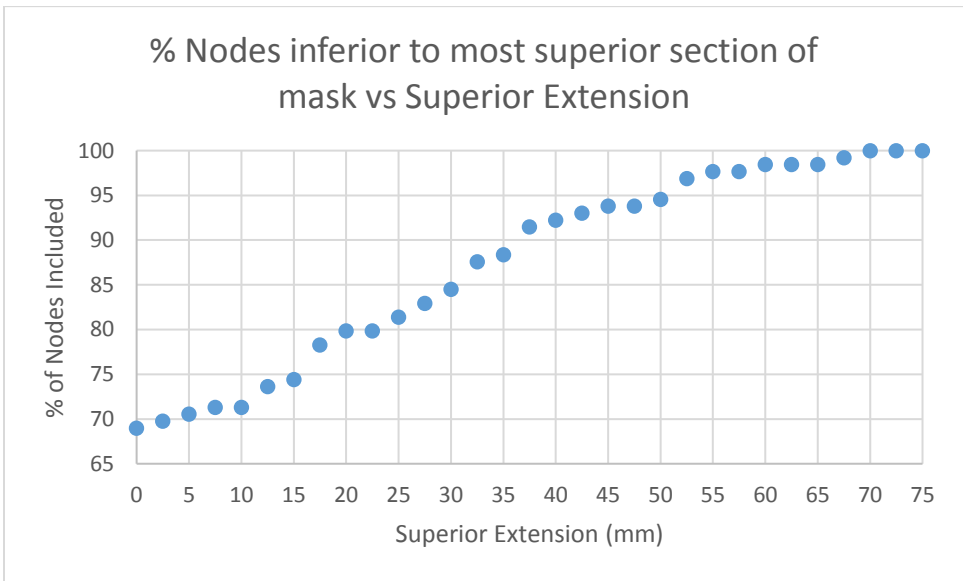


Figure 14: Percentage of lymph nodes inferior to the most superior slice of the masked region vs superior extension. An extension of 75 mm was selected in the final model.

Similarly, in the inferior direction, the mask was extended until every axial slice of all pathologically enlarged nodes were included superior to the most inferior slice. The data shown in Figure 15 shows that an inferior extension of 25 mm ensures all nodes from the fifty-eight patients were located superior to the most inferior slice.

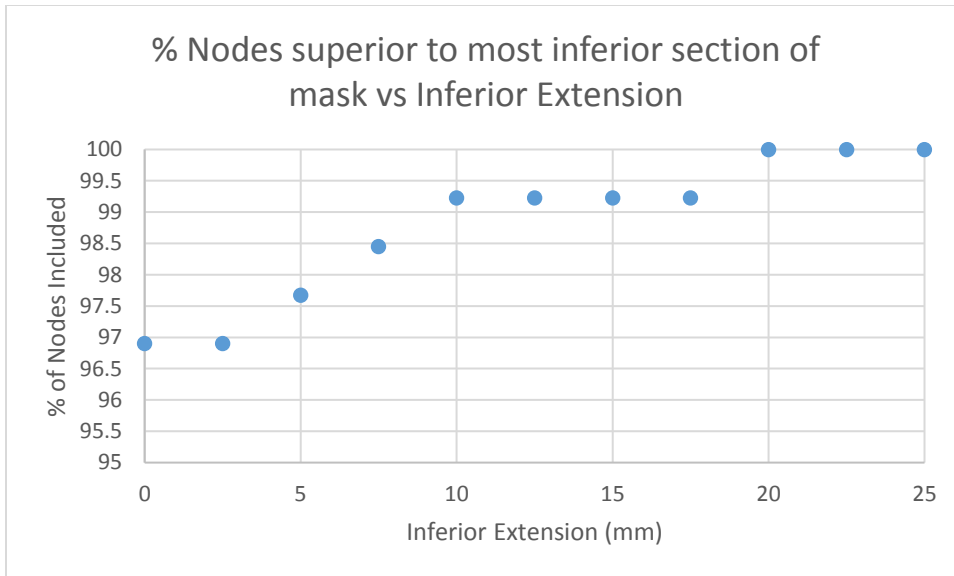


Figure 15: Percentage lymph nodes superior to the most inferior aspect of the mask vs inferior extension. An extension of 25 mm was selected in the final model.

2.4.2. Axial Expansion

Despite being located within the SI range of the mask, some nodes were still not contained completely within the masked region of interest. To correct for this, a radial expansion was evaluated to ensure proper inclusion of the lymph nodes. The results shown in Figure 16 indicated that a radial expansion of 13 mm covered 99% of all possible positive cervical cancer lymph nodes within the fifty-eight patient cohort.

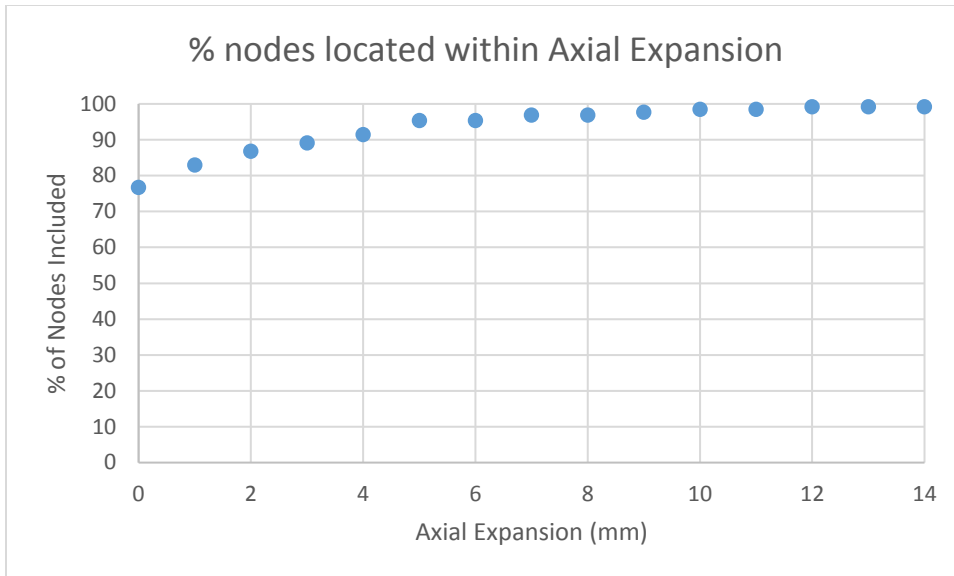


Figure 16: Percentage of nodes included within masked region vs radial axial expansion

The final results of all the expansion, SI and Axial, are summarized in Table 3.

Table 3: Amount of expansion by direction expanded of mask to include 99% of the pathologically enlarged lymph nodes

Direction of Expansion	Amount of Expansions Required
Superior	75 mm projection superiorly of mask
Inferior	25 mm projection inferiorly of mask
Axial	13 mm radial expansion of mask

2.5. Identification of Potential Nodes

2.5.1. Introduction

As stated previously, Matlab contains a function known as `regionprops`, which is useful in the identification of nodal surfaces based on the 2D images. `Regionprops` does this by taking a binary image and exporting out a number of requested features. The outputs requested were the Centroid and the Area for each non-connected structure. These two values can be used to characterize any surface within the image, with the Centroid pointing to the row and column of its center, and a radius for the circle of equivalent area from the Area.

Consider a circle with radius 10, placed at the center of a 100x100 square, this can be thought of as an axial cross section of a spherical lymph node (Figure 17, left). `Regionprops` will generate Centroid values

of 50,50 and an area of 100π (Figure 17, right). The area can be converted to a radius for a circle of equal area as $\text{radius}=\sqrt{\text{Area}/\pi}$.

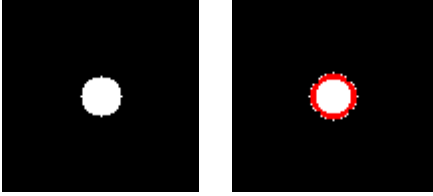


Figure 17: Identification of a single binary circle with *regionprops*

Note, however, if there are two circles which are touching, the function still only generates a single centroid and area, as seen in Figure 18.

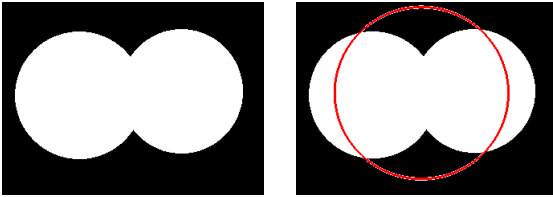


Figure 18: Identification of connected binary circles, as a single object with *regionprops*

The goal then was to transform the raw CT data image into a binary image, which *regionprops* can then be used to identify potential positive nodal surfaces.

2.5.2. Binary Thresholding

Attempting to threshold raw CT data based on HUs alone can have poor results, as shown in Figure 19, where bone thresholding shows dark regions placed throughout the normal tissue. Because of this, Gaussian smoothing was considered. Without smoothing the thresholding can appear grainy (see Figure 19, left) and the ability for the Laplacian of the Gaussian (LoG) edge detection (explained in the following sections) which was needed to separate structures becomes more difficult due to heterogeneity of the HUs within the tissues, which results in erroneous edges. A large sigma value for the Gaussian smoothing will result in a better homogeneity within the node, but runs the risk of removing the edges between a node and normal tissue, making it more difficult to identify both of these independent structures. The sigma value for the Gaussian smoothing was set at 1mm, based on the evaluation of patients with nodes in close proximity to normal structures, example Figure 19.

After smoothing, Hounsfield Unit thresholding was used to mask out the bone (HU values greater than 125) in the image. Values which are associated with bone are instead converted to -50, Figure 19, since -50 HU is lower than the binary thresholding cutoff, which will be explained shortly. This was done because, particularly in the para-aortic region, nodes are often proximal to bony structures, and in a binary image it was desired for the two to be separated. A more thorough explanation for this is explained in the remaining chapter.

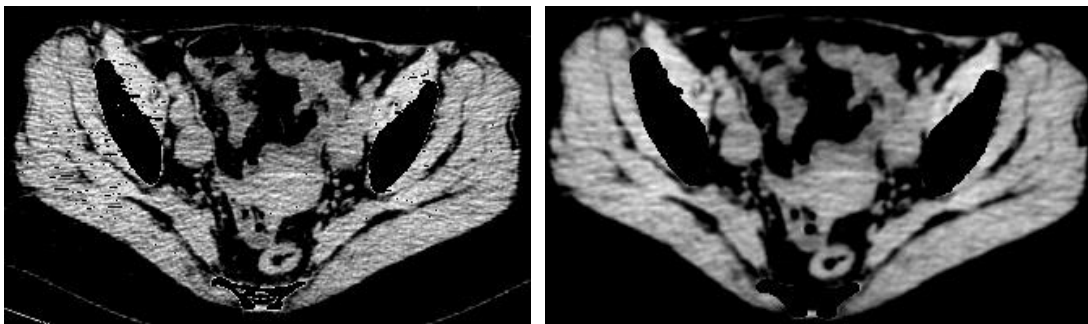


Figure 19: Note the difference in appearance after HU thresholding of the non-filtered image (left) vs the filtered image (right), in particular if the bone thresholding was done on the non-smoothed image vs smoothed image.

If the node was not abutting any other structures it can easily be identified on the binary map and imposed back onto the original image with regionprops, Figure 20. The image was turned into a binary

with the threshold value set as -20 HU, a comparison of different HU values is shown later in Figure 25.

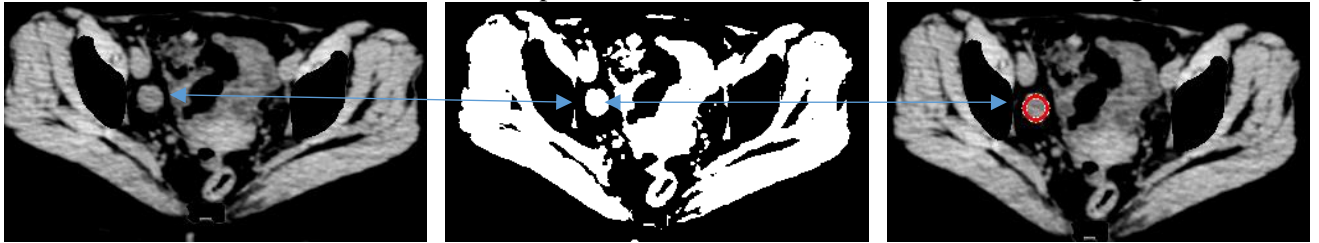


Figure 20: Internal iliac node (left), not being attached to anything else on the binary image (center), is identified using region props as a unique surface (right).

When the binary image of a node was not abutting against other normal tissue structures, regionprops identified a potential nodal surface correctly. However, in situations where the node was connected to another structure within the binary map, it was unable to separately identify the potential node, and would instead identify both as a single object, see Figure 18. Therefore, a method of separating the node from normal structures in the binary map needed to be created.

We developed two approaches to separate a node and normal tissue which are connected within the binary image. In the first case, the node and normal tissue were pressed into each other, but are separable enough that simple erosion methods can separate them (Figure 21, a). In the second case, where the node and tissue were overlapping, edge-detection techniques from the Gaussian smoothed image was used to separate them (Figure 21, b).

These two scenarios can be seen in Figure 21, where the node on the left (a) is pressing into the iliac artery, and the node on the right (b) is nearly indistinguishable on the binary image from the iliac artery. These nodes are the same nodes shown in Figure 11.

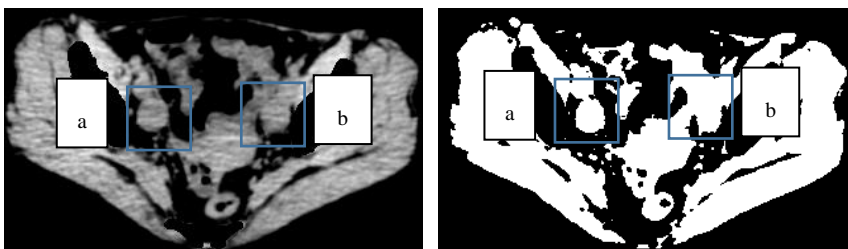


Figure 21: Axial slice of two IJ nodes, a) connects to artery anteriorly on the binary image and b) is nearly indistinguishable from the normal tissue on the binary image

Our solution to these two situations are explained below, where the node (a) can be identified with erosion and dilation correction, while (b) required edge detection along with erosion and dilation correction.

2.5.3. Erosion and Dilation

The largest challenge with identifying pathologic nodal tissues was separating them from surrounding normal tissues into which they often press against or collapse, especially nearby arterial structures. Particularly in the common and paraaortic region, there appeared to be a tendency for lymph nodes to be present directly against normal structures, such as the descending aorta or the left or right common iliac arteries. In the EI/II region, the nodes tend to collapse into the bladder or the arterial structures, Figure 22.

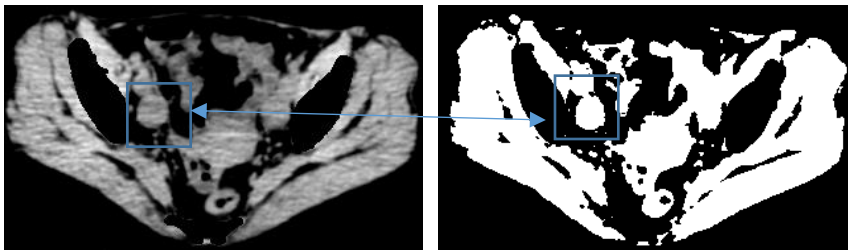


Figure 22: (left) Axial image converted into (right) binary image to show connection of lymph node with normal tissue

If the binary image in Figure 22 is eroded to the point that the node and artery are no longer touching, the node can be identified as a single surface.

Theory:

Erosion was performed through the usage of circular image filters of increasing radii on the binary image. After erosion by a matrix circle with radius, $R_{Erosion}$, the new area will be measured as

$$A_0 = (\sqrt{A_1} - R_{Erosion}\sqrt{\pi})^2$$

Where A_1 is the true area of the object without dilation, and A_0 is the newly measured area. From this point a centroid and area are calculated for each unconnected binary surface. While the centroid could be of the correct spot of the no longer connected surfaces, the measured area will be less than it was originally, (Figure 23, center).

The area can be corrected, however, through the usage of the following equation, where $R_{Erosion}$ is the radius of the matrix circle:

$$A_1 = (\sqrt{A_0} + R_{Erosion}\sqrt{\pi})^2$$

The centroid value can thus be maintained, while the area corrected for the amount of erosion, (Figure 23, right).

An example of this can be seen in Figure 23, where 13 overlapping circles are eroded and area corrected to identify the 13 independent circles.

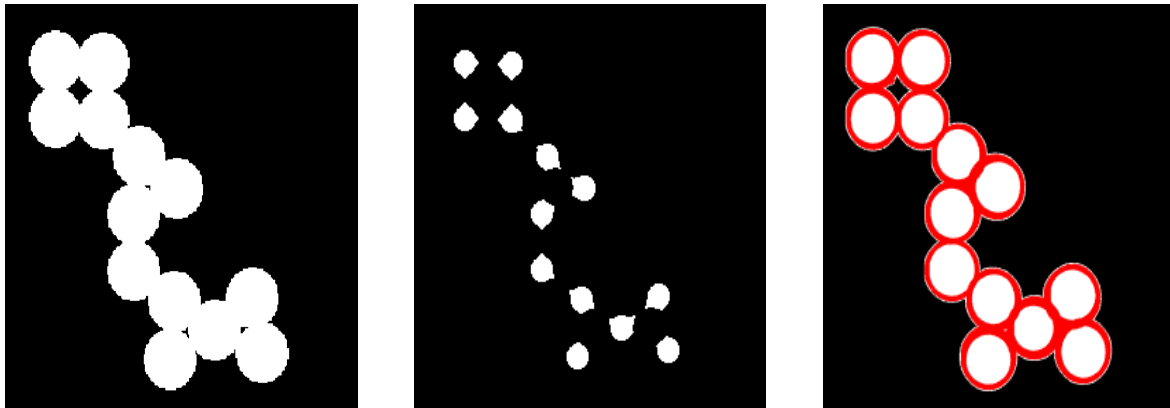


Figure 23: (left) Image of circle before erosion filtering, each with an area of 375π . (center) After erosion filtering of a circular matrix with radius 11 pixels, each spot has area 70π . (right) Maintaining the centroid values found from the center image and correcting back for the amount of erosion, each circle correctly identified with area around 375π

Practice:

As long as the node and normal structure are not largely overlapping, they can be eroded down into independent surfaces, Figure 24 blue square.



Figure 24: (left) Binary where lymph node and artery are connected (center) Image after erosion to the point which structures are separated (blue) and where erosion was unable to separate (red) (right) Corrected area for erosion, final identification. Note that the node within the blue box has been identified, but the one in the red box has not been.

One of the issues encountered with this was that after the circle had been eroded enough to identify the node, every erosion after that will result in the same circle being placed over it. To remove

these overlaps, a function was created which removed repeated centroid (+/- 1mm) and radius values (+/- 1mm).

Simple erosion filtering will not be enough to identify the node located within the red box in Figure 24. To identify this, edge detection with information from the Gaussian smoothed image was taken, as explained below in 2.5.5 Edge Detection.

2.5.4. Identification of ideal thresholding

Much of the program's ability to identify nodes resides on the value set to threshold the binary image. In the extreme, if the thresholding value is set to -1000, everything will appear as a '1' and nothing will be identified. Similarly, if the value is set to 1000, everything will appear as a '0'.

Values of binary cutoff between -70 to 20 HU were considered. These values were selected to cover a relatively wide range, since the values of tissue should be above 0 HU and lymph nodes are close to 10-20 HUs. The results of this in Figure 25 indicate that a maximum of nodes are found with a thresholding value of -20. A node was determined to have been detected if 75% of its axial slices or more are located within the radii of the surface. A false surface is any surface identified which does not occur on an axial node slice with the correct centroid (+/- 2mm) and correct radii (+/- 2mm).

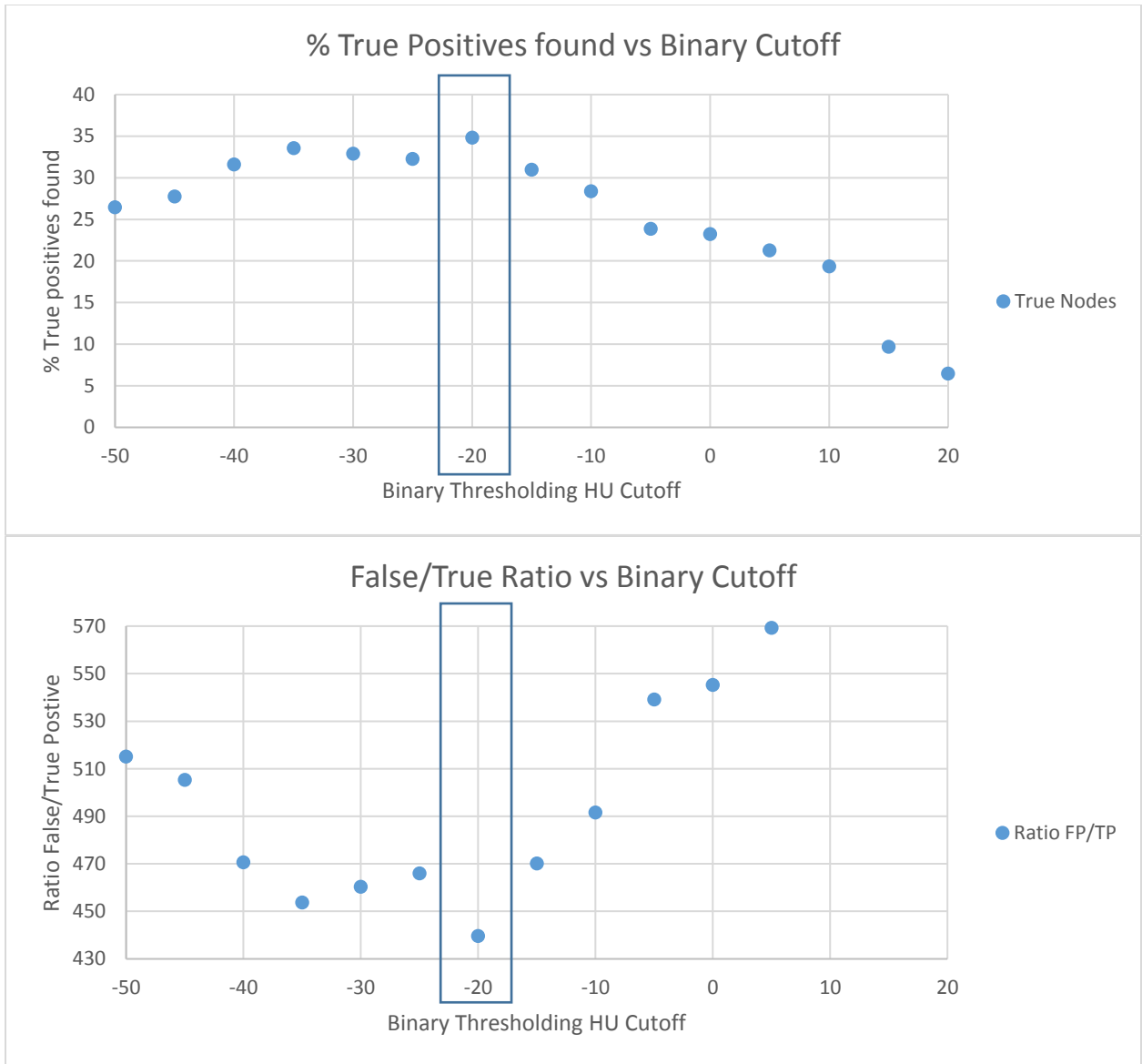


Figure 25: (top) % of true positives and (bottom) ratio of false/true positives vs HU Cutoff

Note that all nodes were not identified, as a single node could go from being an independent structure to pressing against normal tissue, resulting in part, but not all, of the required 75% of it being identified. This is caused by an inability for the erosion filtering to identify a node if there is not an edge around it (Figure 24, red box).

2.5.5. Edge Detection

In order to help separate tissues which have different HUs, but are still overlapping in the binary image, information from the Gaussian filtered image is employed with a LoG edge detection algorithm.

With this algorithm, the value of sigma can be selected by the user. The edges which are detected on the filtered image are then superimposed onto the binary image. Sigma values from 1.00 to 7.75 in 0.25 increments were considered for usage. The smaller values of sigma will help create edges between structures when their values are already very close, but can result in extraneous edges, and the larger sigma values will help separate the tissues which have relatively larger differences in their HUs, Figure 26.

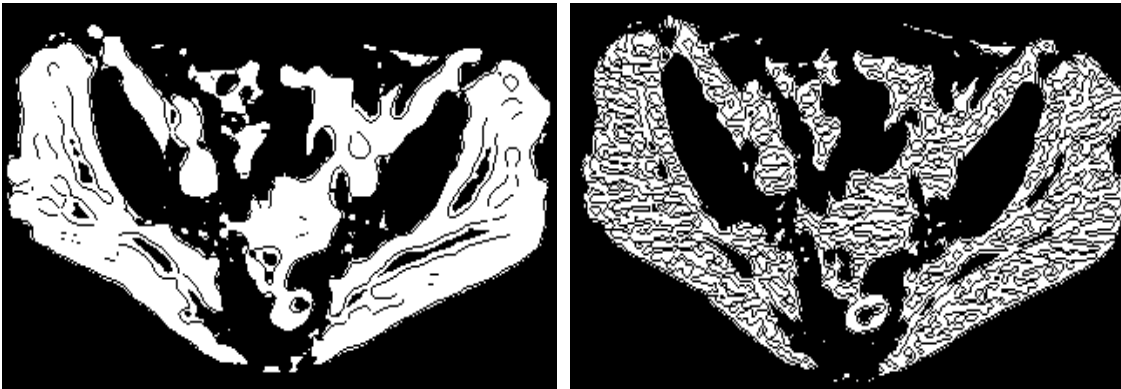


Figure 26: (left) Image with edges imposed from $\sigma = 3$, (right) Image with edges imposed from $\sigma = 1$

With the proper sigma, it is possible to identify the top of the node located within the red box in Figure 27, which will allow erosion filtering to later identify as an independent surface.

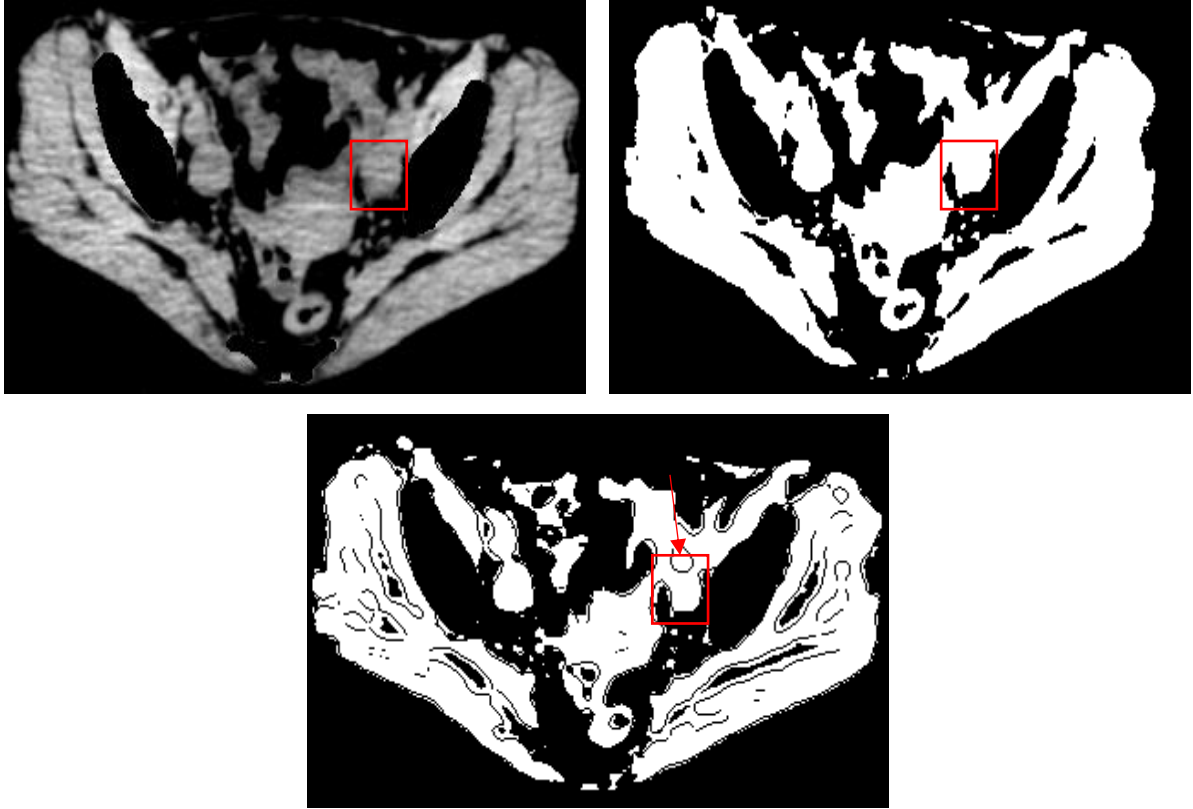


Figure 27: (top left) Original, filtered image, (top right) Image of node collapsed into artery and near-by normal tissues on binary image and (bottom) Image of node with edge from LoG edge detection imposed, $\sigma = 3 \text{ mm}$

Lower sigma values consistently generated larger numbers of false surfaces, Figure 28. Therefore, there was an incentive to find the combination of the largest sigma values which identify the most pathologic nodes. With 25 total possibilities, 24 from sigma 2.00 to 7.75 in 0.25 increments, and 1 for the binary image with no edge detection, there are a total of 2^{25} possible combinations of sigma.

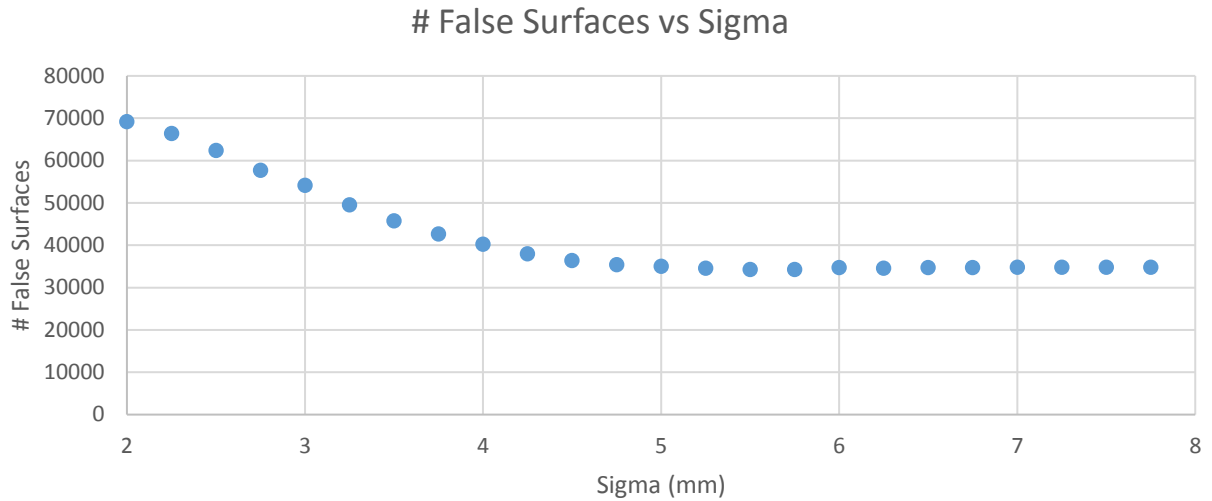


Figure 28: Number of false surfaces generated vs sigma

In order to avoid testing all possible combinations, forward selection (35) was employed to determine the optimal combination of sigma values. This means that the largest sigma was first selected (the binary, as it is essentially a sigma of infinity) and then the next largest sigma was employed and the number of nodes detected was recorded. After which, the second value was removed and instead the 3rd was placed in and repeated. Whatever combination resulted in the largest increase in nodes detected was carried onto the next step, and so on until at least 90% of the nodes had been identified. A hypothetical example of this is shown in Figure 29.

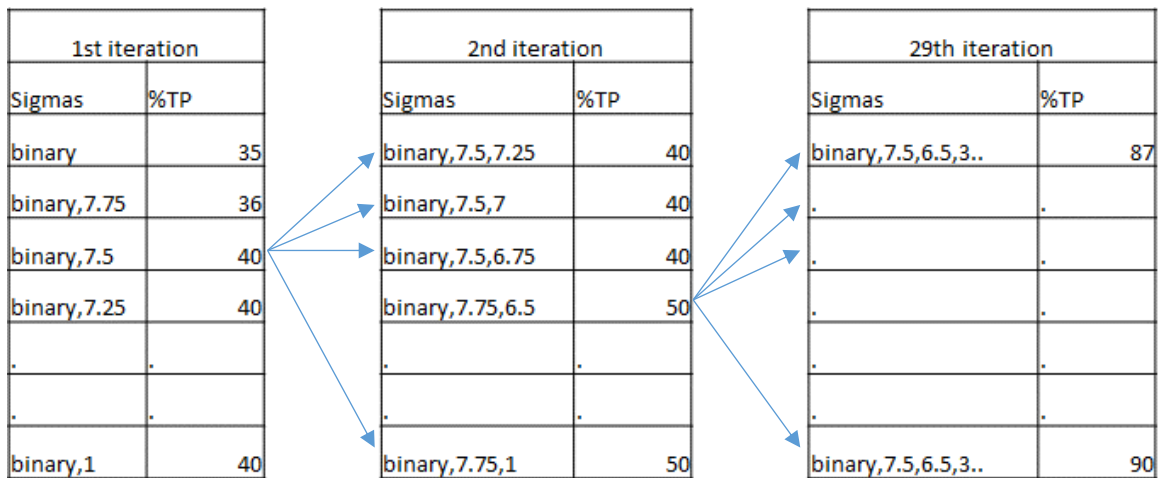


Figure 29: Example of forward selection for sigma

The results of which were that the binary and sigma values of 5 mm and 3.5 mm were selected based on their ability to identify 90 percent of the true positive nodes.

2.6. Correction for non-circular geometry and poor identification

The erosion and edge detection methods thus far shown identified most of the positive pathologic nodes, with the caveat of also identifying a large number of surfaces which are not nodes, “false surfaces”. Recall that a false surface is any surface identified which does not occur on an axial node slice with the correct centroid ($\pm 2\text{mm}$) and correct radii ($\pm 2\text{mm}$). In order to remove some of these erroneous surfaces, criteria were employed based on information from the binary images and the Gaussian smoothed images.

2.6.1. Binary Image Factors

Within the binary images, four metrics were considered to differentiate the false surfaces from true surfaces: solidity, difference in radii, difference in radii*baseradii, and max radii.

2.6.1.1. Binary Image Factors: Solidity

Solidity is an output created by regionprops which gives the proportion of area contained within the convex surface, divided by the total area. A circle and rectangle would have a solidity equal to ~ 1 , while a crescent moon would have a solidity less than 1, Figure 30. An equivalent example is placing a rubber-band around the object and identifying how much is binary ‘1’ within the area of the rubber band.

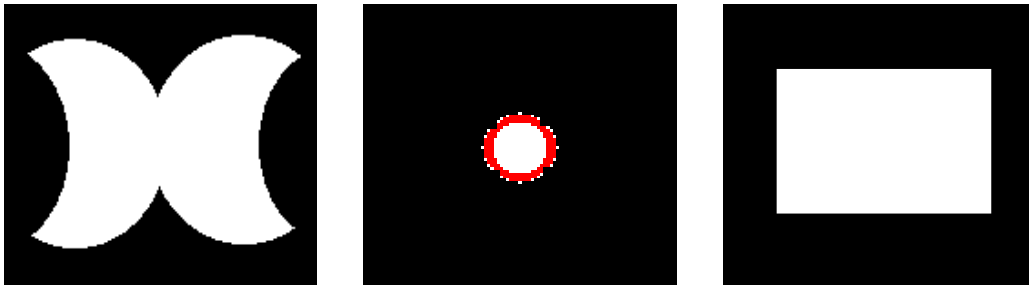


Figure 30: (left) Solidity of connecting circles is .7, (center) solidity of single circle is ~ 1 and (right) solidity of a rectangle is 1

Based on the results, a minimum solidity of 0.85 was selected as a cutoff as it maintained a large percentage of the true positives while allowing a reduction in the ratio of false to true positives, Figure 31.

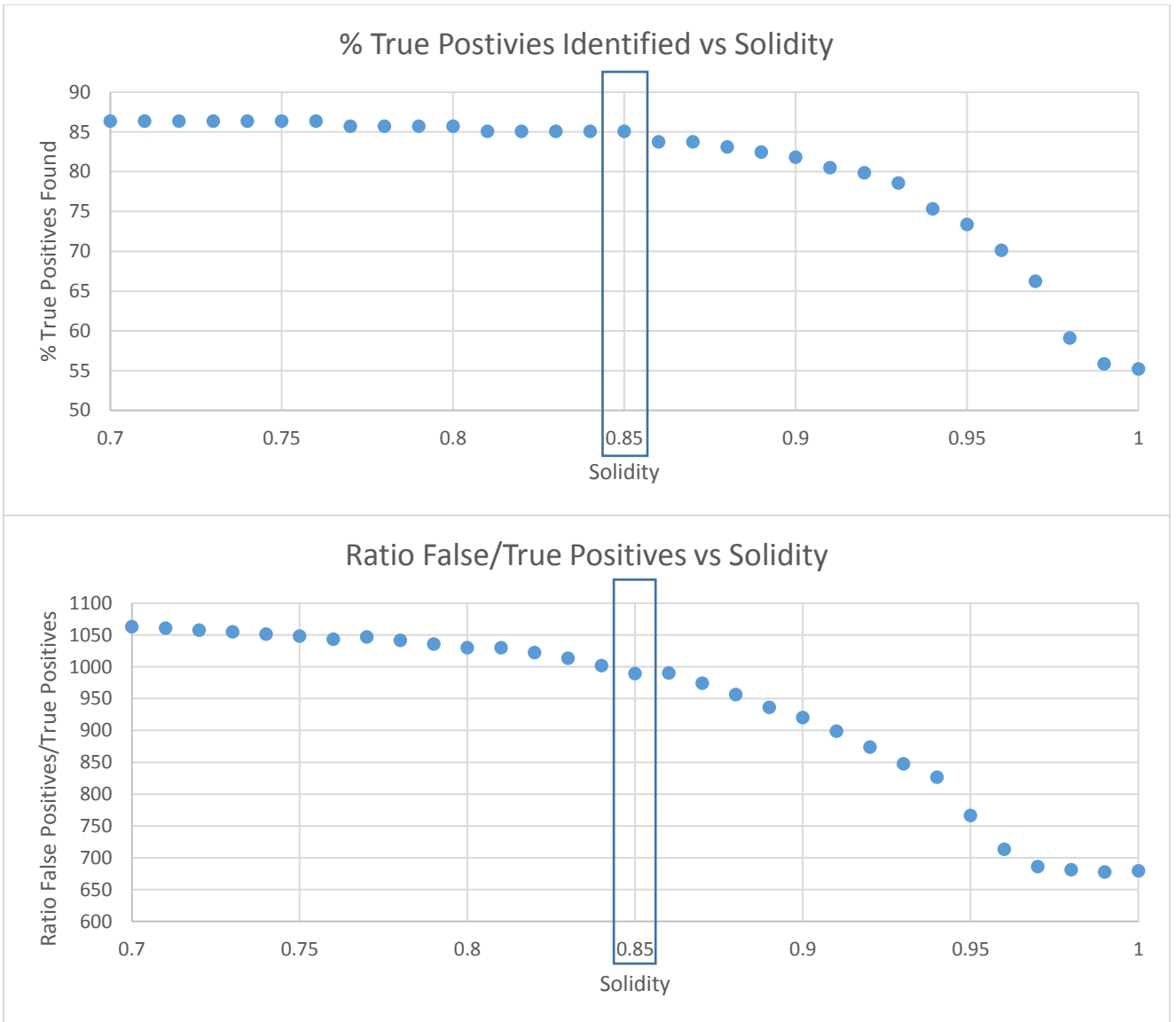


Figure 31: (top) % of true positives found vs solidity and (bottom) ratio of false positives to true positives vs solidity. Cutoff of 0.85 was selected

2.6.1.2. Binary Image Factors: Radius Difference

In order to further reduce the number of potential false surfaces, a criterium was created based on how circular was the identified surface. A circle of equal area (red) was masked onto the binary image for each surface identified, where a circle of equal area was then again measured, Figure 32. A difference in the radii between the two was found; if the surface identified is a circle, the difference will be 0.

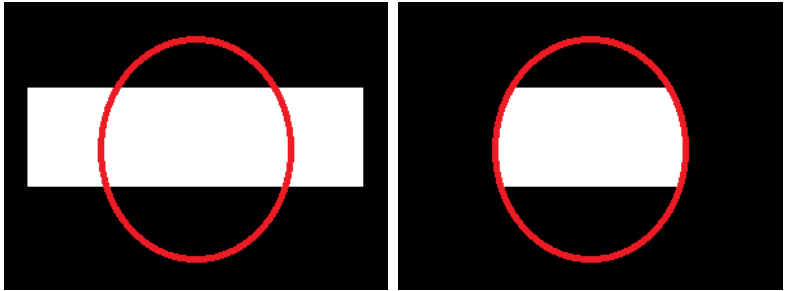


Figure 32: (left) Identification of potential surface and (right) mask of surface

The results, as shown in Figure 33, led to the selection that any surface with a radii difference greater than 3.5 mm was removed, as it maintained most of the true positives while removing some false surfaces.

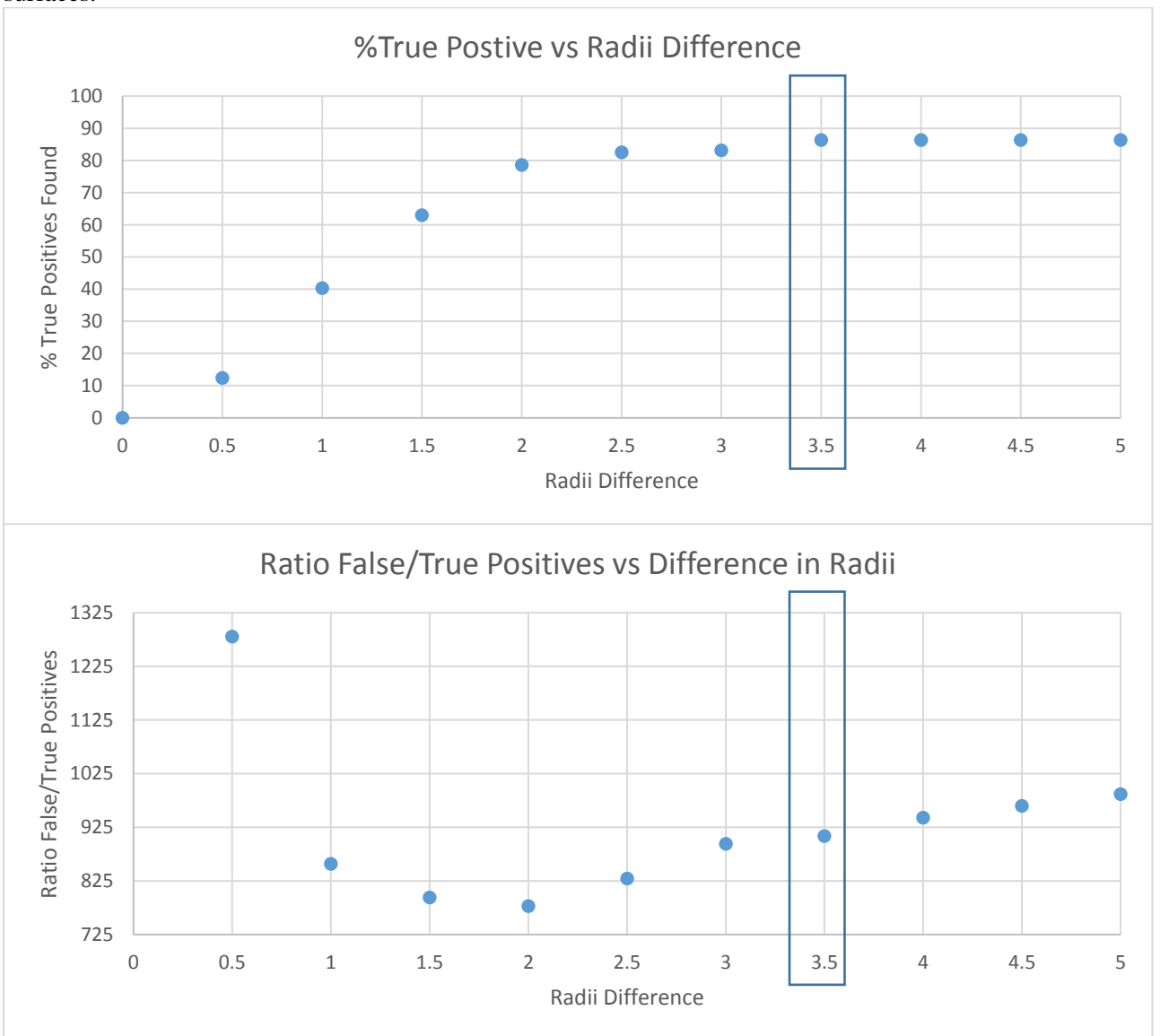


Figure 33: (top) Percent of True positives found vs radii difference Ratio of false/true positives vs difference in radii from projection and (bottom). Cutoff criteria of 3.5mm was selected.

2.6.1.3. Binary Image Factors: Difference in radii*Base radii

This criteria was created as a difference in radii, as explained previously, multiplied by the initial radius. With this, a large surface which is not circular will have a significantly larger value than a smaller structure with the same difference in radii. The results of this can be seen in Figure 34, where a cutoff of 50 was selected as it maintained most of the true positives, while allowing a reduction in false/true positives.

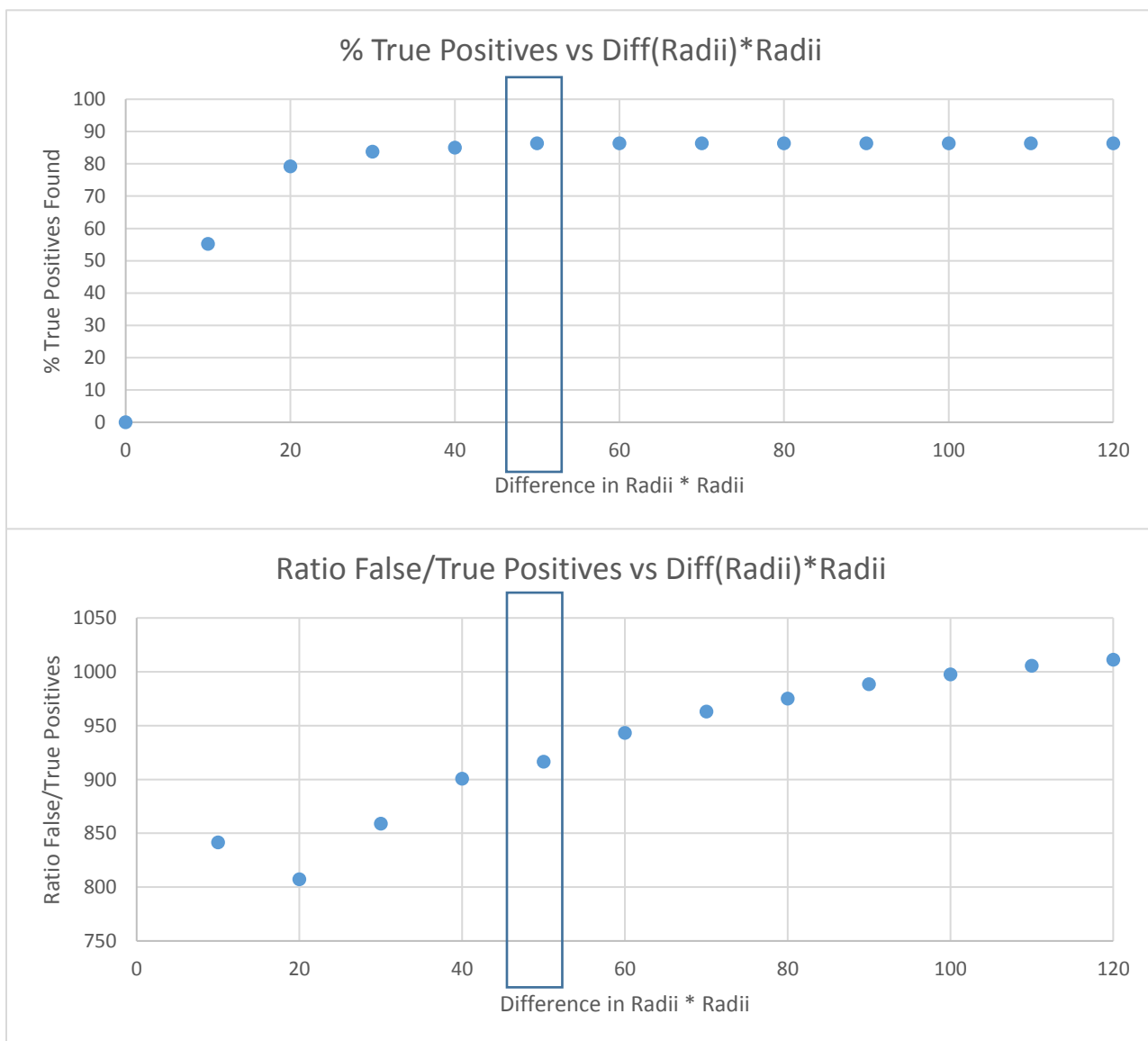


Figure 34: (top) Percent of true positives found vs difference in radii*radii. (bottom) Ratio of false to true positives vs difference in radii * radii Cutoff of anything greater than 50 was selected

2.6.1.4. Binary Image Factors: Max Radii

Certain structures can immediately be removed based solely on their size. A surface identified over the bladder will have a significantly larger radii measured than that of a potential node, and can thus be removed. Based on the data shown in Figure 35, anything with a radius larger than 14 mm can be removed while not removing any potential true positives.

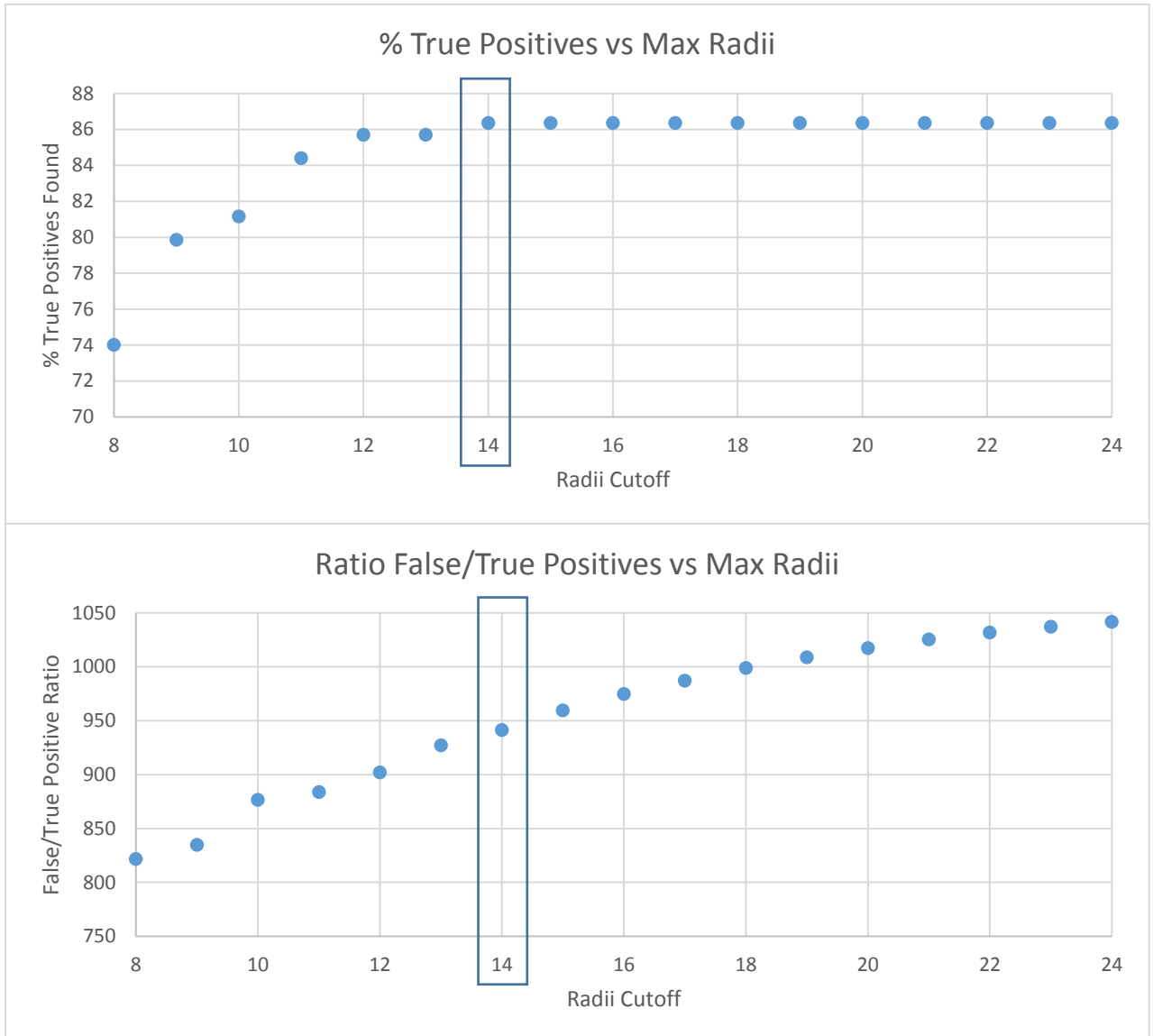


Figure 35: (top) Percentage of true positives (TP) with radii less than cutoff. Radii greater than 14 mm were removed and (bottom) Ratio of false to true positives vs max radii cutoff. A cutoff of 14 mm was selected

2.6.2. Gaussian Smoothed Image Factors

As shown in the previous figures, it is possible for connected binary surfaces to be identified as a single potential node. For each surface the mean pixel values of a circle of equivalent area within it are measured, as well as the mean pixels of a ring placed around the outside, Figure 36. In order to remove surfaces which might have been poorly placed, a base and base-ring criteria were created: (1) that the mean HUs of the base circle should be above a certain threshold and (2) that the difference between the base minus a ring around the base should be above a certain threshold.

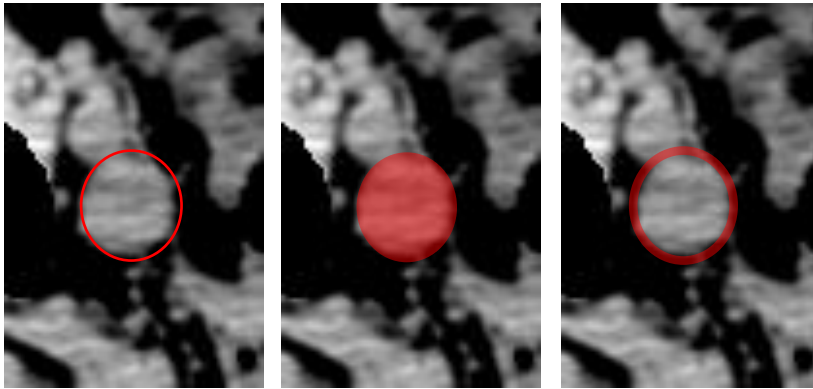


Figure 36: (left) Node was identified from binary image, (center) the mean of the area on the original image, 'base', and (right) the mean of the area on the outside of the circle, 'ring'

Determination of the base and ring area was achieved by filtering a normalized circular matrix with radius equal to that identified from the regionprops function across the image.

2.6.2.1. 'Base' Minimum mean HU

Data from the surfaces, Figure 37, showed that a minimum mean HU base of 10 allowed for a reduction in the ratio of false/true positives while maintaining most of the true positives.

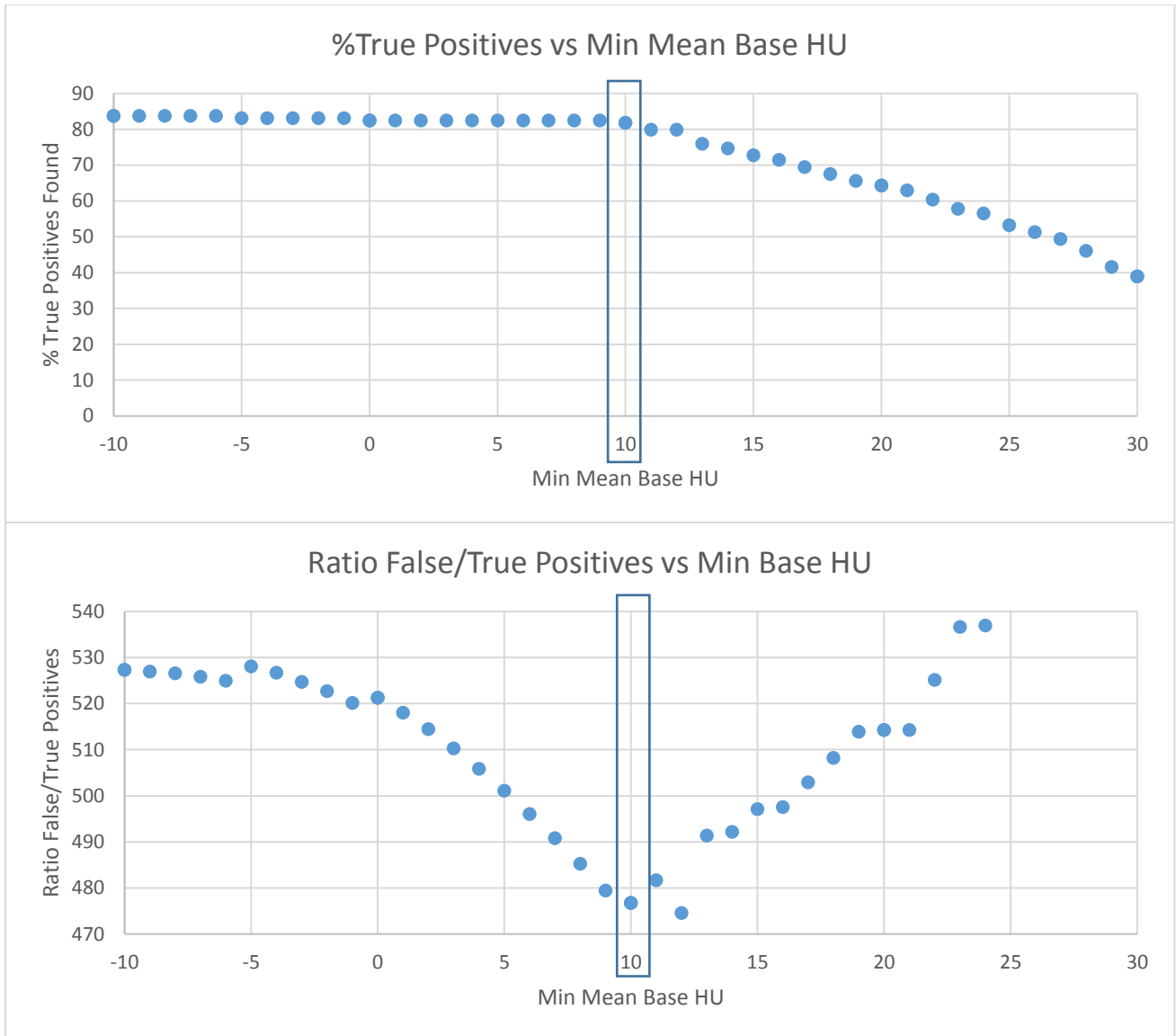


Figure 37: (top) Percentage of true positives found with min mean base cutoff and (bottom) Ratio of false/true positive with mean base cutoff. A minimum value of 10 was selected.

2.6.2.2. 'Base' minus 'Ring' Minimum mean HU

Visual inspection of cervical cancer nodes often demonstrates them to have a region immediately around them which has HUs less than that of normal tissue, Figure 36. In order to remove other potential false surfaces which occur within homogenous tissues, a ring around the outside of the node was imposed and then subtracted from the base. If the surface identified was similar to that shown in Figure 36, the base – ring value will be greater than 0. This ring area was determined as the minimum of a ring, which

was: the radius of the circle, the radius + 1 mm, and the radius + 2 mm. These additions were added to compensate for oblique nodes, which are not perfectly encapsulated by a circular ring, Figure 38.

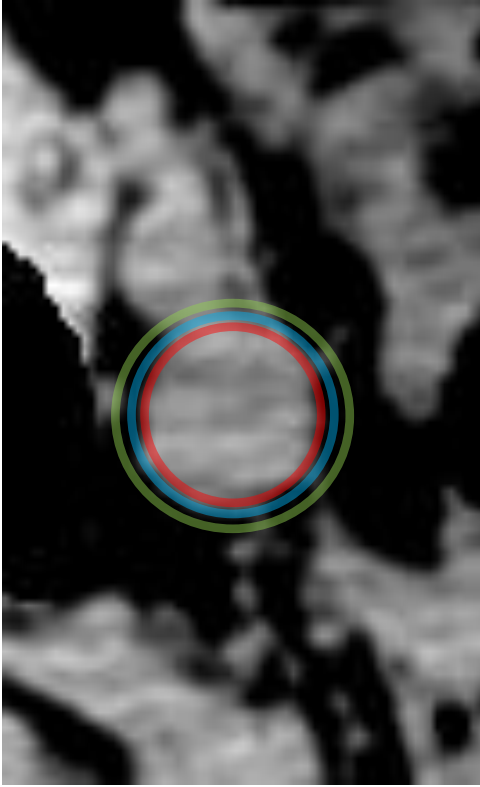


Figure 38: Ring mean value was taken as the minimum of the red, blue, and green ring values.

Since the nodes ought to have values around them which are lower than the base, a comparison of the base mean minus the ring mean was plotted, Figure 39, and a cutoff value 15 of was selected, as it allowed for the detection of most of the true positive surfaces, while reducing the ratio of false to true positives.

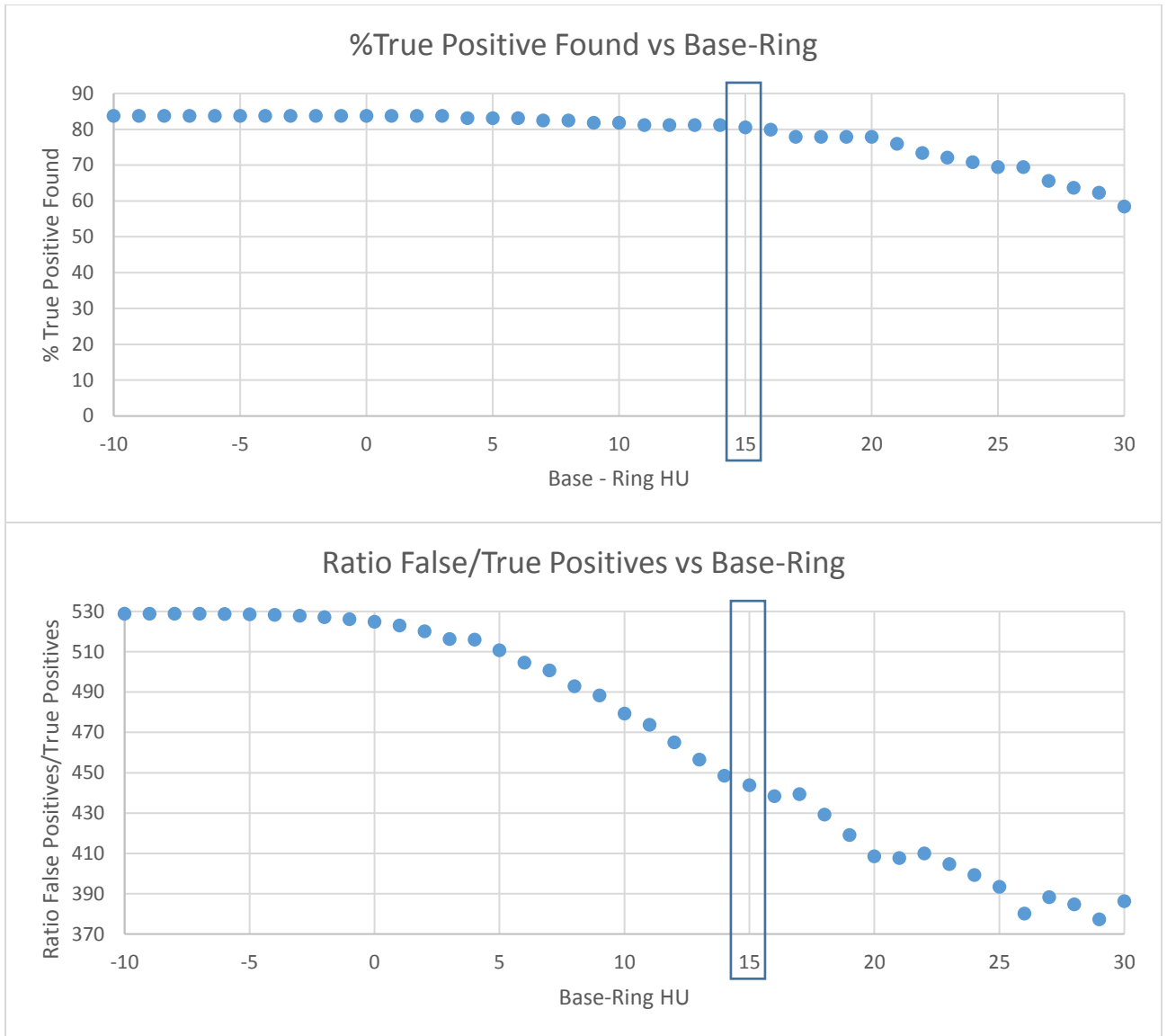


Figure 39: (top) Percentage of true positive found with minimum requirement of Base-Ring (bottom) Ratio of false/true positives vs Base-Ring minimum HU. A minimum requirement of 15 was selected.

2.6.3. Reshaping of Mask

There appeared to be a large number of false surfaces identified in the anatomy inferior to the femoral heads. Observations of positive lymph nodes showed that superior projection of each slice would not directly overlap with bony anatomy. This observation was put to use to remove some of these false surfaces. Projection of each surface, much in the same way that mean values were calculated in 2.6.2 Gaussian Smoothed Image Factors, onto superior slices was performed. If the mean of the projection was greater than 125, it was deemed to have coalesced with bone, and was therefore removed. A graph of the

results in Figure 40 led to the selection of a projection of 100 mm, as it maintained most of the true positives while reducing the false/true positive ratio drastically.

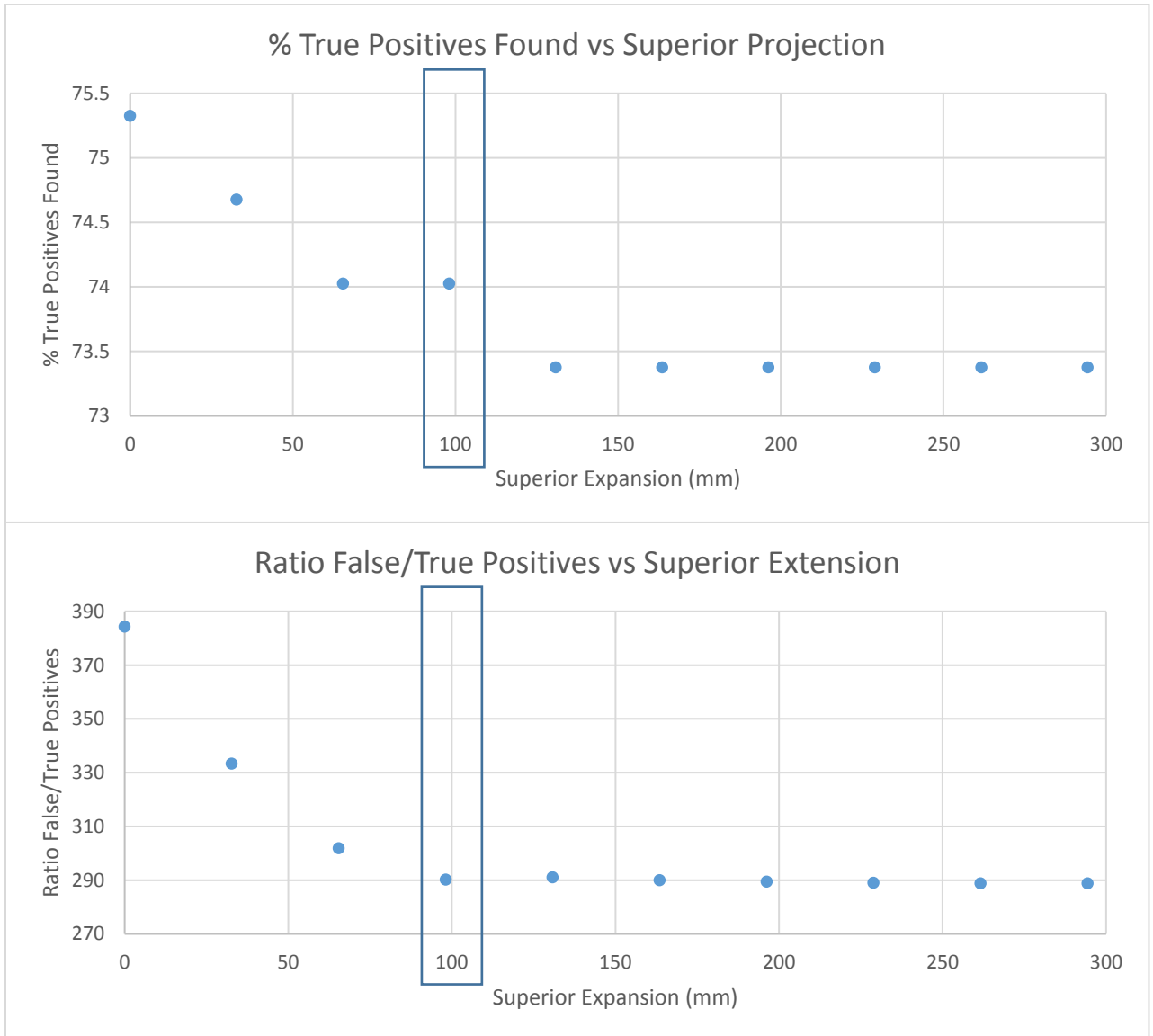


Figure 40: (top) Percentage of true positives found vs superior projection and (bottom) False to true positive ratio vs superior projection. A projection of 100 mm was selected.

The variable of increasing the projected radius by a fixed amount was investigated and the results are shown in Figure 41. An increase in projected area by 1 mm was ultimately selected as it included all the true positives and reduced the ratio of false to true positives.

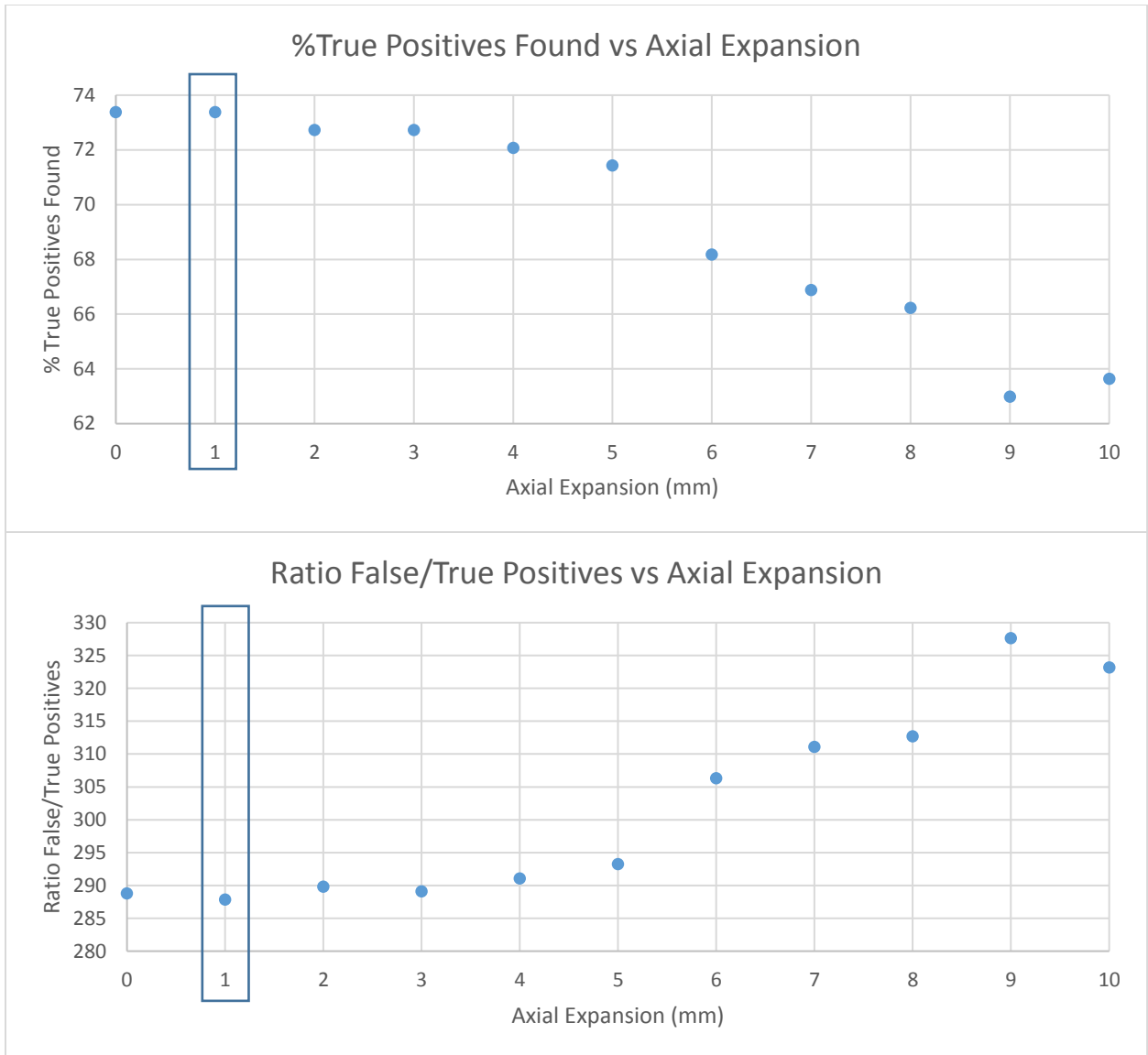


Figure 41: (top) Percentage of true positives found vs axial expansion during superior projection (bottom) Ratio of false/true positives vs axial expansion during superior projection. Axial expansion of 1 mm was selected.

2.6.4. Removal of Overlapping Structures

Even with these criteria, the model often created surfaces which overlapped one another, Figure 42. In order to remove unnecessary surfaces, a criteria was established such that if two surfaces met the following requirements the larger of the two was maintained while the smaller was removed

$$\sqrt{(col_i - col_j)^2 + (row_i - row_j)^2} \leq \max(radius_{i,j}) - \min(radius_{i,j}) + C_0$$



Figure 42: Example of overlapping surfaces

The results of equation 1 are shown in Figure 43, where C_0 was varied from -5 mm to +5 mm.

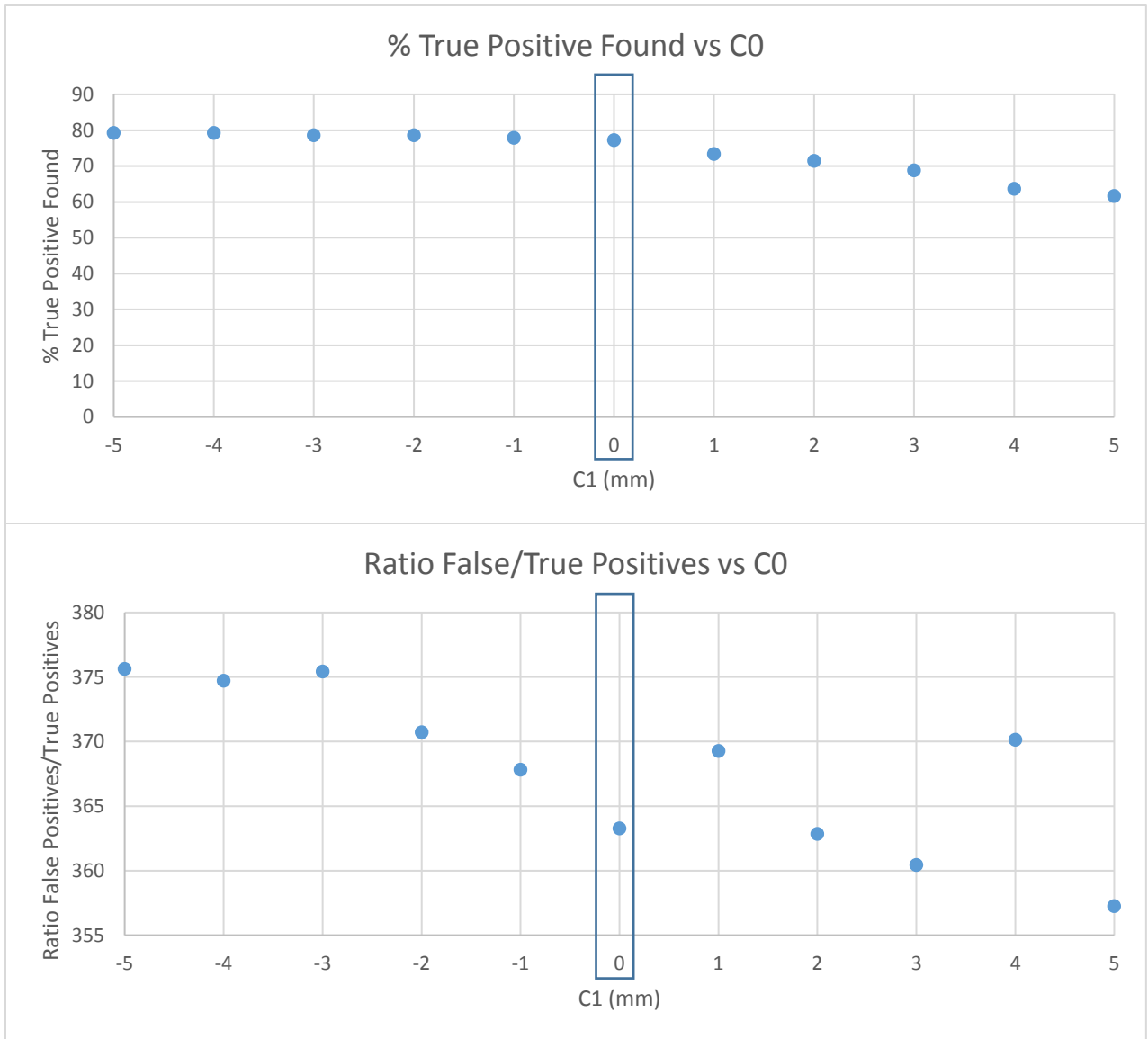


Figure 43: (top) True positive found vs constant for overlap and (bottom) Ratio of false/true positives vs constant for overlap. C_0 of 0 was ultimately selected.

2.7. Identification of start points to build 3D structures

Now that 2D surfaces have been identified on the axial slices, the first step in creating a 3D structure is determining where to start the building process.

Lymph nodes within the cervical region are often characterized by their sudden appearance and disappearance within axial slices (Figure 44).

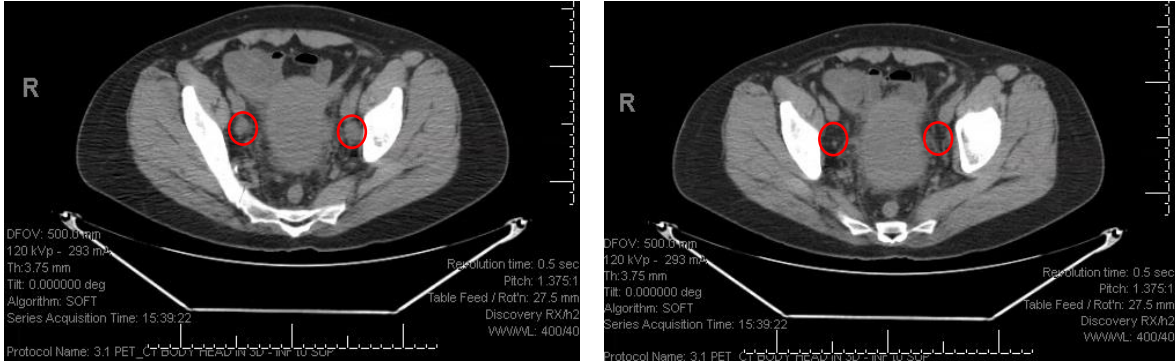


Figure 44: (left) Image of two E1/I1 cervical cancer nodes and (right) 7 mm inferior, both completely gone

In order to identify regions which signal the beginning of pathologic lymph nodes, each previously identified surface is superimposed onto the slices directly inferior to it, Figure 45.

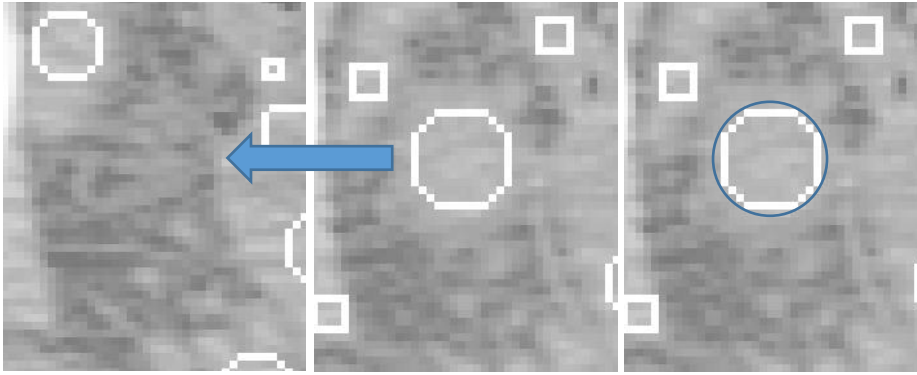


Figure 45: (left and center) Projection of surface onto inferior slice, finding no surfaces. (right) Consideration of surface as a starting point (blue circle).

The criteria for determining if there is another surface located inferiorly is represented by the following equation:

$$\sqrt{(col_i - col_j)^2 + (row_i - row_j)^2} \leq \max(radius_i, radius_j) * C_1 + C_2$$

Where i is the immediate surface, j is all possible surfaces on the inferior slice, and C₁ and C₂ are constants. If there are no surfaces which fall within this projection, the surface was considered to be a start point, Figure 45, right. Constants C₁ and C₂ are varied from 0 to 2.1 by .15 increments and -3mm to +3mm by 1mm increments. These values were selected anecdotally as covering a relatively large range based on the results, Figure 46. The results of this identified C₁ equal to .6 and C₂ equal to -2 mm to be useful in maintaining most of the true positives and reducing the false positives, Figure 46.

% True Positives Identified								
		C2						
		-3	-2	-1	0	1	2	3
C1	0	73.4	73.4	73.4	73.4	73.4	73.4	73.4
	0.15	73.4	73.4	73.4	73.4	73.4	72.7	70.1
	0.3	73.4	73.4	73.4	73.4	71.4	70.1	68.2
	0.45	73.4	73.4	72.7	70.8	70.1	67.5	61.0
	0.6	72.7	72.1	70.1	70.1	67.5	59.1	55.8
	0.75	71.4	70.1	69.5	64.9	59.1	54.5	53.9
	0.9	70.1	68.2	66.2	58.4	55.2	52.6	48.7
	1.05	67.5	66.2	57.1	55.2	51.3	48.1	44.8
	1.2	65.6	61.0	55.2	50.0	46.8	43.5	39.0
	1.35	61.0	53.9	50.0	46.1	43.5	37.7	35.1
	1.5	53.2	49.4	45.5	41.6	35.7	33.8	29.2
	1.65	48.7	42.9	39.6	34.4	33.1	27.9	26.0
	1.8	42.9	37.0	33.8	31.8	27.3	26.0	22.1
	1.95	36.4	32.5	30.5	27.3	25.3	20.8	19.5
2.1	31.2	29.2	27.9	24.7	22.1	18.2	18.2	
Ratio of False Positives to True Positives								
		C2						
		-3	-2	-1	0	1	2	3
C1	0	370	370	370	356	313	259	202
	0.15	370	370	358	311	242	189	157
	0.3	364	340	292	226	181	149	126
	0.45	322	269	218	177	141	120	112
	0.6	258	212	171	135	115	111	101
	0.75	209	165	134	115	107	100	89
	0.9	165	131	109	105	96	87	83
	1.05	131	109	104	92	86	81	76
	1.2	109	96	91	87	81	75	73
	1.35	96	90	84	79	73	73	69
	1.5	90	82	77	74	74	69	69
	1.65	81	79	75	74	67	70	65
	1.8	78	78	73	67	69	63	63
	1.95	76	73	68	66	62	65	61
2.1	73	68	62	61	59	63	55	

Figure 46:(top) Percentage of true positives found as a function of C1 and C2. (bottom) Ratio of false/true positives as a function of C1 and C2.

2.7.1. Removal of extraneous start points

There continued to be an issue that some ‘start points’ were being identified over tissue

equivalent sections, and thus were not good ‘start points’ for the identification of possible pathologic

lymph nodes. Just because one surface was not identified inferiorly to another surface did not mean that it was a proper start point; it could simply be that the surface which was previously inferior had been removed in the previous iterations.

In order to ensure that each start point was a true potential start point, a requirement based on the change in HU units was implemented. The metric created was the difference in respective HUs multiplied by the current surface radius. An example of this is shown in Figure 47 where the mean HU of the superior image is 15 with a radius of 5 mm, the mean HU of the inferior image is 0, and so the metric value will be 75 mm*HU. The metric value mm*HU has no intrinsic meaning.

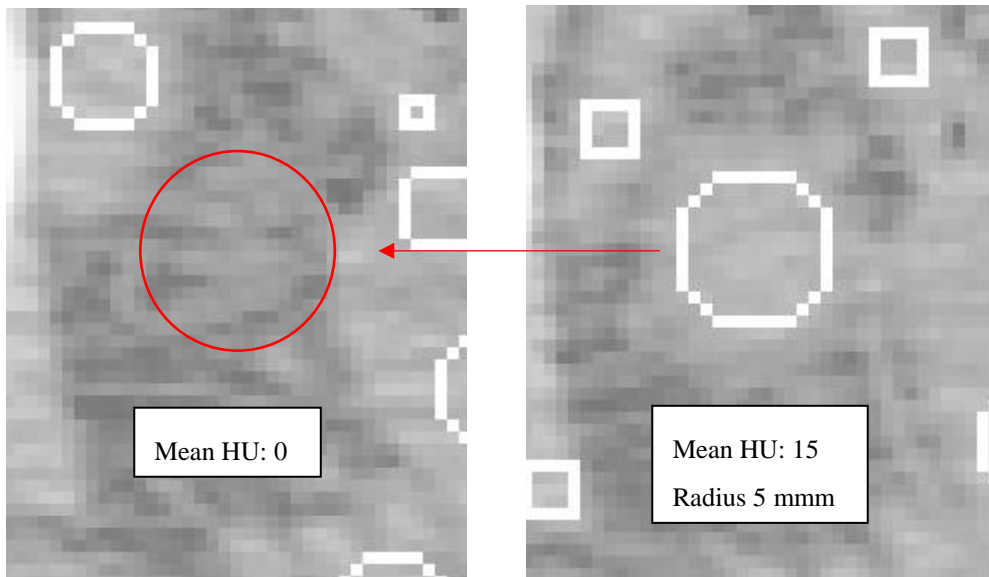


Figure 47: For the above images, the metric value would be equal to $(15-0)*5\text{mm}$, or 75 mm*HU .

The results of this can be seen in Figure 48, where a cutoff of 45 mm*HU was selected based on the observation of number of true positives found and reduction in the ratio of false to true positives.

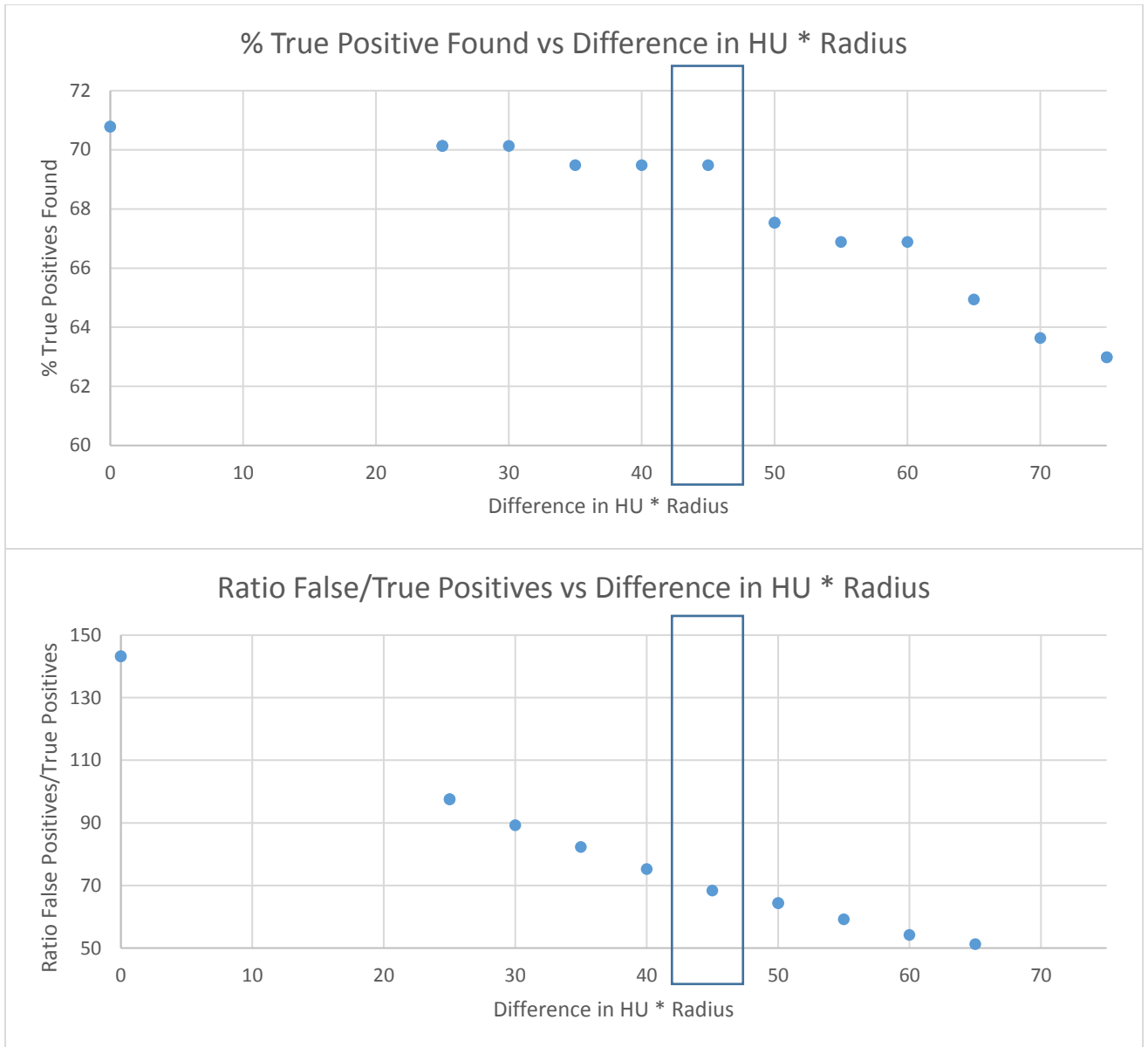


Figure 48: (top) Percentage of true positives found vs difference in HU * Radius (bottom) Ratio of false to true positives vs difference in HU * Radius. A cutoff of 45 mm*HU was selected

2.8. Generation of 3D Structure

After identification of starting surfaces, the remaining axial surfaces are connected to one another to create 3D structures of potential nodes. As in the previous section, these structures are created if the centers of both circles occur within the maximum of their two radii, Figure 49. A surface was considered to continue inferiorly or superiorly if the centers of both circles occur within the maximum of their two radii, represented by the following equation:

$$\sqrt{(col_i - col_j)^2 + (row_i - row_j)^2} \leq \max(radius_i, radius_j) * C_3 + C_4$$

where i is the immediate surface, j is all possible surfaces on the superior slice, and C_3 and C_4 are constants. If there are surfaces which fall within this criteria they are added onto the candidate node.

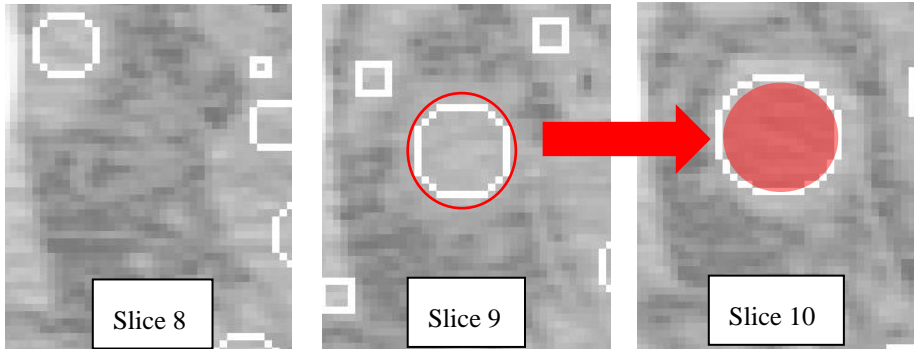


Figure 49: (left-center) Surface in red has been identified as a potential starting point (center-right) this surface is projected onto the superior slice, where another surface is identified, the two are connected.

Based on the data shown in Figure 50, C_3 and C_4 were selected to be .65 and 0 mm, respectively, due to the observation of true positives found and reduction of the ratio of false to true positives.

% True Positives Identified								
		C4						
C3	0	-3	-2	-1	0	1	2	3
	0	0	0	0	1	12	31	53
	0.1	0	0	0	1	25	48	60
	0.2	0	0	2	14	43	57	64
	0.3	0	1	11	39	55	64	67
	0.4	1	8	24	53	62	65	69
	0.5	8	19	47	58	66	67	69
	0.55	16	44	56	64	66	70	77
	0.6	38	54	64	66	71	77	78
	0.65	10	27	58	69	70	70	71
	0.7	22	50	60	71	69	71	79
	0.8	53	60	66	69	75		
	0.9	57	65	72	69	79		

Ratio of False Positives to True Positives								
		C4						
C3	0	-3	-2	-1	0	1	2	3
	0				20	11	14	17
	0.1				11	11	16	22
	0.2			3	6	13	20	37
	0.3		3	5	10	18	34	79
	0.4	4	4	7	15	31	79	171
	0.5	2	7	13	32	71	192	558
	0.55	7	11	31	73	214	580	1500
	0.6	2	7	22	62	160	422	1184
	0.65	6	10	18	30	120	342	961
	0.7	10	18	52	119	358	1030	2400
	0.8	35	78	262	701	1831		
	0.9	99	298	780	1995	4884		

Figure 50: (top) Percentage of true positives found as a function of C3 and C4 (bottom) Ratio of false to true positives as a function of C3 and C4. C3 was selected to .65 and C4 0 mm.

This iteration was continued onwards until there were no additional surfaces superior with which to connect, at which point the surfaces grouped together can be considered as an individual pathologic node candidate. An example of a candidate node is shown in Figure 51.

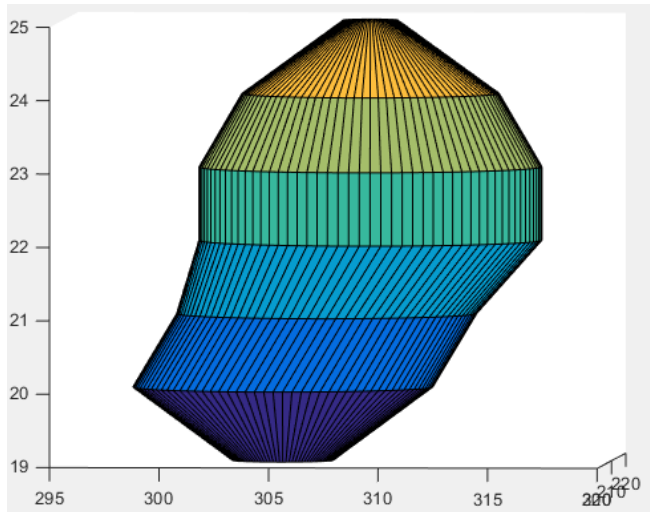


Figure 51: Connection of surfaces from a single lymph node candidate

This methodology creates structures analogous to tree branches: if there are multiple surfaces located directly inferiorly or superiorly to a particularly large surface, each would generate a unique potential node, even if they overlap at the beginning, as shown in Figure 52.

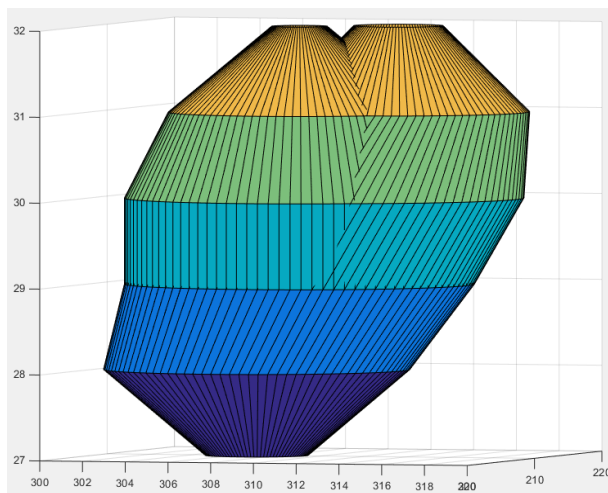


Figure 52: Two node candidates which share the same initializing point

2.9. Additional Extension

The first iteration of this work led to the addition of another segment in the generation of the 3D structure. The ends, or most superior and most inferior surface on the connected candidate node, are projected superiorly and inferiorly by one more slice, respectively. The projection image was transformed into a binary image with a threshold of -20 HU, much like that described in section 2.5- Identification of

Potential Nodes. If the area contained within the binary image was less than that of the original surface area, a new surface was appended onto the end of the structure.

2.10. Results

The results of all the selection criteria for creation of the 3D nodes and removal of extraneous surfaces can be seen in Table 4.

Table 4: All criteria used for the creation of the 3D nodes, as well as criteria for removal of extraneous surfaces. X is the measured variable, removed if equation is satisfied. Example Solidity: remove if x is less than 0.85.

Factor Name	Cutoff Criteria
Binary Image Factors	
Solidity	$x < 0.85$
Radius Difference	$x < 3.5 \text{ mm}$
Radius Difference*Radius	$x < 50 \text{ mm}^2$
Max Radii	$x > 14 \text{ mm}$
Image Factors	
Minimum 'Base'	$x < 10 \text{ HU}$
Minimum 'Base'-'Ring'	$x < 15 \text{ HU}$
Reshaping of Mask	
Superior Projection Distance	100 mm
Axial Expansion	1 mm
Removal of Overlap	
C0	0 mm
Identification of Start Points	
C1	0.6
C2	-2 mm
HU Difference	$x < 45 \text{ HU} * \text{mm}$
Generation of 3D Structure	
C3	0.65
C4	0 mm

With the completion of section 2.8- Generation of 3D Structure, the program identified ~69% (109/154) of the pathologically enlarged lymph nodes on the fifty-eight patients. This resulted in a ratio of false to true positives of 30 to 1.

2.11. Discussion

While the ability to identify 69% of the pathologic nodal tissue was less than the hypothesized 75%, it was determined to be a reasonably acceptable value for identification. The most significant issue was the large number of false to true positives, which was substantially higher than desired. Likely this was caused by the fact that previous attempts to reduce the number of false-positives had been performed with respect to the 2D slices, and not utilizing the candidate node as a 3D structure. A cross-section as might be seen on an axial slice of a candidate node can be very similar in appearance to that of the cross-section of an artery, and thus exacerbates the difficulty of differentiating the two when using a 2D basis alone. The reshaping of the mask (Section 2.6.3- Reshaping of Mask) assumes that the patient is imaged with 0 degrees of angle, and this may cause an issue if large scan angles are used, although this has not been tested.

2.12. Conclusion

In summary, it is possible to identify 69% of the potentially pathologically enlarged lymph nodes based on 2D axial slices in a non-contrast CT. However, the surface differences occurring between normal tissues and pathologically enlarged nodal tissues on individual axial slices are at times not great enough to differentiate the two without a large number of false positives to true positives (30:1). Further efforts to reduce the false positive/true positive ratio are described in Chapter 3: Identification of differentiating features and optimization of model. This effort is based on 3D rather than 2D identification of pathologically enlarged nodal structures, to reduce the false-to-true positive ratio.

3. Chapter 3: Identification of differentiating features and optimization of model

3.1. Introduction

It was theorized that the ratio of pathologically enlarged candidate nodes to normal tissues, as presented in Chapter 2: Identification of Potentially Pathologically Enlarged Lymph Nodes, could be improved with a machine learning model and the introduction of features regarding the 3D candidate nodes. While 2D requirements had been previously created to remove unwanted surfaces, this chapter will focus solely on the 3D structures and creating a model which utilizes features associated with the 3D structures to differentiate pathologically enlarged lymph nodes from normal tissues. For each potential node entered into the trained model, a 'score' is created for the likelihood that a potential node is in fact a pathologically enlarged lymph node. The lower the score, the more confident the model is that the potential node is a pathologically enlarged lymph node.

3.2. Training and Test Generation

Random removal of ten patients from the original fifty-eight was used to generate thirty groups of forty-eight training patients and ten test patients, to provide data for model analysis, as shown in Figure 53.

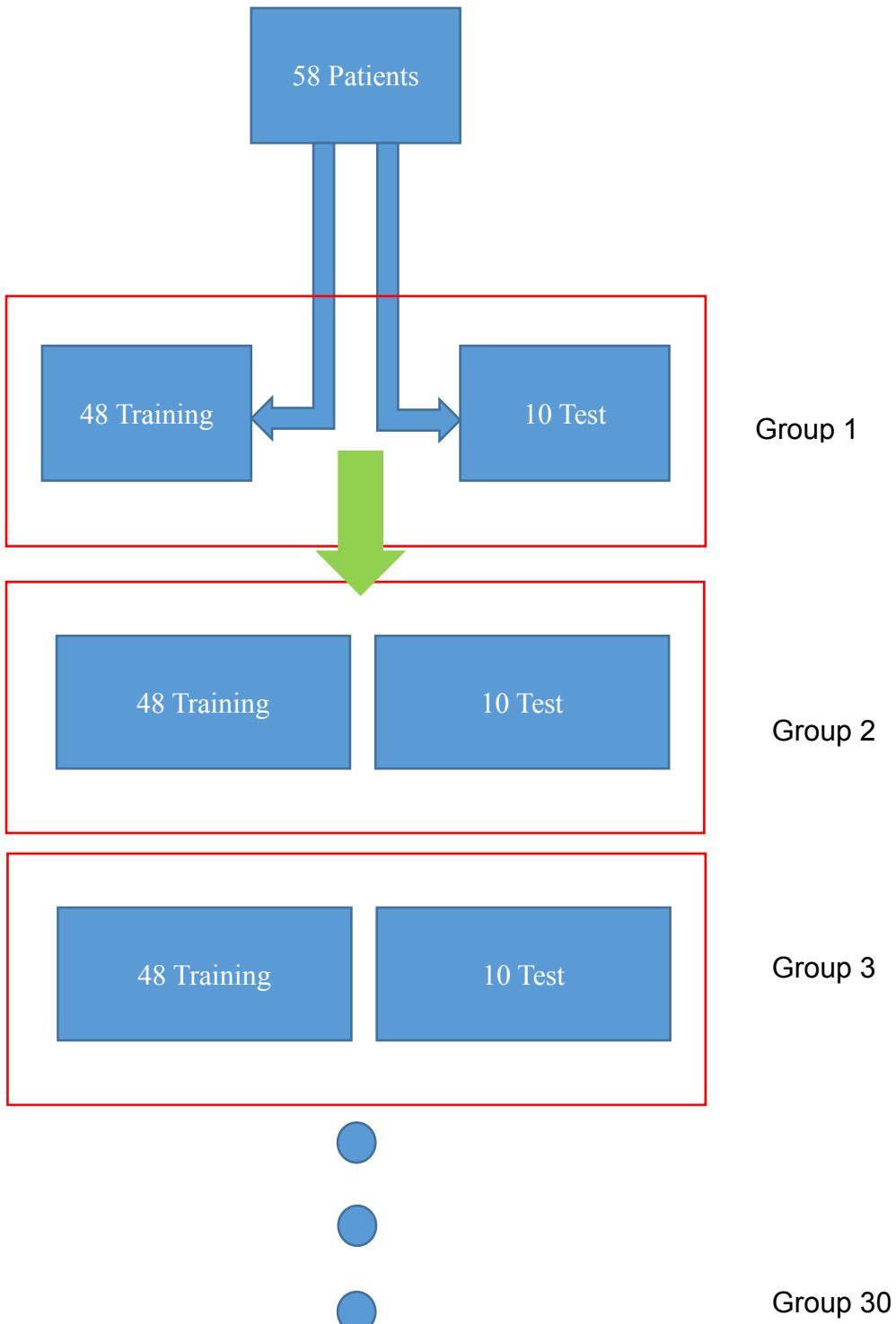


Figure 53: Random selection without replacement of 48 patients for training and 10 patients for test. Repeat random selection to make 30 unique groups

3.3. Feature identification

Proper differentiation of nodes from normal tissues required the generation of features which were consistently different between normal tissue structures and nodal structures. Eighty-six features were created for consideration based on the general physical shape of nodes (20), being banana or spherical in appearance (32), their location within the anatomy (1), their volume (1), and histogram features (64).

3.3.1. Shape Features and Location Feature

The 21 shape features can be divided into 2 major groups: 16 of these regarding the radii between slices which make up the node, 1 for the volume of the node, and 4 concerning the change in center of each node across the axial slices. The location feature is simply the axial location at the middle of the node candidate.

3.3.1.1. Radii Features

An example of the metric used to create the 16 features based on the radii is given below in Figure 54.

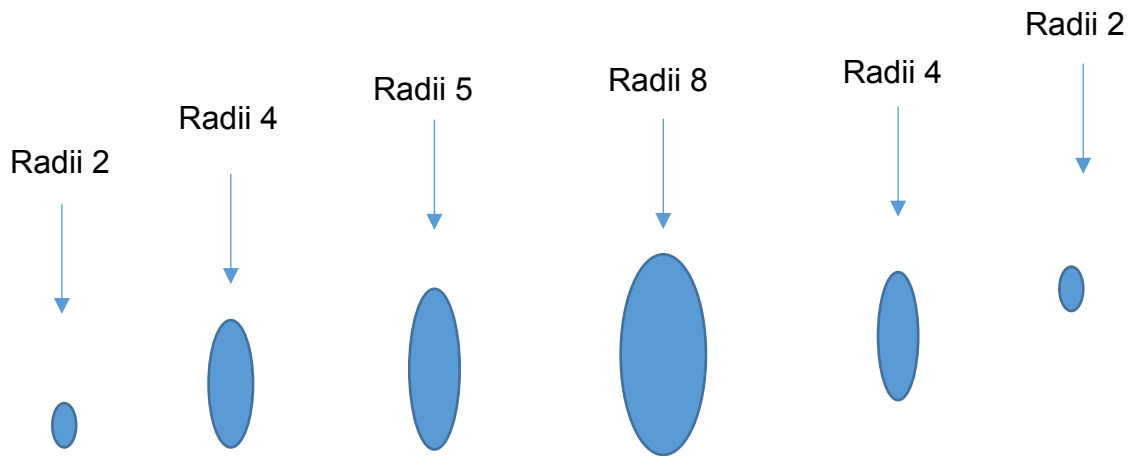


Figure 54: Radii of a candidate node

These features were created to help differentiate normal tissue from pathologic nodes, which normally had a continuous increase in radius to the middle axial slice and then a continuous decrease in radius, until reaching the end of the node. The 16 radii, 1 volume, and 1 location feature can be more easily shown in Table 5. Variable number is used in lieu of feature name in the univariate analysis shown later.

Table 5: Shape Features: Radii. (left column) The variable equation which is used by the model, (center column) the name which it is assigned, and (right column) variable number

Feature Equation	Feature Name	Variable Number
Mean slice	Location	65
max(abs(diff(radii)))	Shape: Max: Diff: Radius	68
max(abs(diff(radii(mid-1:)))	Shape: Max: Diff: Radius	69
max(radii)	Shape: Max: Radius	70
max(radii 1, radii end)	Shape: Max: Radius	71
max(radii (2:end-1))	Shape: Max: Radius	72
max(radii)/AxialExtent	Shape: Max: Radius	73
max(radii 2, radiiend-1)	Shape: Max: Radius	74
min(radii)	Shape: Min: Radius	75
min(radii 1, radii end)	Shape: Min: Radius	76
min(radii 2, radii end-1)	Shape: Min: Radius	77
min(radii (2:end-1))	Shape: Min: Radius	78
std(radii)	Shape: Std: Radius	79
sum(abs(diff(radii)))	Shape: Sum: Diff: Radius	82
sum(abs(diff(radii))/AxialExtent	Shape: Sum: Diff: Radius	83
sum(radii)	Shape: Sum: Radius	84
sum(radii)/AxialExtent	Shape: Sum: Radius	85
volume	Shape: Volume	86

3.3.1.2. Difference in Centers Features

Some normal tissues, such as the external and internal arteries, traveled significantly from their start to their end point. In order to help differentiate these from potential nodes, a metric was created based on the distance of the centroid of each surface to that of the largest surface in the middle of the node, Figure 55.

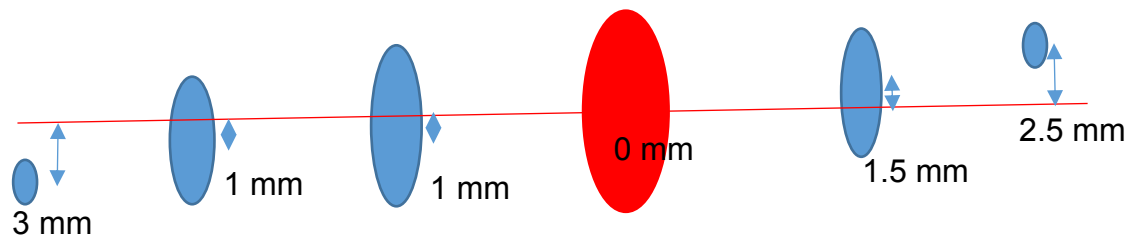


Figure 55: Difference in Distance about centers of surfaces

These 4 features can be more easily shown in Table 6.

Table 6: Shape Features: Distance between slices. (left column) The variable equation which is used by the model, (center column) the name which it is assigned, and (right column) variable number

Feature Equation	Feature Name	Variable Number
$\max(\text{abs}(\text{diff}(\text{difindist}))/\text{radii})$	Shape Features: Max: Diff: Distance Btw Slices	66
$\max(\text{abs}(\text{diff}(\text{difindist})))$	Shape Features: Max: Diff: Distance Btw Slices	67
$\text{sum}(\text{abs}(\text{diff}(\text{difindist}))/\text{AxialExtent})$	Shape: Sum: Diff: Distance Between Slices	80
$\text{sum}(\text{abs}(\text{diff}(\text{difindist})))$	Shape: Sum: Diff: Distance Between Slices	81

3.3.2. Histogram Features

The 64 histogram features can be broken up into two general groups: (56) are in regards to four surfaces imposed onto each potential node: the ‘base’, ‘subbase’, ‘ring’, and ‘subring’, and (8) features are devised from the HU difference of the ‘subbase’ minus the ‘ring’. The base and ring are values which were previously calculated in Gaussian Smoothed Image Factors, Figure 56 a-b. The subbase is the base radius subtracted by 2 mm, and the subring is the ring around this reduced base, Figure 56 c-d.

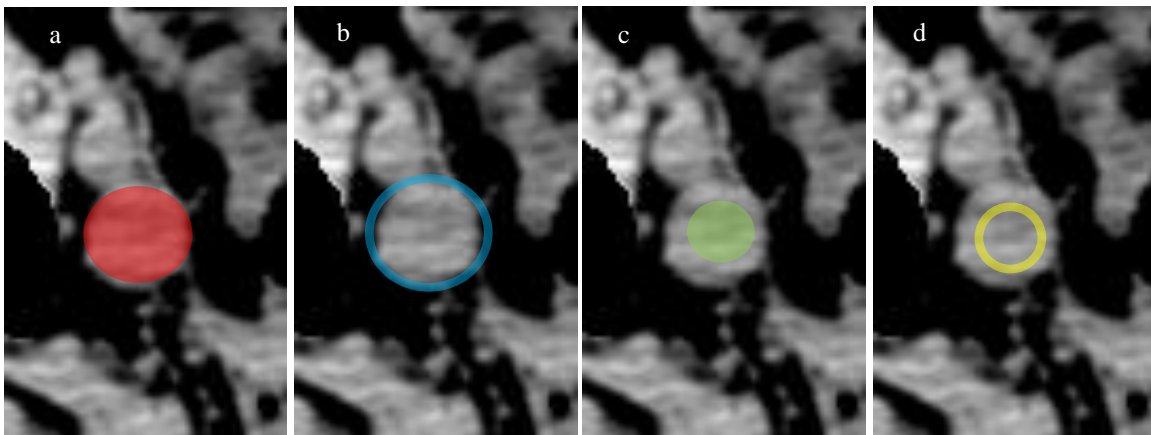


Figure 56: (a) (red) Base area with radius r mm, (b) (blue) Ring area with radius r mm, (c) (green) Subbase area with radius $r-2$ mm and (d) (yellow) Subring area with radius $r-2$ mm.

The first 56 histogram features can further be broken up into 4 groups: 14 for the subbase, 14 for the subring, 14 for the base, and 14 for the ring. The equations and names for the base and subbase shown in Table 7, and those for the ring and subring are shown in Table 8.

Table 7: Base and SubBase (left column) The variable equation which is used by the model, (center column) the name which it is assigned, and (right column) variable number

Feature Equation	Feature Name	Variable Number
$\max(\text{abs}(\text{diff}(\text{node}(:,\text{SubBase}).*\text{radii})))$	Histogram Features: Max: Diff: Mean: SubBase	1
$\max(\text{abs}(\text{diff}(\text{node}(:,\text{Base}).*\text{radii})))$	Histogram Features: Max: Diff: Mean: Base	2
$\max(\text{abs}(\text{diff}(\text{node}(:,\text{SubBase}))))$	Histogram Features: Max: Diff: Mean: SubBase	5
$\max(\text{abs}(\text{diff}(\text{node}(:,\text{Base}))))$	Histogram Features: Max: Diff: Mean: Base	6
$\max((\text{node}(:,\text{Base})))$	Histogram Features: Max: Mean: Base	11
$\max((\text{node}(:,\text{Base}).*\text{radii}))$	Histogram Features: Max: Mean: Base	12
$\max((\text{node}(:,\text{Base}).*\text{radii}.^2))$	Histogram Features: Max: Mean: Base	13
$\max((\text{node}(:,\text{SubBase})))$	Histogram Features: Max: Mean: SubBase	20
$\max((\text{node}(:,\text{SubBase}).*\text{radii}))$	Histogram Features: Max: Mean: SubBase	21
$\max((\text{node}(:,\text{SubBase}).*\text{radii}.^2))$	Histogram Features: Max: Mean: SubBase	22
$\text{mean}((\text{node}(:,\text{Base}).*\text{radii}.^2))$	Histogram Features: Mean: Mean: Base	25
$\text{mean}((\text{node}(:,\text{Base}).*\text{radii}))$	Histogram Features: Mean: Mean: Base	26
$\text{mean}((\text{node}(:,\text{Base})))$	Histogram Features: Mean: Mean: Base	27
$\text{mean}((\text{node}(:,\text{SubBase}).*\text{radii}.^2))$	Histogram Features: Mean: Mean: SubBase	31
$\text{mean}((\text{node}(:,\text{SubBase}).*\text{radii}))$	Histogram Features: Mean: Mean: SubBase	32
$\text{mean}((\text{node}(:,\text{SubBase})))$	Histogram Features: Mean: Mean: SubBase	33
$\min(\text{abs}(\text{diff}(\text{node}(:,\text{Base}))))$	Histogram Features: Min: Diff: Mean: Base	37
$\min(\text{abs}(\text{diff}(\text{node}(:,\text{Base}).*\text{radii})))$	Histogram Features: Min: Diff: Mean: Base	38
$\min(\text{abs}(\text{diff}(\text{node}(:,\text{SubBase}).*\text{radii})))$	Histogram Features: Min: Diff: Mean: SubBase	39
$\min(\text{abs}(\text{diff}(\text{node}(:,\text{SubBase}))))$	Histogram Features: Min: Diff: Mean: SubBase	42
$\min((\text{node}(:,\text{Base}).*\text{radii}.^2))$	Histogram Features: Min: Mean: Base	45
$\min((\text{node}(:,\text{Base}).*\text{radii}))$	Histogram Features: Min: Mean: Base	46
$\min((\text{node}(:,\text{Base})))$	Histogram Features: Min: Mean: Base	47
$\min((\text{node}(:,\text{SubBase}).*\text{radii}.^2))$	Histogram Features: Min: Mean: SubBase	51
$\min((\text{node}(:,\text{SubBase}).*\text{radii}))$	Histogram Features: Min: Mean: SubBase	52
$\min((\text{node}(:,\text{SubBase})))$	Histogram Features: Min: Mean: SubBase	53
$\text{std}(\text{node}(:,\text{Base}))$	Histogram Features: Std: Base	59
$\text{std}(\text{node}(:,\text{SubBase}))$	Histogram Features: Std: SubBase	63

Table 8: Ring and Subring (left column) The variable equation which is used by the model, (center column) the name which it is assigned, and (right column) variable number

Feature Equation	Feature Name	Variable Number
$\max(\text{abs}(\text{diff}(\text{node}(:,\text{Ring}))))$	Histogram Features: Max: Diff: Mean: Ring	3
$\max(\text{abs}(\text{diff}(\text{node}(:,\text{Ring}).*\text{radii})))$	Histogram Features: Max: Diff: Mean: Ring	4
$\max(\text{abs}(\text{diff}(\text{node}(:,\text{SubRing}))))$	Histogram Features: Max: Diff: Mean: SubRing	7
$\max(\text{abs}(\text{diff}(\text{node}(:,\text{SubRing}).*\text{radii})))$	Histogram Features: Max: Diff: Mean: SubRing	8
$\max((\text{node}(:,\text{SubRing})))$	Histogram Features: Max: Mean: SubRing	14
$\max((\text{node}(:,\text{SubRing}).*\text{radii}))$	Histogram Features: Max: Mean: SubRing	15
$\max((\text{node}(:,\text{SubRing}).*\text{radii}.^2))$	Histogram Features: Max: Mean: SubRing	16
$\max((\text{node}(:,\text{Ring})))$	Histogram Features: Max: Mean: Ring	17
$\max((\text{node}(:,\text{Ring}).*\text{radii}))$	Histogram Features: Max: Mean: Ring	18
$\max((\text{node}(:,\text{Ring}).*\text{radii}.^2))$	Histogram Features: Max: Mean: Ring	19
$\text{mean}((\text{node}(:,\text{Ring}).*\text{radii}.^2))$	Histogram Features: Mean: Mean: Ring	28
$\text{mean}((\text{node}(:,\text{Ring}).*\text{radii}))$	Histogram Features: Mean: Mean: Ring	29
$\text{mean}((\text{node}(:,\text{Ring})))$	Histogram Features: Mean: Mean: Ring	30
$\text{mean}((\text{node}(:,\text{SubRing}).*\text{radii}.^2))$	Histogram Features: Mean: Mean: SubRing	34
$\text{mean}((\text{node}(:,\text{SubRing}).*\text{radii}))$	Histogram Features: Mean: Mean: SubRing	35
$\text{mean}((\text{node}(:,\text{SubRing})))$	Histogram Features: Mean: Mean: SubRing	36
$\min(\text{abs}(\text{diff}(\text{node}(:,\text{Ring}))))$	Histogram Features: Min: Diff: Mean: Ring	40
$\min(\text{abs}(\text{diff}(\text{node}(:,\text{Ring}).*\text{radii})))$	Histogram Features: Min: Diff: Mean: Ring	41
$\min(\text{abs}(\text{diff}(\text{node}(:,\text{SubRing}))))$	Histogram Features: Min: Diff: Mean: SubRing	43
$\min(\text{abs}(\text{diff}(\text{node}(:,\text{SubRing}).*\text{radii})))$	Histogram Features: Min: Diff: Mean: SubRing	44
$\min((\text{node}(:,\text{Ring}).*\text{radii}.^2))$	Histogram Features: Min: Mean: Ring	48
$\min((\text{node}(:,\text{Ring}).*\text{radii}))$	Histogram Features: Min: Mean: Ring	49
$\min((\text{node}(:,\text{Ring})))$	Histogram Features: Min: Mean: Ring	50
$\min((\text{node}(:,\text{SubRing}).*\text{radii}.^2))$	Histogram Features: Min: Mean: SubRing	54
$\min((\text{node}(:,\text{SubRing}).*\text{radii}))$	Histogram Features: Min: Mean: SubRing	55
$\min((\text{node}(:,\text{SubRing})))$	Histogram Features: Min: Mean: SubRing	56
$\text{std}(\text{node}(:,\text{Ring}))$	Histogram Features: Std: Ring	62
$\text{std}(\text{node}(:,\text{SubRing}))$	Histogram Features: Std: SubRing	64

The final 8 histogram metrics are related to the subbase minus the ring. Recalling back to 2.6.2 Gaussian Smoothed Image Factors, a metric was created which consisted of the base minus the ring. Considering that the subbase ought to be more entirely enclosed within potential nodal tissue, these 8 metrics were created to help separate out nodes which were ideally situated without surrounding normal tissue, Table 9.

Table 9: Subbase - Ring. (left column) The variable equation which is used by the model, (center column) the name which it is assigned, and (right column) variable number

Feature Equation	Feature Name	Variable Number
max(subbase-ring)	Histogram Features: Max: Diff: Subbase-Ring	9
max(subbase-ring).*radii	Histogram Features: Max: Diff: Subbase-Ring	10
mean(subbase-ring)	Histogram Features: Mean: Diff: Subbase-Ring	23
mean(subbase-ring).*radii	Histogram Features: Mean: Diff: Subbase-Ring	24
min(subbase-ring)	Histogram Features: Min:Diff: Subbase-Ring	57
min(subbase-ring).*radii	Histogram Features: Min:Diff: Subbase-Ring	58
std(subbase-ring)	Histogram Features: Std: Diff: Subbase-Ring	60
std(subbase-ring).*radii	Histogram Features: Std: Diff: Subbase-Ring	61

3.4. Feature Selection

3.4.1. Model Selection

Four separate binary classification ensemble models (36) were investigated: AdaBoost (37), RUSBoost (38), RobustBoost (39), and GentleBoost (37).

These potential models were selected based on recommendations from Matlab and literature with regards to their abilities with binary classification. The AdaBoost model is a recommended starting ensemble method. RUSBoost is best utilized for skewed data, where the ratio of false to true positives is greater than 1. RobustBoost is best utilized for label noise, or accidentally mislabeling a true positive or normal tissue. Lastly, GentleBoost works best when there are more than 31 levels of predictors.

3.4.2. Univariate Analysis

Univariate analysis was performed on each variable with each of the four models listed above. The metric used in this analysis was the AUC generated based on the forty-eight training patients and ten test patients as explained in Training and Test Generation. This was repeated independently on the 30 groups to create an average AUC and standard deviation for each feature, using each model, as shown in Figure 57.

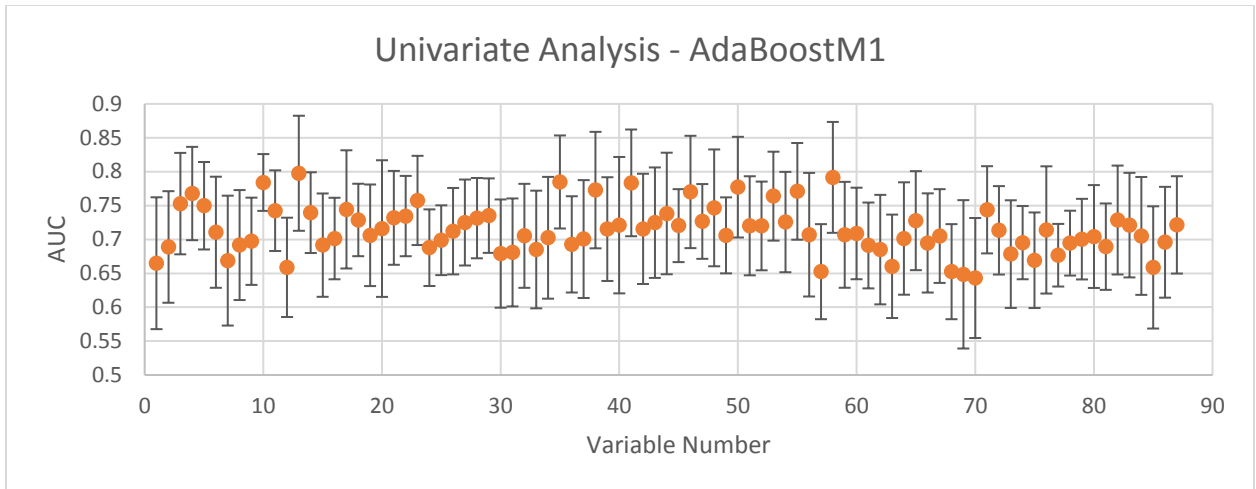


Figure 57: Univariate Analysis - AdaBoostM1, AUC for each variable

3.4.3. Correlation Test

A Spearman correlation test was performed on all variables, as shown in Figure 58. A Spearman test was performed instead of a Pearson test to account for the potential of the variables being related in a non-linear fashion.

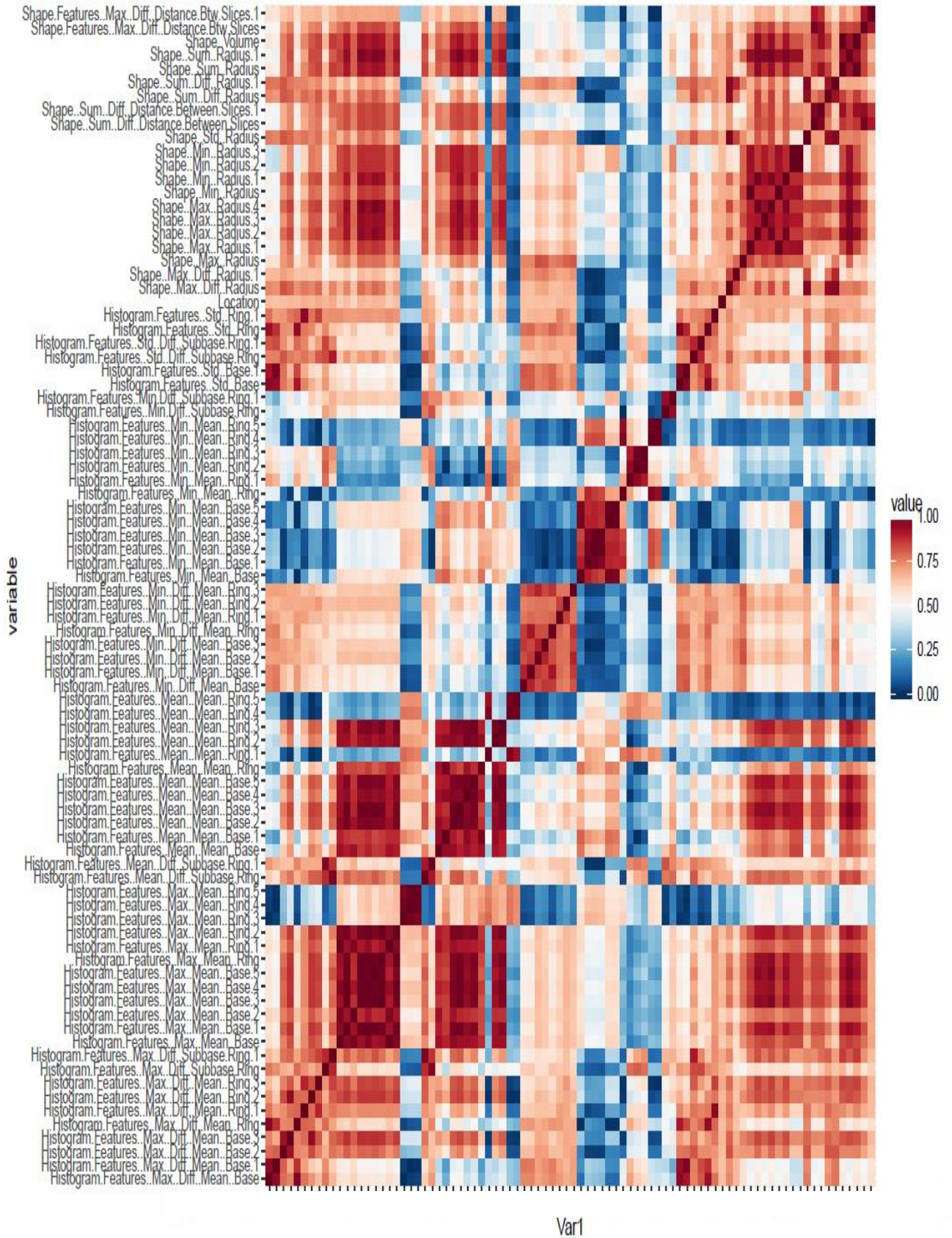


Figure 58: Spearman Correlation Test, x-axis is the same as y-axis

3.4.4. Multi-Variate Analysis

Four methods of feature selection for model building were examined: Serial addition, Forward Selection (35), Backward Selection (35), and Forward/Backward Selection (35).

3.4.4.1. *Serial Addition*

The theory behind Serial addition is to sort all features based on their univariate AUC scores. That being, the feature which had the best ability to differentiate true nodes from normal surfaces would be added first and the worst feature would be added last.

Taking these sorted features, the model is built by adding in the first feature with the highest univariate AUC, and then adding in the variable with the second highest univariate AUC, etc. Note, however, that there are some problems associated with this. For example, if two variables have high AUCs, but are also highly correlated, adding them into the model will not greatly improve it.

To help remove this problem, correlation cutoffs of 1, 0.9, 0.8, 0.7, 0.6, and 0.5 were used to make 6 groups of features. This means, for the 0.5 group, if two features have a correlation coefficient greater than 0.5, the one with the higher Univariate AUC will be selected and the other removed.

3.4.4.2. *Forward Selection*

Forward selection removes the need for making correlation cutoffs. This method involves creating a model with features with the highest univariate AUC. Next, a second feature is input into the model and a comparison AUC is calculated. This second feature is then removed and a different feature is input with a comparison AUC calculated (Figure 59).

1st iteration		2nd iteration		n Iteration	
Variable	AUC	Variable	AUC	Variable	AUC
1	0.758	1,3,2	0.76	1,3,6,...,2	0.86
1,2	0.76	1,3,4	0.75	1,3,6,...,4	0.85
1,3	0.77	1,3,5	0.78	1,3,6,...,5	0.87
1,4	0.74	1,3,6	0.79	1,3,6,...,7	0.8
1,5	0.73	1,3,7	0.71	1,3,6,...,8	0.84
.
.
.
1,n	0.74	1,3,n	0.75	1,3,6,...,n	0.9

Figure 59: Example of Forward Selection. Note the highest AUC on the first iteration is variable 1 and 3. These two are then saved into the 2nd iteration, etc.

The results of this are that an individual test group will have an optimized set of features which best differentiate the positive nodes from the normal tissues.

There is a new issue created with this technique however: each of the 30 groups will generate a different set of ideal features to be used. Figure 60 show that for RUSBoost in Group1, there is a set of 8 features which are best able to create a model. Therefore, to get a metric on how useful these 8 features are on the entire test population, the other 29 groups of forty-eight training and ten test sets are run with only these 8 features. This is repeated again with the optimized set of features determined in each of the 30 groups, for all 4 models.

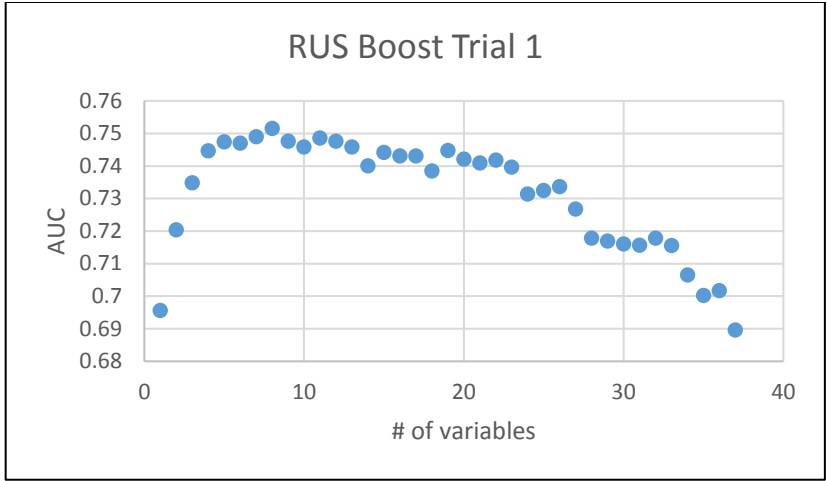


Figure 60: Number of features included for optimized differentiation of true positives and normal tissues on Group 1

3.4.4.3. Backward Selection

Backward Selection works in much the same way as Forward Selection, but in the opposite direction. Whereas Forward Selection begins by essentially doing univariate analysis and adding on variables as they increase the performance in regards to AUC, Backward selection starts with all of the variables included, and then removes variables as they increase the overall AUC.

An example of this can be seen as follows, Figure 61:

1st iteration		2nd iteration		3rd Iteration	
Variables	AUC	Variables	AUC	Variables	AUC
1,2,3,4,5,6,7	0.75	1,2,3,4,6,7	0.82	1,2,3,4,6	0.86
1,2,3,4,5,7,8	0.78	1,2,3,4,6,8	0.85	1,2,3,4,8	0.85
1,2,3,4,5,7,8	0.77	1,2,3,4,7,8	0.75	1,2,3,6,8	0.87
1,2,3,4,6,7,8	0.8	1,2,3,6,7,8	0.79	1,2,4,6,8	0.8
1,2,3,5,6,7,8	0.72	1,2,4,6,7,8	0.7	1,3,4,6,8	0.84
1,2,4,5,6,7,8	0.62	1,3,4,6,7,8	0.65	2,3,4,6,8	0.82
1,3,4,5,6,7,8	0.68	2,3,4,6,7,8	0.69		
2,3,4,5,6,7,8	0.72				

Figure 61: Example of Backward Selection. Each iteration removes the variable which results in the largest increase in AUC.

3.4.4.4. Forward/Backward Selection

Forward selection and Backward selection both have another drawback: while Feature 1 might have the highest univariate AUC, Features 2 and 3 may have a higher combined AUC than Feature 1. This possible combination of features will never occur with the forward selection method and there are other combinations which are not possible from backward selection alone. To try and mitigate this problem, the Forward/Backward Selection technique was investigated.

Much like Forward Selection, this method employs sequentially adding variables to see which gives the largest increase in AUC, Figure 59. However, between each step a second Backward selection is run, and if the AUC increases, it is removed permanently. The example in Figure 62 demonstrates what would happen on the 5th potential iteration.

Start Point		1st Iteration		2nd Iteration		3rd Iteration		Final Selection	
Variables	AUC	Variables	AUC	Variables	AUC	Variables	AUC	Variables	AUC
1,3,6,8,12	0.85	1,3,6,8	0.84	1,3,8	0.82	3,8	0.87	3,8,12	0.9
		1,3,6,12	0.825	1,3,12	0.87	3,12	0.8		
		1,3,8,12	0.875	1,8,12	0.8	8,12	0.75		
		1,6,8,12	0.85	3,8,12	0.9				
		3,6,8,12	0.85						

Figure 62: Example of Forward/Backward selection. The 'StartPoint' comes from the previous forward selection and each iteration within the backward selection is a removal of one variable, trying to maximize the AUC

After each iteration of Backward selection, the final result is then re-entered back for the next iteration of Forward selection. Similar to Forward Selection, the optimized features selected from each trial were then exclusively used in the other trials to get an average AUC and standard deviation.

3.5. Results

An example of the results of Serial Addition for GentleBoost can be seen in Figure 63. Note that the lower the correlation cutoff, the fewer variables are present, which makes intuitive sense as it removes variables which are correlated. Here, it's possible to see that the GentleBoost model has the best ability to differentiate true positive nodes from normal structures when 15 features are used with a correlation cutoff of 0.9.

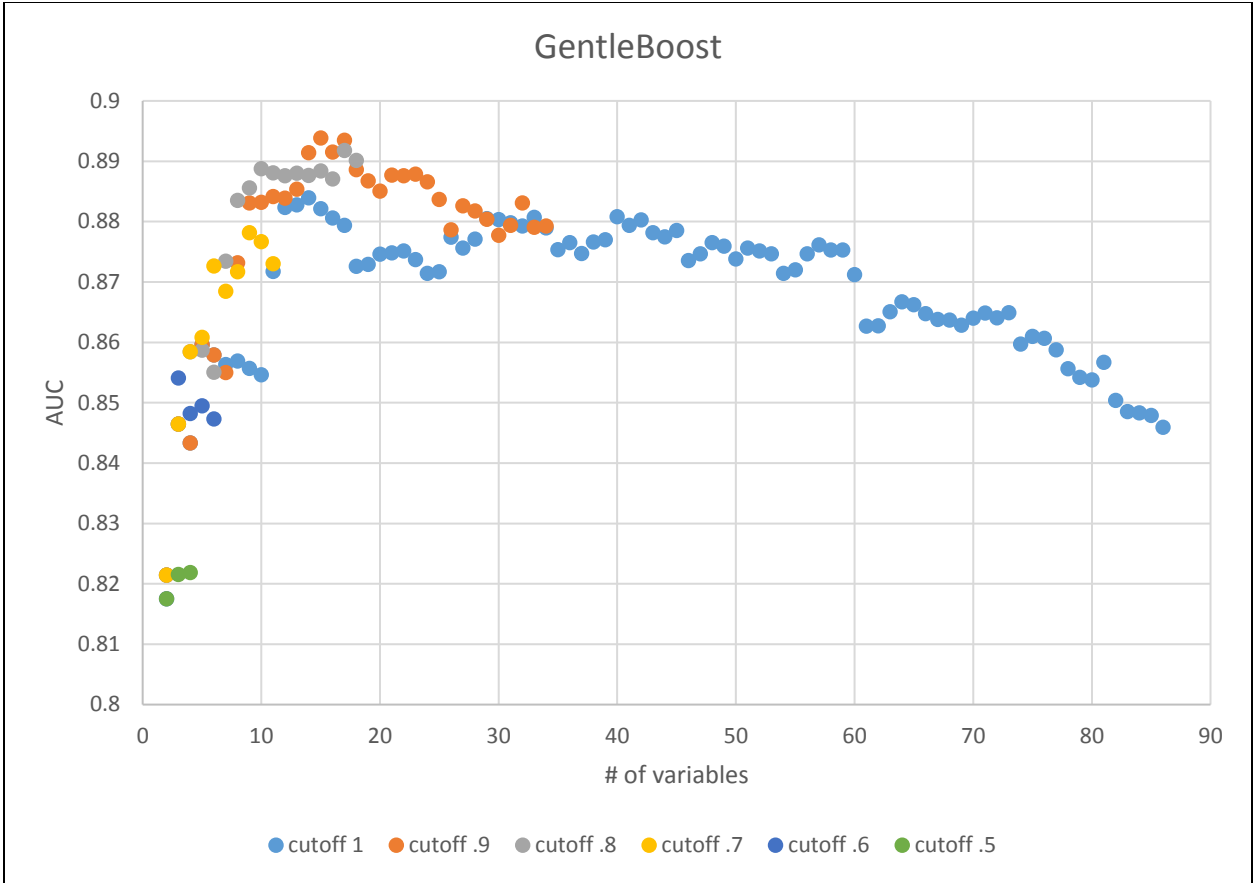


Figure 63: Serial Addition for AdaBoost, AUC vs # of variables included by correlation cutoff

A comparison of the maximum average AUC values across the four models and their standard deviations is shown in Table 10. From this data it can be deduced that, by serial addition, the best differentiation occurs, on average, by using the GentleBoost methodology:

Table 10: Comparison of Models from Serial Addition

Model	Max Average	Std
AdaBoost	0.890	0.0257
RUSBoost	0.866	0.0299
RobustBoost	0.791	0.0440
GentleBoost	0.894	0.0229

This model selected 15 features, as shown in Table 11.

Table 11: Feature Formula and Feature Name for AdaBoostM1 from Serial Selection

Feature Formula	Feature Name
$\max(\text{abs}(\text{diff}(\text{Radii}(\text{mid}-1:))))$	Shape: Max: Diff: Radius
$\max(\text{Radii})/r$	Shape: Max: Radius
$\text{sum}(\text{Radii})$	Shape: Sum: Radius
$\text{sum}(\text{abs}(\text{diff}(\text{Radii})))$	Shape: Sum: Diff: Radius
$\text{sum}(\text{abs}(\text{diff}(\text{difindist}))) / r$	Shape: Sum: Diff: Distance Between Slices
$\text{mean}((\text{node}(:, \text{SubBase})))$	Histogram Features: Mean: Mean: Base
$\text{min}((\text{node}(:, \text{SubBase})))$	Histogram Features: Min: Mean: Base
$\text{min}((\text{node}(:, \text{SubRing})))$	Histogram Features: Min: Mean: Ring
$\text{min}((\text{node}(:, \text{Base})))$	Histogram Features: Min: Mean: Base
$\max(\text{abs}(\text{diff}(\text{node}(:, \text{SubBase}))))$	Histogram Features: Max: Diff: Mean: Base
$\max(\text{abs}(\text{diff}(\text{node}(:, \text{SubRing}))))$	Histogram Features: Max: Diff: Mean: Ring
$\min(\text{abs}(\text{diff}(\text{node}(:, \text{Base}))))$	Histogram Features: Min: Diff: Mean: Base
$\max(\text{abs}(\text{diff}(\text{node}(:, \text{Ring}))))$	Histogram Features: Max: Diff: Mean: Ring
mean slice	Location
$\max(\text{abs}(\text{diff}(\text{node}(:, \text{SubBase}) .* \text{Radii})))$	Histogram Features: Max: Diff: Mean: Base
$\text{std}(\text{subbase-ring}) .* \text{Radii}$	Histogram Features: Std: Diff: Subbase-Ring

In forward selection, a comparison of all the models shows that AdaboostM1 has the second highest overall AUC average, but the lowest standard deviation, Table 12.

Table 12: Comparison of max average AUC and Standard deviation by model

Forward Selection		
Model	Max Average	Std
AdaBoost	0.89	0.031
GentleBoost	0.90	0.032
RUSBoost	0.88	0.031
RobustBoost	0.80	0.077

The AdaBoost model utilizes 17 features identified as best differentiating the normal tissues from pathologically enlarged lymph nodes, as shown in Table 13.

Table 13: Feature Formula and Feature Name for AdaBoostM1 from Forward Selection

Feature Formula	Feature Name
volume	Shape: Volume
max(abs(diff(radII(mid-1:)))	Shape: Max: Diff: Radius
sum(radII)	Shape: Sum: Radius
sum(abs(diff(radII)))	Shape: Sum: Diff: Radius
sum(abs(diff(difindist)))/r	Shape: Sum: Diff: Distance Between Slices
mean((node(:,SubBase).*radII))	Histogram Features: Mean: Mean: Base
mean((node(:,SubRing).*radII.^2))	Histogram Features: Mean: Mean: Ring
mean((node(:,Base).*radII.^2))	Histogram Features: Mean: Mean: Base
mean((node(:,Ring).*radII.^2))	Histogram Features: Mean: Mean: Ring
min((node(:,SubBase)))	Histogram Features: Min: Mean: Base
min(abs(diff(node(:,Base))))	Histogram Features: Min: Diff: Mean: Base
max(abs(diff(node(:,Ring))))	Histogram Features: Max: Diff: Mean: Ring
std(node(:,SubBase))	Histogram Features: Std: Base
mean slice	Location
max(abs(diff(node(:,SubRing).*radII)))	Histogram Features: Max: Diff: Mean: Ring
min(abs(diff(node(:,Ring).*radII)))	Histogram Features: Min: Diff: Mean: Ring
min(subbase-ring).*radII	Histogram Features: Min:Diff: Subbase-Ring

From the backward selection model, the results can be seen in Table 14.

Table 14: Comparison of max average AUC and std by model

Backward Selection		
Model	Max Average	Std
AdaBoost	0.90	0.033
GentleBoost	0.89	0.038
RUSBoost	0.87	0.034
RobustBoost	0.76	0.053

AdaBoost was selected here based on its highest max average AUC and low standard deviation.

The 12 features selected are shown in Table 15:

Table 15: Feature Formula and Feature Name for AdaBoostM1 from Backward Selection

Feature Formula	Feature Name
$\text{sum}(\text{abs}(\text{diff}(\text{radii})))$	Shape: Sum: Diff: Radius
mean slice	Location
$\text{min}(\text{node}(:, \text{subbase}))$	Histogram Features: Min: Mean: SubBase
$\text{sum}(\text{abs}(\text{diff}(\text{difindist}))) / \text{Axial Extent}$	Shape: Sum: Diff: Distance Between Slices
$\text{mean}(\text{node}(:, \text{subbase}) .* \text{radii})$	Histogram Features: Mean: Mean: SubBase
$\text{min}(\text{node}(:, \text{ring}) .* \text{radii})$	Histogram Features: Min: Mean: Ring
$\text{max}(\text{abs}(\text{diff}(\text{node}(:, \text{ring}))))$	Histogram Features: Max: Diff: Mean: Ring
$\text{min}(\text{abs}(\text{diff}(\text{node}(:, \text{ring}) .* \text{radii})))$	Histogram Features: Min: Diff: Mean: Ring
$\text{min}(\text{abs}(\text{diff}(\text{node}(:, \text{subring}) .* \text{radii})))$	Histogram Features: Min: Diff: Mean: SubRing
$\text{max}(\text{abs}(\text{diff}(\text{radii}(\text{mid}-1:))))$	Shape: Max: Diff: Radius
$\text{mean}(\text{subbase}-\text{ring}) .* \text{radii}$	Histogram Features: Mean: Diff: Subbase-Ring
$\text{mean}(\text{node}(:, \text{ring}) .* \text{radii} .^2)$	Histogram Features: Mean: Mean: Ring

For the mixed Forward/Backward feature selection method, the results can be seen in Table 16.

Table 16: Comparison of max average AUC and std by model

Forward and Back		
Model	Max Average	Std
AdaBoost	0.89	0.031
GentleBoost	0.89	0.033
RUSBoost	0.88	0.032
RobustBoost	0.80	0.075

AdaBoost was selected based on its lowest standard deviation value and selected 12 features, shown in Table 17

Table 17: Feature Formula and Feature Name for AdaBoostM1 from Forward/Backward Selection

Feature Formula	Feature Name
$\max(\text{abs}(\text{diff}(\text{Radii}(\text{mid}-1:))))$	Shape: Max: Diff: Radius
$\text{sum}(\text{Radii})$	Shape: Sum: Radius
$\text{sum}(\text{abs}(\text{diff}(\text{Radii})))$	Shape: Sum: Diff: Radius
$\text{sum}(\text{abs}(\text{diff}(\text{difindist}))/r)$	Shape: Sum: Diff: Distance Between Slices
$\text{mean}((\text{node}(:,\text{Ring}).*\text{Radii}.^2))$	Histogram Features: Mean: Mean: Ring
$\text{min}((\text{node}(:,\text{SubBase})))$	Histogram Features: Min: Mean: Base
$\text{min}(\text{abs}(\text{diff}(\text{node}(:,\text{SubBase}))))$	Histogram Features: Min: Diff: Mean: Base
$\text{max}(\text{abs}(\text{diff}(\text{node}(:,\text{SubBase}))))$	Histogram Features: Max: Diff: Mean: Ring
$\text{max}(\text{abs}(\text{diff}(\text{node}(:,\text{Ring}))))$	Histogram Features: Max: Diff: Mean: Ring
mean slice	Location
$\text{min}(\text{abs}(\text{diff}(\text{node}(:,\text{SubBase}).*\text{Radii})))$	Histogram Features: Min: Diff: Mean: Ring
$\text{std}(\text{subbase-ring})$	Histogram Features: Std: Diff: Subbase-Ring

A comparison of the best AUC and standard deviation from each method, Serial, Forward, Backward, and Forward/Backward, was created using leave-one-out cross validation. These are shown in Figure 64, Figure 65, Figure 66, and Figure 67, respectively.

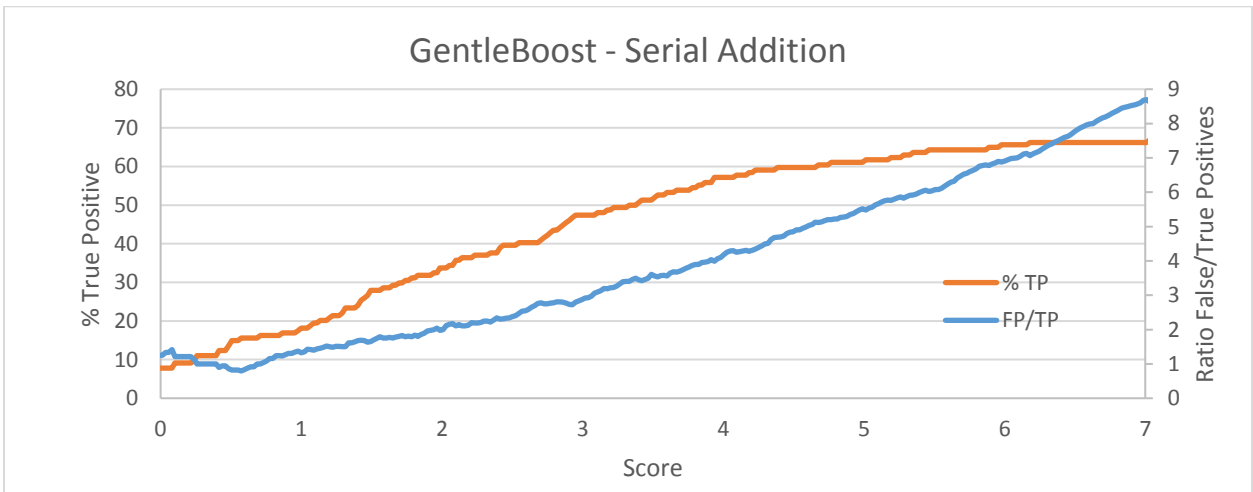


Figure 64: % TP and Ratio False/True positives vs score for GentleBoost on Serial Addition

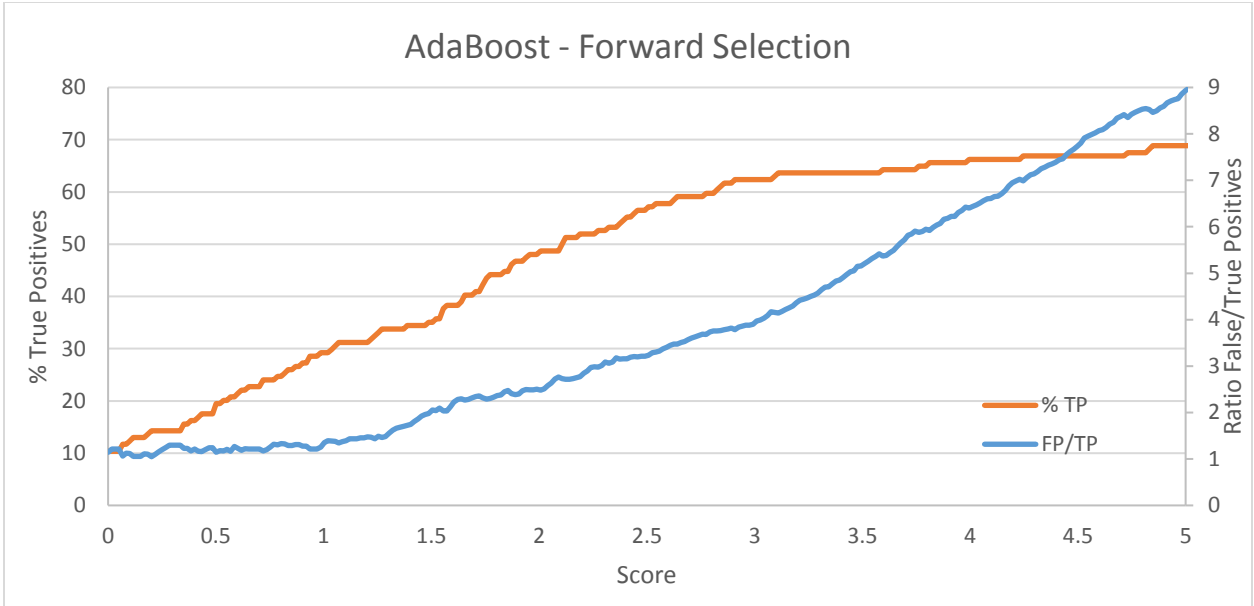


Figure 65: %TP and Ratio False/True positives vs score for AdaBoost for Forward Selection

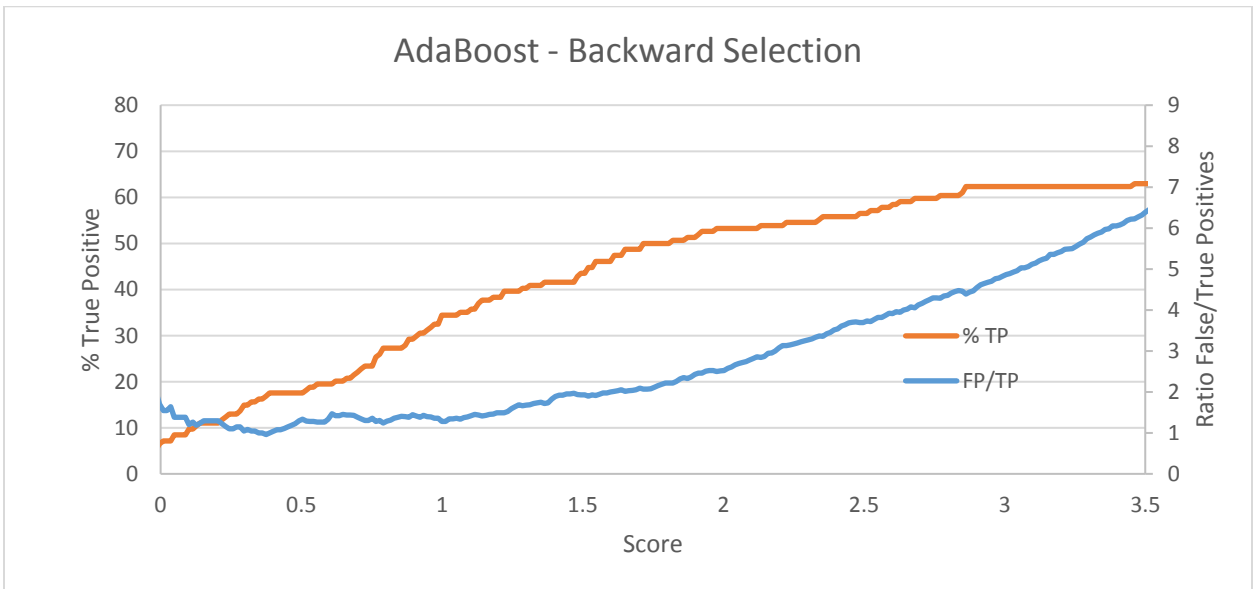


Figure 66: %TP and Ratio False/True positives vs score for AdaBoost for Backward Selection

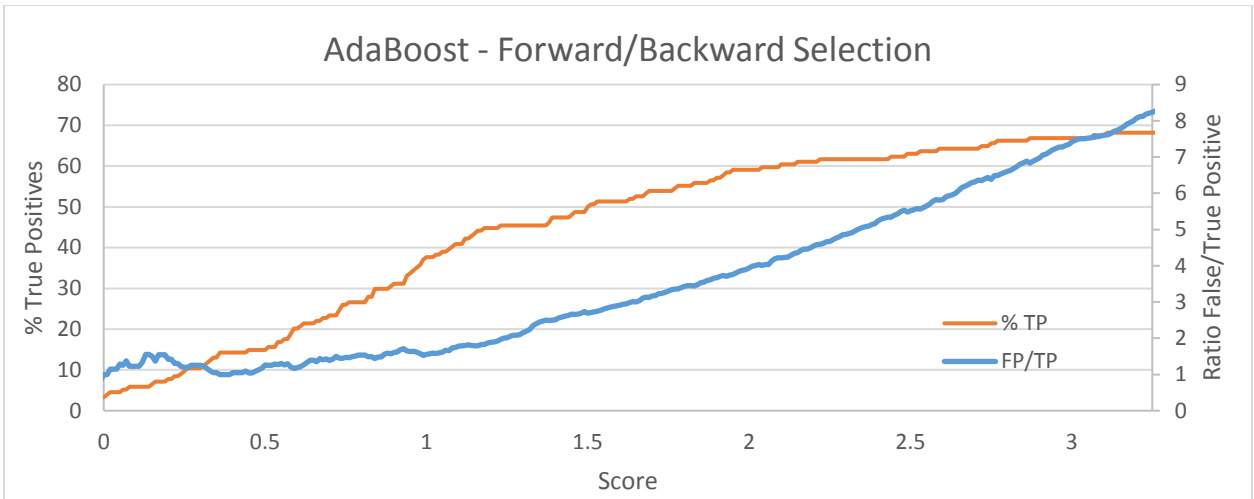


Figure 67: %TP and Ratio False/True positives vs score for AdaBoost for Forward/Backward Selection

A comparison of all three can be better visualized as the ratio of false/true positives vs the % true positives identified, seen in Figure 68.

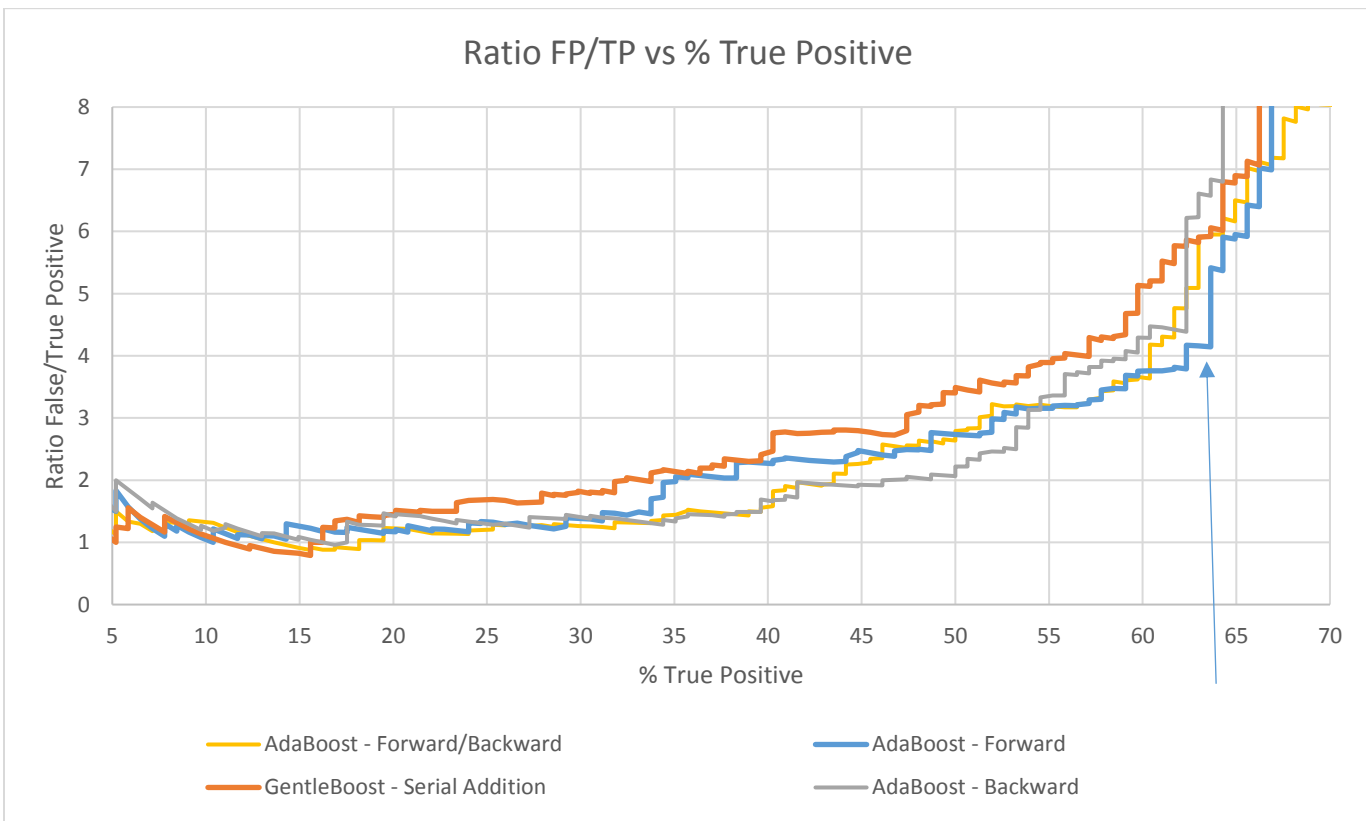


Figure 68: Ratio of False/True Positives vs % True Positives for the top models of each technique

From these, the AdaBoostM1 model and Forward-Selection feature technique were ultimately selected, because of their ability to identify approximately 64% of the true positives with a false/true

positive ratio of 4:1. The final features, consisting of being 5 shape features, 1 location feature, and 11 histogram features can be seen in Table 13.

3.6. Pinnacle Contour Creation

A score for each node candidate would be useless unless it is normalized or grouped as to the likelihood that it is truly pathological. For contour naming purposes, the scores were grouped into 3 potential categories: ‘Highly-Likely’, ‘Likely’, and ‘Somewhat-Likely’ with regards to how likely the score was associated with being a true-positive pathologic node.

The score cutoffs for each group are represented in Figure 69, where blue is representative of the ‘Highly-Likely’ group, and therefore has the lowest score range, green is for the ‘Likely’ group, and yellow for the ‘Somewhat-Likely’.

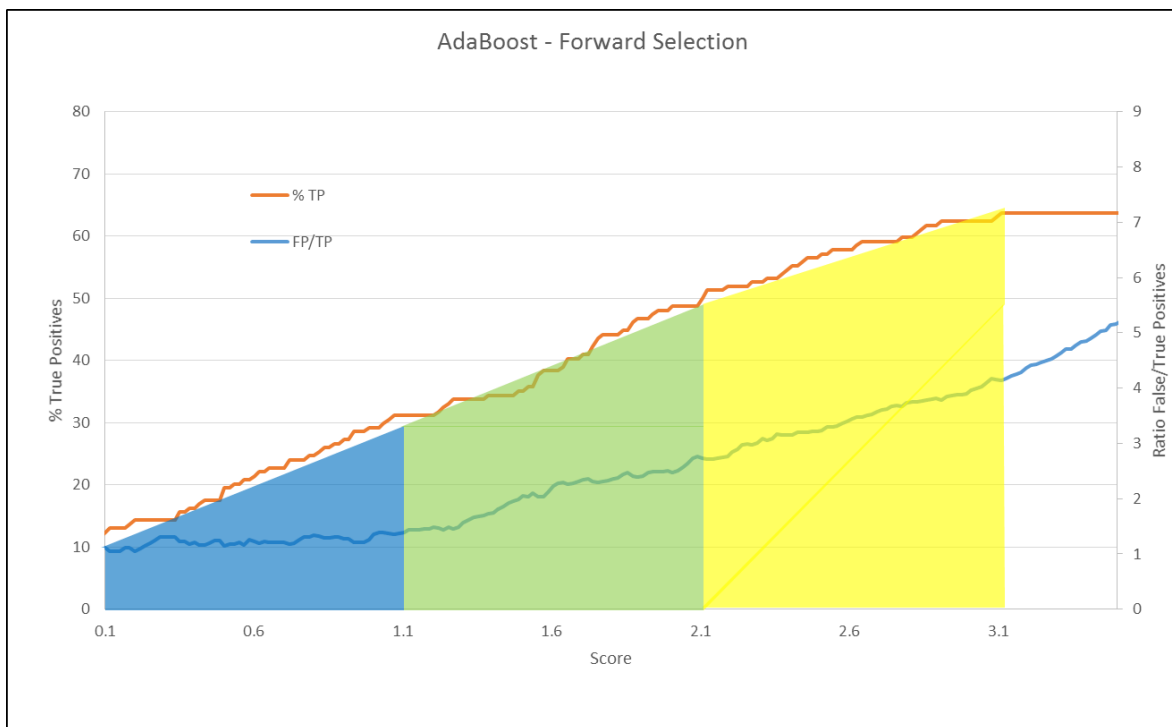


Figure 69: Breakdown among groups by score: Blue 'Highly-Likely', green 'Likely', and yellow 'Somewhat-Likely'

Structures with a score less than 1.1 will be grouped into the ‘Highly-Likely’ group, and the contour generated in Pinnacle will be blue. Similarly, structures with a score between 1.1 and 2.1 are categorized as ‘Likely’, structures scoring above 2 are categorized into ‘Somewhat-Likely’, and anything above 3.1 will be removed.

3.7. Validation Set

In order to validate these results, twenty new patients from MD Anderson with pretreatment PET/CT were entered into the program, these not being part of the initial training or test set as outlined in the previous section. These patients had 35 total pathologic nodes, with a distribution as shown in Figure 70.

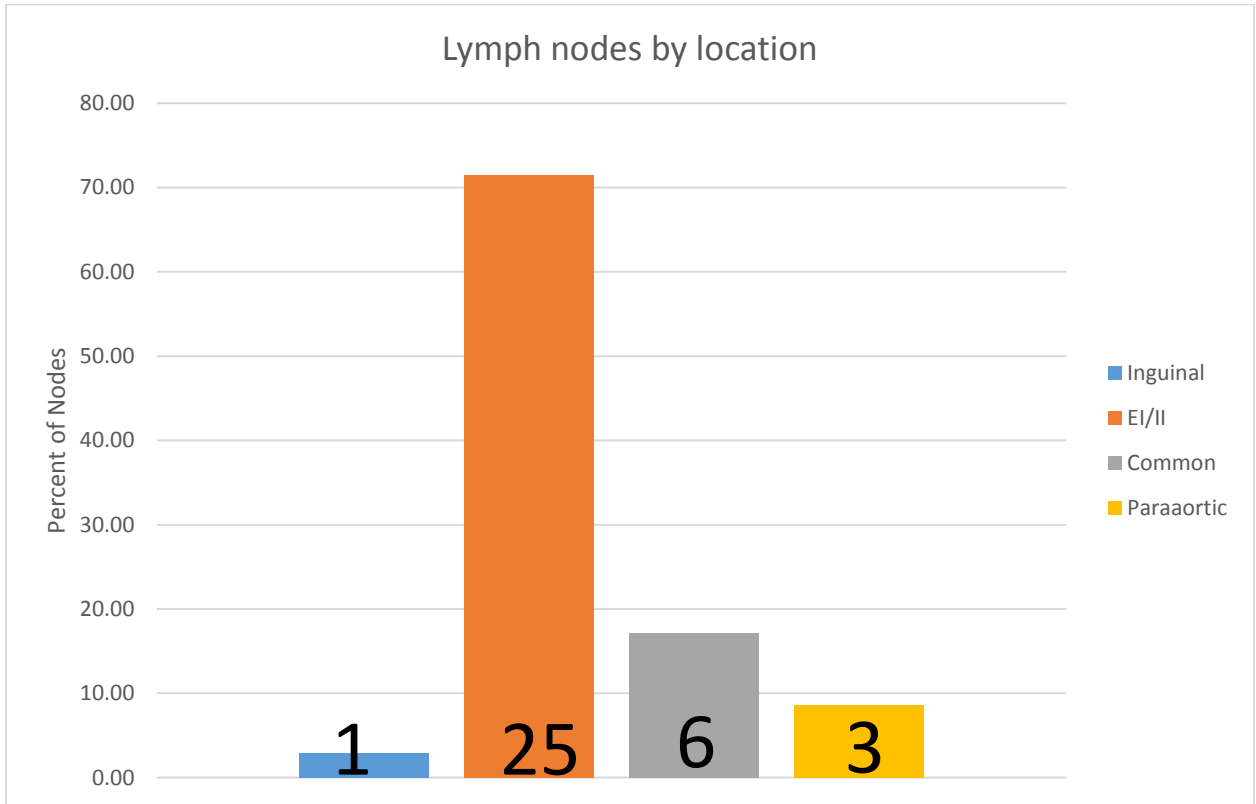


Figure 70: Distribution of Nodes in Validation Set

The optimized model, generated from the fifty-eight initial patients, was then used on this new validation patient set, generating the curve shown in Figure 71.

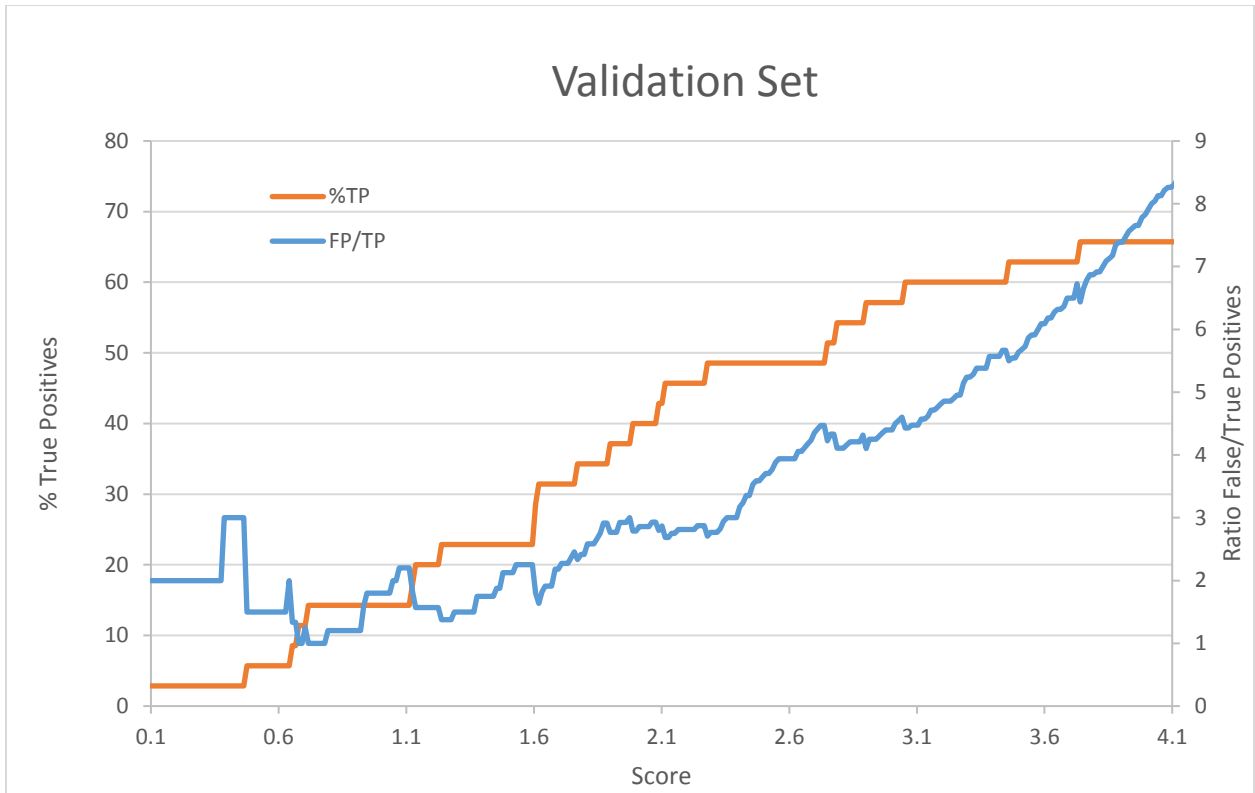


Figure 71: % True Positives and Ratio False/True Positives vs Score for Validation Set. TP means True Positive and FP means False Positive. A score cutoff of 3.1 has been previously determined based on the fifty-eight patient dataset. All scores are included for illustration purposes only. Axis have been changed to start at 0.1 for visualization purposes

The results from leave-one-out cross validation of the initial fifty-eight identified ~63% of the pathologically enlarged lymph nodes, along with a false to true positive ratio of ~4 to 1. These findings were further investigated with a validation set of twenty patients, with ~60% of the pathologically enlarged lymph nodes identified and a false to true positive ratio of ~4 to 1 was determined.

3.8. Discussion

It is possible to differentiate pathologically enlarged lymph nodes from normal tissue using machine learning and a set of variable features. While the 86 features created here to differentiate normal tissues from the pathologically enlarged lymph nodes, it is entirely possible that there exist better features not yet imagined. Such feature improvement may further enhance results with this model in the future.

The scoring cutoffs for the groups ‘Highly Likely’, ‘Likely’, and ‘Somewhat Likely’ are relatively arbitrary, and might also be improved upon. It was considered reasonable to select the scores which had false/true positive ratio around 1, 3, and 4 to designate each group, and the final ‘cutoff’ was selected due

to the general plateau seen in Figure 69, in the percent of true positives found. Further work in this area may also lead to a more robust methodology in future iterations of this program. However, it is hoped that the current model will improve patient care in those locations where imaging modalities and physician expertise is limited.

4. Chapter 4: Discussion

4.1. General Review

It was hypothesized that a program could be developed that would be capable of identifying 75% of the pathologically enlarged lymph nodes with a false to true positive ratio less than 5:1. The program's sensitivity for the original fifty-eight patients was ~63% and for the twenty patient validation set was ~60%. Although this is lower than what would be expected in a CAD system for lung nodules, the false positive ratio is relatively similar (~4:1 false/true positive). Also, the abdomen and pelvis are a much more difficult area to separate pathologic structures from normal tissue, when compared to chest CAD systems. Ultimately the goal of being identifying 75% of the pathologically enlarged lymph nodes was not met. However, an ability to maintain a ratio of false positives to true positives of 5:1 was approximately achieved.

4.2. Strengths and Weaknesses by Location

The ability of the program to identify nodes based on anatomical location using leave-one-out model building of the original fifty-eight patients is shown in Figure 72. The original fifty-eight patients were used since these patients had a more even distribution of nodes across the anatomical regions than the validation set.

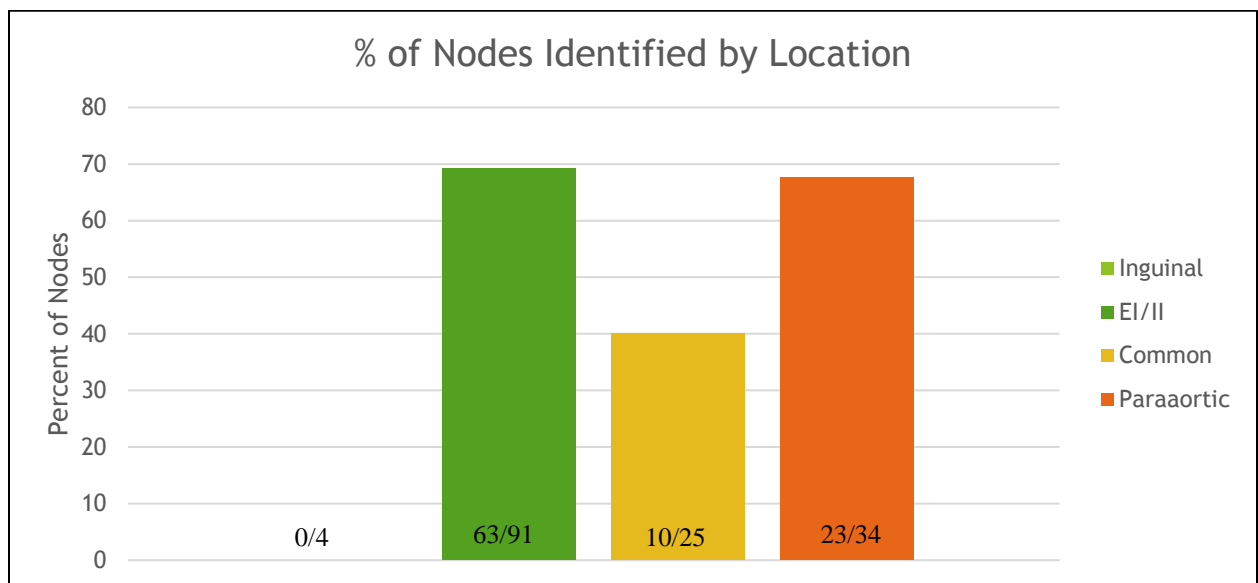


Figure 72: % of Nodes identified by anatomical location of the original fifty-eight patients

The program appeared best able to identify external/internal iliac nodes and paraaortic nodes, identifying 69% (63/91) and 67% (23/34) nodes, respectively. The program did not identify the inguinal nodes in the original fifty-eight patients. However the small dataset (4 inguinal nodes) makes it difficult to draw conclusions about its ability in this region. It appears that the program had the largest difficulty with identifying nodes in the common iliac region, identifying 40% (10/25) of the pathologically enlarged nodes present.

The nodes identified within the paraaortic region are arguably the most important, as any positive lymph nodes identified within this region will result in raising the superior aspect of the four-field box to include this likely diseased nodal field.

One of the largest challenges in detecting pathologically enlarged lymph nodes is that their HUs are very similar to normal tissue which surrounds them. Also, the way in which the nodes often press or collapse against normal structures can make them difficult to separate out as independent surfaces and structures. Evaluation of the program's failure to identify nodes show that most of the failures are nodes pressed tightly into the normal tissue structures, as seen in Figure 73, and the program cannot separate them.



Figure 73: Example of a node that the program could not find, contoured in red/green by physician

The program appears to be able to best identify nodes when they are separable from normal tissues, allocating them the lowest score, Figure 74. This appears to occur most frequently in the external/internal iliac region and the paraaortic region, which could explain those anatomical regions having the highest rate of identification.

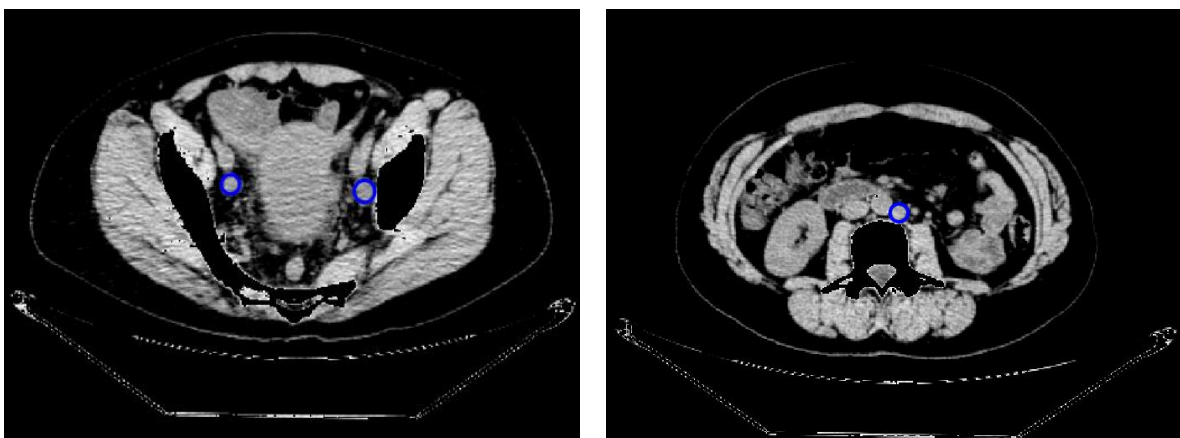


Figure 74: Examples of identification of two external iliac nodes and paraaortic node (blue) that the program correctly identified

A comparison of the ratio of false positives to true positives identified by anatomical location is shown in Figure 75. This demonstrates that the failures of the program to identify common iliac nodes

greatly increases the ratio of false to true positives. The program appears to perform best in the internal/external iliac region. This is likely because, with the mask, there are not a large number of relatively circular objects on an axial slice which could be misidentified as lymph node.

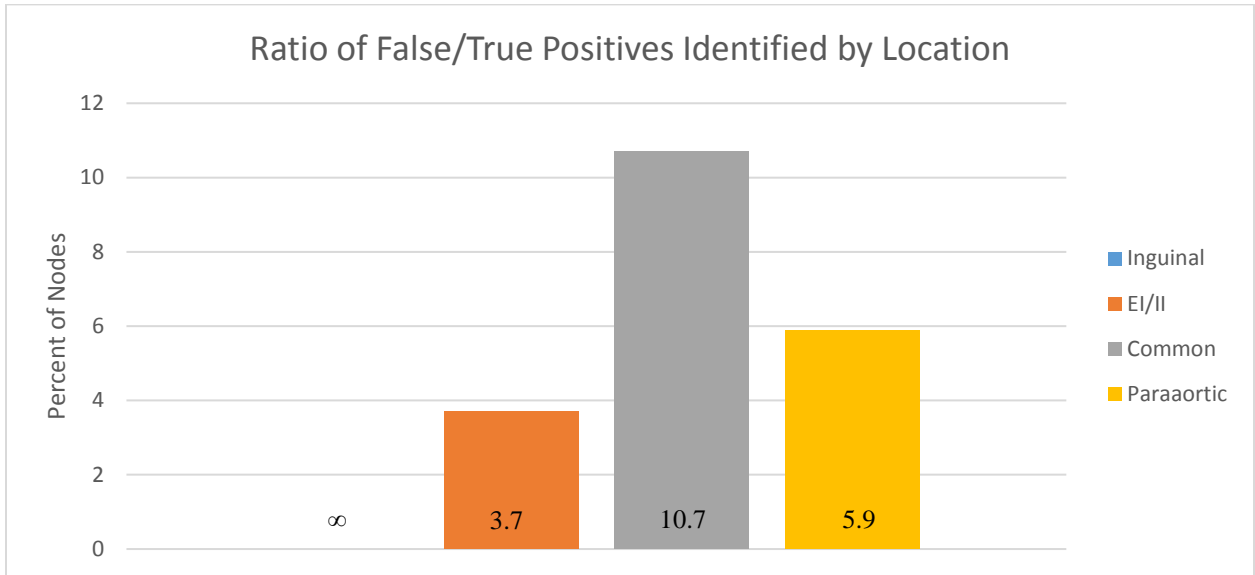


Figure 75: Ratio of false positives to true positives identified by anatomical location of the original fifty-eight patient cohort

I believe that the reason for the validation set achieving a better ratio of false/true positives is based on these patients having a slice thickness of around 2 to 2.5 mm, while the initial fifty-eight primarily had slice thicknesses around 3.27mm. While the program has been written to take slice thickness into account, better image quality and thinner slices are likely to improve its ability to differentiate between normal tissues and potential disease pathology.

4.2.1. Limitations

This work has several limitations. All patients were acquired from a single institution, MD Anderson Cancer Center, in the United States. It is possible that these patients are not comparable between the United States, given their residence in a very high HDI country, and a LMIC. The validation set only contains twenty patients, within which only 3 paraaortic nodes were present. It would be useful to include more patients for confirmation, particularly those with paraaortic involvement. While this work has not been validated with other patient groups outside the US, work is currently being done with a clinic in Botswana utilizing this program.

The program has been written such that the slice thickness of the CT scanner is accounted for, however, pathologically enlarged nodes on thicker slices will likely be more difficult to identify than on thinner slices. The sensitivity of the program in regards to this has not been investigated. While pixel size varied among the patients due to the changes in FOV, the sensitivity of the program with respect to varying pixel size was not characterized. Image quality could affect the capability of the program's ability to identify pathologically enlarged lymph nodes. Factors leading to changes in the measured HUs, such as metal or body habitus that is larger than the field-of-view, would affect the program, as surface separation criteria are based on HUs.

The deformation of the initial CTV is a manual process. While work is currently being done to automate this, it is a major limitation in the feasibility of this program becoming a truly fully automated system.

All of the CTs scans on the patients used for this program were with 0 degrees of angle. Large scan angles could, hypothetically, cause issues in the program's ability to identify 'starting points' in the 3D identification of pathologic nodes, as described in section 2.7- Identification of start points. The effect of different scan angles on the accuracy of the program has not been investigated.

The program's accuracy based on stage of patient disease (IIA, III, etc.) has not been investigated. The fifty-eight original patients were selected based on the presence of significant lymphatic disease, often with a large amount of paraaortic involvement. The paraaortic proportion of disease in the validation set was much less than that of the training set, so sensitivity by anatomical location was used in the original fifty-eight with leave-one-out cross validation. This might not be an accurate representation of the population, and more patients with disease in locations other than the EI/II would be beneficial.

4.2.2. Future Implementation

This program was created as a tool to improve cervical cancer treatment by identifying disease which might otherwise go untreated. In particular, it is suggested that this would assist in the identification of disease that might require raising the superior block of the four-field box. As is, this

program does not have a high enough sensitivity and specificity to run without supervision. It has been created as a tool to assist in the identification of disease. However, each contour created should be evaluated critically, and the lack of a contour on an object is not justification for considering it to be non-nodal.

The entire program is ~50 Megabytes in size and takes approximately (10/number of cores minutes) to run on an individual patient. As most computers have 2-4 cores, each patient takes approximately 2.5 minutes to run on a 4 core machine, or up to 5 minutes on a 2 core machine. It runs as a standalone .exe, with the user input required to select the desired image files after image deformation and output folder, Figure 76.

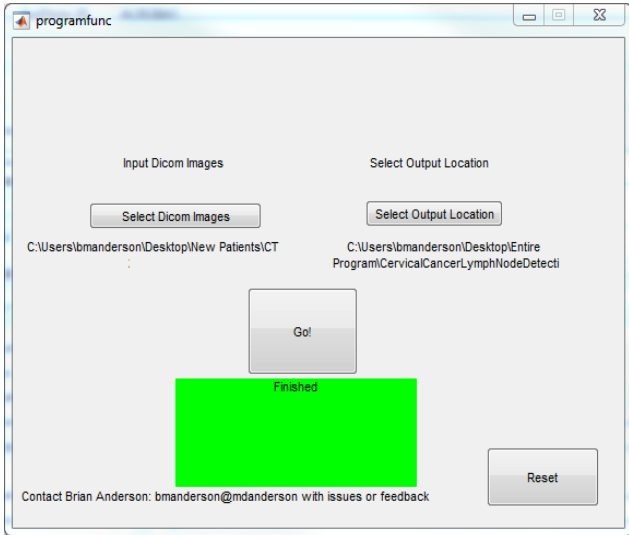
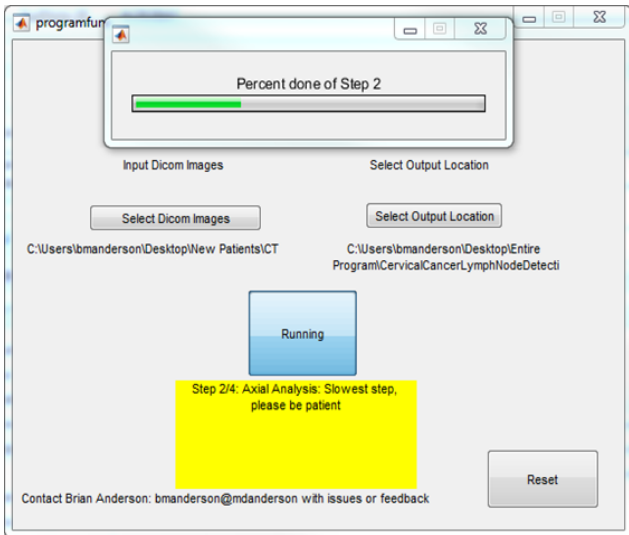
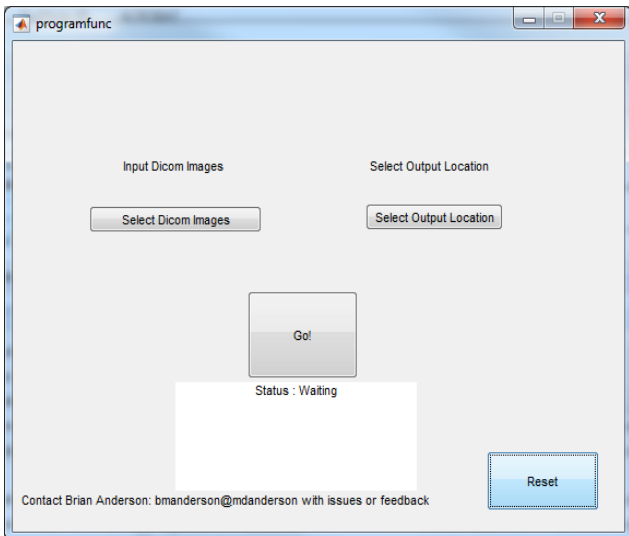


Figure 76: Example of program operation

The deformable registration is currently being automated, although for this work it required manual user interface. The DICOM structure file, created in the designated output location, can then be imported into a treatment planning system for evaluation of generated contours

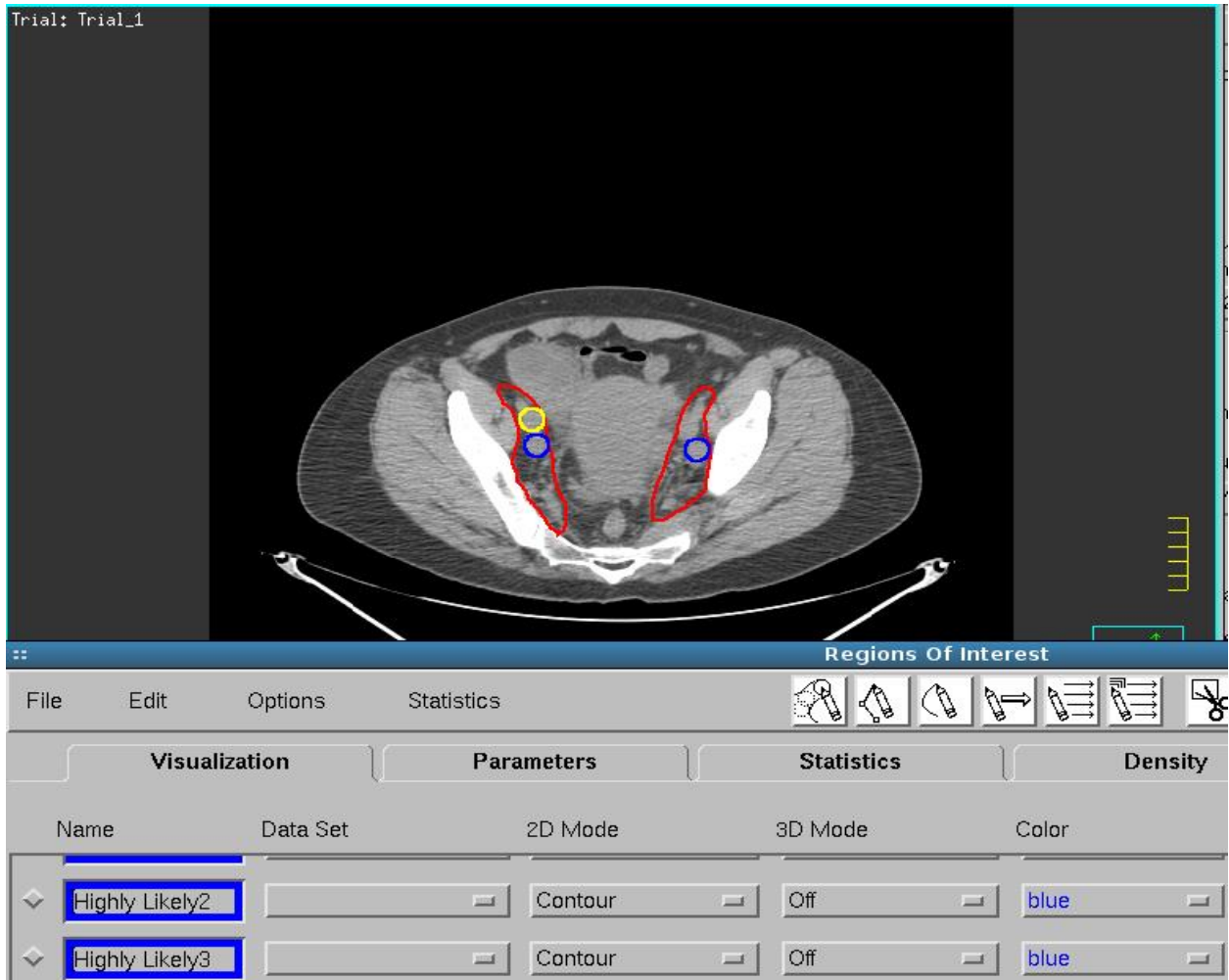


Figure 77: Example of structure imported into treatment planning system. Two EI/II nodes properly identified in the 'Highly Likely' group (blue), and artery falsely identified in the 'Somewhat Likely' group (yellow)

4.3. Conclusion

This program provides an inexpensive, simple, and rapid way to improve cervical cancer treatment planning in resource limited settings with little impact on clinical workflow. The ability to identify pathologically enlarged nodes from non-contrast CT images which are already acquired can vastly improve treatment. These improvements include: providing boost treatment for any pathologic nodes and, in the case of paraaortic metastasis, raising the superior aspect of the four-field box to include otherwise

untreated disease. Positive node identification is essential, and can lead to optimal field of treatment or boost (20). This is especially important in locations lacking PET imaging, and those with limited resources.

References

1. 2014. Baseline country survey on medical devices. *World Heal. Organ.* .
2. Takiar, V., H. P. Fontanilla, P. J. Eifel, A. Jhingran, P. Kelly, R. B. Iyer, C. F. Levenback, Y. Zhang, L. Dong, and A. Klopp. 2013. Anatomic distribution of fluorodeoxyglucose-avid para-aortic lymph nodes in patients with cervical cancer. *Int. J. Radiat. Oncol. Biol. Phys.* 85: 1045–50.
3. Stewart, B. W., and C. P. Wild. 2014. World cancer report 2014. *World Heal. Organ.* 1–2.
4. Ferlay, J., H.-R. Shin, F. Bray, D. Forman, C. Mathers, and D. M. Parkin. 2010. Estimates of worldwide burden of cancer in 2008: GLOBOCAN 2008. *Int. J. Cancer* 127: 2893–2917.
5. IARC Monographs on the Evaluation of Carcinogenic Risks to Humans Human Papillomaviruses
IARC MONOGRAPHS. .
6. Chuang, L. T., S. Temin, R. Camacho, A. Dueñas-Gonzalez, S. Feldman, M. Gultekin, V. Gupta, S. Horton, G. Jacob, E. A. Kidd, K. Lishimpi, C. Nakisige, J.-H. Nam, H. Y. S. Ngan, W. Small, G. Thomas, and J. S. Berek. 2016. Management and Care of Women With Invasive Cervical Cancer: American Society of Clinical Oncology Resource-Stratified Clinical Practice Guideline. *J. Glob. Oncol.* 2: 311–340.
7. Krahl, V. E. 1960. Anatomy of the human body (Gray’s Anatomy). By Henry Gray. Twenty-seventh edition (American Centennial Edition). Edited by Charles Mayo Goss. 1458 pages with 1174 illustrations, mostly in color. \$17.50. Lea & Febiger, 600 Washington Square, Philadelphia, Pa., 1959. *Anat. Rec.* 136: 505–505.
8. SEER. 2013. *Cancer of the Cervix Uteri (Invasive)*,.
9. Tinga, D. J., P. R. Timmer, J. Bouma, and J. G. Aalders. 1990. Prognostic significance of single versus multiple lymph node metastases in cervical carcinoma stage IB. *Gynecol. Oncol.* 39: 175–180.
10. Wong, T., E. L. Jones, and R. E. Coleman. 2004. Positron emission tomography with 2-deoxy-2-[18F]fluoro-D-glucose for evaluating local and distant disease in patients with cervical cancer. *Mol. Imaging Biol.* 6: 55–62.
11. PDQ Adult Treatment Editorial Board. 2002. *Cervical Cancer Treatment (PDQ®): Patient Version*,.

12. International Atomic Energy Agency. 2013. IAEA HUMAN HEALTH REPORTS No.6 Management of Cervical Cancer: Strategies for Limited-resource Centres — A Guide for Radiation Oncologists. 20.
13. Gulia, A., F. Patel, B. Rai, A. Bansal, and S. C. Sharma. 2013. Conventional four field radiotherapy versus computed tomography-based treatment planning in cancer cervix: A dosimetric study. *South Asian J. cancer* 2: 132–5.
14. Zunino, S., O. Rosato, S. Lucino, E. Jauregui, L. Rossi, and D. Venencia. 1999. Anatomic study of the pelvis in carcinoma of the uterine cervix as related to the box technique. *Int. J. Radiat. Oncol.* 44: 53–59.
15. Nagar, Y. S., S. Singh, S. Kumar, and P. Lal. 2004. Conventional 4-field box radiotherapy technique for cancer cervix: potential for geographic miss without CECT scan-based planning. *Int. J. Gynecol. Cancer* 14: 865–870.
16. Singh, D., H. Latha, A. Kapoor, A. Mayilvaganan, S. L. Jakhar, and H. S. Kumar. 2015. Necessity of CT-MRI based treatment planning for cervical tumors with retroverted uterus: A case report with review of literature. *J. Cancer Res. Ther.* 11: 662.
17. Avinash, H. U., T. R. Arul Ponni, M. G. Janaki, A. S. Kirthi Koushik, and S. M. Kumar. 2015. A prospective dosimetric and clinical comparison of acute hematological toxicities in three-dimensional conformal radiation therapy and intensity modulated radiation therapy with concurrent chemotherapy in carcinoma cervix. *J. Cancer Res. Ther.* 11: 83–7.
18. Fontanilla, H. P., A. H. Klopp, M. E. Lindberg, A. Jhingran, P. Kelly, V. Takiar, R. B. Iyer, C. F. Levenback, Y. Zhang, L. Dong, and P. J. Eifel. 2013. Anatomic distribution of [18F] fluorodeoxyglucose-avid lymph nodes in patients with cervical cancer. *Pract. Radiat. Oncol.* 3: 45–53.
19. Cox, J. D., K. K. Ang, and P. J. Eifel. 2010. Chapter 29 – The Uterine Cervix. In *Radiation Oncology* 733–773.
20. Ariga, T., T. Toita, G. Kasuya, Y. Nagai, M. Inamine, W. Kudaka, Y. Kakinohana, Y. Aoki, and S. Murayama. 2013. External beam boost irradiation for clinically positive pelvic nodes in patients with uterine cervical cancer. *J. Radiat. Res.* 54: 690–6.
21. Marnitz, S., C. Köhler, S. Bongardt, U. Braig, H. Hertel, and A. Schneider. 2006. Topographic

- distribution of sentinel lymph nodes in patients with cervical cancer. *Gynecol. Oncol.* 103: 35–44.
22. El-Baz, A., G. M. Beache, G. Gimel'farb, K. Suzuki, K. Okada, A. Elnakib, A. Soliman, and B. Abdollahi. 2013. Computer-aided diagnosis systems for lung cancer: challenges and methodologies. *Int. J. Biomed. Imaging* 2013: 942353.
23. Gurcan, M. N., B. Sahiner, N. Petrick, H.-P. Chan, E. A. Kazerooni, P. N. Cascade, L. Hadjiiski, P. Prettenhofer, R. Weiss, V. Dubourg, J. Vanderplas, A. Passos, D. Cournapeau, M. Brucher, M. Perrot, and E. Duchesnay. 2002. Lung nodule detection on thoracic computed tomography images: Preliminary evaluation of a computer-aided diagnosis system. *Med. Phys.* 29: 2552–2558.
24. Balagurunathan, Y., V. Kumar, Y. Gu, J. Kim, H. Wang, Y. Liu, D. B. Goldgof, L. O. Hall, R. Korn, B. Zhao, L. H. Schwartz, S. Basu, S. Eschrich, R. A. Gatenby, and R. J. Gillies. 2014. Test–Retest Reproducibility Analysis of Lung CT Image Features. *J. Digit. Imaging* 27: 805–823.
25. Tan, M., R. Deklerck, B. Jansen, M. Bister, and J. Cornelis. 2011. A novel computer-aided lung nodule detection system for CT images. *Med. Phys.* 38: 5630–5645.
26. Teramoto, A., and H. Fujita. 2013. Fast lung nodule detection in chest CT images using cylindrical nodule-enhancement filter. *Int. J. Comput. Assist. Radiol. Surg.* 8: 193–205.
27. Cascio, D., R. Magro, F. Fauci, M. Iacomi, and G. Raso. 2012. Automatic detection of lung nodules in CT datasets based on stable 3D mass–spring models. *Comput. Biol. Med.* 42: 1098–1109.
28. Riccardi, A., T. S. Petkov, G. Ferri, M. Masotti, and R. Campanini. 2011. Computer-aided detection of lung nodules via 3D fast radial transform, scale space representation, and Zernike MIP classification. *Med. Phys.* 38: 1962–1971.
29. Messay, T., R. C. Hardie, and S. K. Rogers. 2010. A new computationally efficient CAD system for pulmonary nodule detection in CT imagery. *Med. Image Anal.* 14: 390–406.
30. Cupples, T. E., J. E. Cunningham, and J. C. Reynolds. 2005. Impact of Computer-Aided Detection in a Regional Screening Mammography Program. *Am. J. Roentgenol.* 185: 944–950.
31. Freer, T. W., and M. J. Ullissey. 2001. Screening Mammography with Computer-aided Detection: Prospective Study of 12,860 Patients in a Community Breast Center. *Radiology* 220: 781–786.

32. McMahon, C. J., N. M. Rofsky, and I. Pedrosa. 2010. Lymphatic Metastases from Pelvic Tumors: Anatomic Classification, Characterization, and Staging. *Radiology* 254: 31–46.
33. Zhang, L., L. Dong, L. Court, H. Wang, M. Gillin, and R. Mohan. 2005. TU-EE-A4-05: Validation of CT-Assisted Targeting (CAT) Software for Soft Tissue and Bony Target Localization. *Med. Phys.* 32: 2106–2106.
34. Wang, H., L. Dong, J. O’Daniel, R. Mohan, A. S. Garden, K. K. Ang, D. A. Kuban, M. Bonnen, J. Y. Chang, and R. Cheung. 2005. Validation of an accelerated “demons” algorithm for deformable image registration in radiation therapy. *Phys. Med. Biol.* 50: 2887–2905.
35. Hastie, T., R. Tibshirani, and J. Friedman. 2009. The Elements of Statistical Learning. *Elements* 1: 337–387.
36. Rokach, L. 2010. Ensemble-based classifiers. *Artif Intell Rev* 33: 1–39.
37. Friedman, J., T. Hastie, R. Tibshirani, and Y. Stanford. 1998. Additive Logistic Regression: a Statistical View of Boosting. .
38. Seiffert, C., T. Khoshgoftaar, and J. Hulse. 2009. RUSBoost: A Hybrid Approach to Alleviating Class Imbalance. *IEEE* 185–197.
39. Freund, Y. A more robust boosting algorithm. .

Vita

Brian Mark Anderson was born in Houston, Texas on January 28, 1992, the son of Mark and Sally Anderson. The family moved to Hickory, North Carolina shortly thereafter. After completing high school at Hickory High School in 2010, he entered The Georgia Institute of Technology in Atlanta, Georgia. In May 2015, he received the degree of Bachelor of Science with highest honors, with a major in Nuclear and Radiological Engineering. In August 2015 he entered The University of Texas MD Anderson Cancer Center, UTHealth Graduate School of Biomedical Sciences. He will re-enter this program in August 2017 in pursuit of a Ph.D. in the field of Medical Physics. Brian enjoys his time biking, rock climbing, and reading.

Permanent address:

Brian Mark Anderson

7010 Stafford Shire St NW

Apt 445

Houston, TX 77030